National Laser Users' Facility and External Users' Programs

Under the facility governance plan implemented in FY08 to formalize the scheduling of the Omega Laser Facility as a National Nuclear Security Administration (NNSA) User Facility, Omega Facility shots are allocated by campaign. The majority (68.1%) of the FY17 target shots were allocated to the Inertial Confinement Fusion (ICF) Campaign conducted by integrated teams from Lawrence Livermore National Laboratory (LLNL), Los Alamos National Laboratory (LANL), Naval Research Laboratory (NRL), Sandia National Laboratories (SNL), and LLE; and to the High-Energy-Density (HED) Campaigns conducted by teams led by scientists from the national laboratories, some with support from LLE.

The Fundamental Science Campaigns accounted for 24.2% of the Omega Laser Facility target shots taken in FY17. Nearly 62% of these shots were dedicated experiments under the National Laser Users' Facility (NLUF) Program, and the remaining shots were allotted to the Laboratory Basic Science (LBS) Program, comprising peer-reviewed fundamental science experiments conducted by the national laboratories and by LLE.

The Omega Laser Facility was also used for several campaigns by teams from the Commissariat à l'énergie atomique et aux énergies (CEA) of France. These programs are conducted at the facility on the basis of special agreements put in place by Department of Energy (DOE)/NNSA and participating institutions.

In this section, we briefly review all the external user activity at the Omega Laser Facility during FY17.

FY17 NLUF Program

During the first quarter of fiscal year 2017 (FY17), the Inertial Fusion Office of DOE/NNSA completed a solicitation, review, and selection process for NLUF experiments to be conducted at the Omega Laser Facility during calendar years (CY's) 2017 and 2018. Twenty-eight proposals were submitted in response to the call for proposals, and the shot requests totaled 60.5 shot days at the Omega Laser Facility. The proposals were peer reviewed by an independent review committee, and ICF/NNSA selected 13 proposals for funding and shot allocation for CY17–CY18.

CY17 was the first of a two-year period of performance for these 13 NLUF projects (Table 152.VI). In addition, several NLUF campaigns completed experiments during FY17 that had been approved during the FY15–FY16 NLUF cycle. In total, 319 target shots were taken for NLUF projects during FY17. The NLUF experiments conducted at the facility during FY17 are summarized in this section.

A critical part of the NLUF program is the education and training of graduate students in high-energy-density physics. During the year, 33 graduate students from nine universities participated in experiments conducted under the NLUF program at the Omega Laser Facility (Table 152.VII).

Transport of Relativistic Electrons in Cylindrically Imploded Magnetized Plasmas

Principal Investigator: F. N. Beg [University of California, San Diego (UCSD)]
Co-investigators: P. Forestier-Colleoni, M. Dozières, and C. McGuffey (UCSD); M. S. Wei and C. M. Krauland [General Atomics (GA)]; P. Gourdain, J. R. Davies, and E. M. Campbell (LLE); S. Fujioka (University of Osaka); and J. J. Santos and D. Batani (University of Bordeaux)

In the fast-ignition (FI) scheme of ICF, fuel compression to high densities and temperatures is achieved in separate processes. A high-energy (≥100-kJ), high-intensity ($\geq 10^{20}$-W/cm^2) short-pulse (~10-ps) laser is first used to create high-energy (~MeV) electrons (or ions), which then heat the precompressed fuel plasma to initiate ignition. One critical issue is the knowledge of the energy and number of relativistic electrons that can reach, and effectively heat, the core plasma. This unresolved issue warrants a new approach to observe the spatial energy deposition of relativistic electrons.

The objective of the UCSD NLUF project in collaboration with GA, LLE, the University of Bordeaux, and the University of Osaka is to systematically investigate the propagation and energy deposition of relativistic electrons in a preassembled cylindrical plasma under controlled conditions of density and temperature with and without an external magnetic field. Understanding the role of an external magnetic field in relativistic electron transport and energy deposition is important for several applications including ICF FI, isochoric heating, and the study of warm dense matter.

Our first NLUF experiment in 2017, which measured the time-dependent plasma conditions of an imploded cylinder with and without an external magnetic field, was successfully performed in the OMEGA chamber. This will be useful for the second experiment, which will reveal the temporal evolution of the plasma conditions with fast-electron energy deposition. In the first experiment, 36 beams (0.3 TW/beam, 1.5-ns square pulse) of the OMEGA laser were used to compress a Cl-doped CH foam cylinder to reach densities close to 7 g/cm^3. This implosion was characterized by two main diagnostic techniques: proton deflectometry and Cl spectroscopy. A schematic of the experimental layout is shown in Fig. 152.37. The cylinder (600-μm outer diameter and 540-μm inner diameter) was filled with 0.1 g/cm^3 of CH foam doped with 1% of Cl. In addition, one Cu foil and one Zn foil were attached to the cylinder's surface to decrease the magnetic mirror effect and allow K$_\alpha$ emissions during the second shot day. The protons used in proton deflectometry were created by a compressed D^{3}He capsule producing two energy populations: 3.5 MeV and 13 MeV. These protons, collected by CR-39, provided an image of the imploded cylinder deformed by the presence of the magnetic field. The Cl spectroscopy focused on the x-ray absorption of Cl 1*s*–2*p* transitions detected on axis. The back-

Table 152.VI: NLUF projects approved for FY17–FY18 funding and Omega Laser Facility shot allocations.

Principal Investigator	Institution	Title
A. Battacharjee	Princeton University	Dynamics of Magnetic Reconnection in High-Energy-Density Plasmas
F. N. Beg	University of California, San Diego	Transport of Relativistic Electrons in Cylindrically Imploded Magnetized Plasmas
R. P. Drake	University of Michigan	Experimental Astrophysics on the OMEGA Laser
T. S. Duffy	Princeton University	Phase Transitions and Crystal Structure of Tin Dioxide at Multi-Megabar Pressures
R. Jeanloz	University of California, Berkeley	High-Energy-Density Chemical Physics and Planetary Evolution
H. Ji	Princeton University	Particle Acceleration Resulting from Magnetically Driven Reconnection Using Laser-Powered Capacitor Coils
K. Krushelnick	University of Michigan	X-Ray Measurements of Laser-Driven Relativistic Magnetic Reconnection Using OMEGA EP
D. Q. Lamb	University of Chicago	Properties of Magnetohydrodynamic Turbulence in Laser-Produced Plasmas
R. Mancini	University of Nevada, Reno	Development of a Photoionized Plasma Experiment on OMEGA EP
R. D. Petrasso	Massachusetts Institute of Technology	Explorations of Inertial Confinement Fusion, High-Energy-Density Physics, and Laboratory Astrophysics
A. Spitkovsky	Princeton University	Study of Magnetized Collisionless Shocks in Laser-Produced Plasmas
D. Stutman	Johns Hopkins University	Demonstration of Talbot–Lau X-Ray Deflectometry Electron Density Diagnostic in Laser–Target Interactions
M. S. Wei	General Atomics	Hot-Electron Generation with 10^{16}-W/cm^2 Infrared Lasers in Shock-Ignition–Relevant Conditions

Table 152.VII: Graduate students participating in NLUF experiments in FY17.

Name	University	PI
Rui Hua	UCSD	Beg
Jonathan Peebles	UCSD	Beg
Shu Zhang	UCSD	Beg
Adrianna Angulo	University of Michigan	Drake
Patrick X. Belancourt	University of Michigan	Drake
Shane Coffing	University of Michigan	Drake
Joshua Davis	University of Michigan	Drake
Laura Elgin	University of Michigan	Drake
Jeff Fein	University of Michigan	Drake
Heath LeFevre	University of Michigan	Drake
Alex Rasmus	University of Michigan	Drake
Robert Vandervort	University of Michigan	Drake
Joseph Levesque	University of Michigan	Drake/ Hartigan
Rachel Young	University of Michigan	Drake/ Hartigan
Rajkrishna Dutta	Princeton	Duffy
Donghoon Kim	Princeton	Duffy
Han Sirus	Princeton	Duffy
Jack Matteucci	Princeton	Fox/ Schaeffer
Peter Heuer	UCLA/Princeton	Schaeffer
Abraham Chien	Princeton	Ji
Andrew Liao	Rice University	Hartigan
Thomas Batson	University of Michigan	Krushelnick
Paul Campbell	University of Michigan	Krushelnick
Amina Hussein	University of Michigan	Krushelnick
Archie Bott	Oxford University/ University of Chicago	Lamb
Alexandra Rigby	Oxford University/ University of Chicago	Lamb
Patrick Adrian	MIT	Petrasso
Neel Kabadi	MIT	Petrasso
Brandon Lahmann	MIT	Petrasso
Raspberry Simpson	MIT	Petrasso
Hong Sio	MIT	Petrasso
Graeme Sutcliffe	MIT	Petrasso
Cole Holcomb	Princeton	Spitkovsky

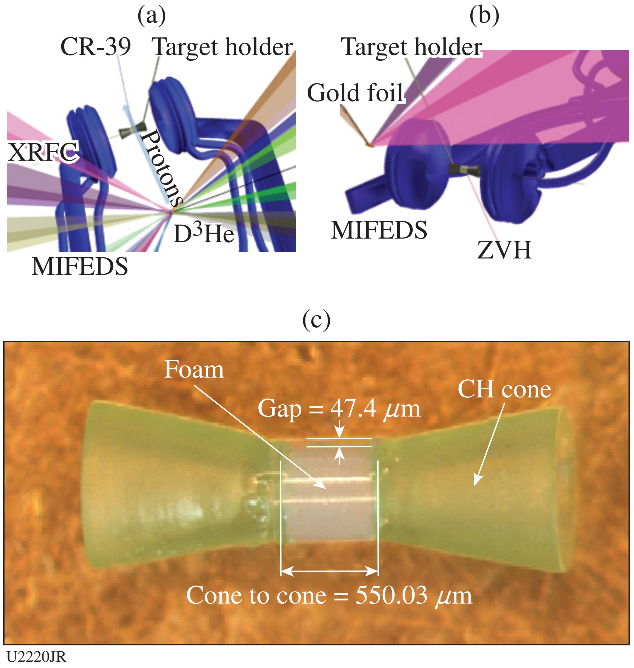

Figure 152.37
Schematic of (a) the proton deflectometry setup of the experiment in the OMEGA chamber and (b) the Cl-spectroscopy setup of the experiment in the OMEGA chamber; (c) a cylinder target with cones (made by GA) to prevent plasma interaction with the cylinder's surface. XRFC: x-ray framing camera; MIFEDS: magneto-inertial fusion electrical discharge system; ZVH: zinc von Hamos detector.

lighter for the absorption measurement was a gold foil irradiated by two pairs of stacked (0.3-TW/beam, 1.5-ns) OMEGA beams, creating a 3-ns x-ray source.

Our results show a cylindrical compression of the cylinder by the 36 OMEGA beams. The most important result is the impact of the external magnetic field on the compression. Figure 152.38 shows the temporally and spectrally resolved x-ray signal from the plasma with and without an external magnetic field. The compression time seems to be 0.5 ns later with a magnetic field, and we infer the electron temperature from the spectra of Cl. Another spectrometer [zinc von Hamos (ZVH)] was used to detect the Cu and Zn foil emissions with and without an external magnetic field. Furthermore, the x-ray pinhole charge-coupled device (CCD) shows a more-homogenous x-ray emission for the compression in the presence of an external magnetic field, indicating a more-homogenous compression. For proton deflectometry, the protons interacted with the cylinder at two different delays: 0.3 ns before and 2 ns after the time of laser incidence on the cylinder (the latter approximately corresponds to the implosion time). Figures 152.39(a) and 152.39(b) show the proton radiography of the cylinder deflected by the external magnetic field (estimated ~5.4 T), 0.3 ns before laser incidence and 2 ns after the laser pulse (after implosion time); the thermoelectric effect appears at the surface of the cone [Figs. 152.39(c) and 152.39(d)]. At this time, the cylinder's diameter can be observed and is directly related to the plasma density, revealing a difference in compression with or without the external magnetic field.

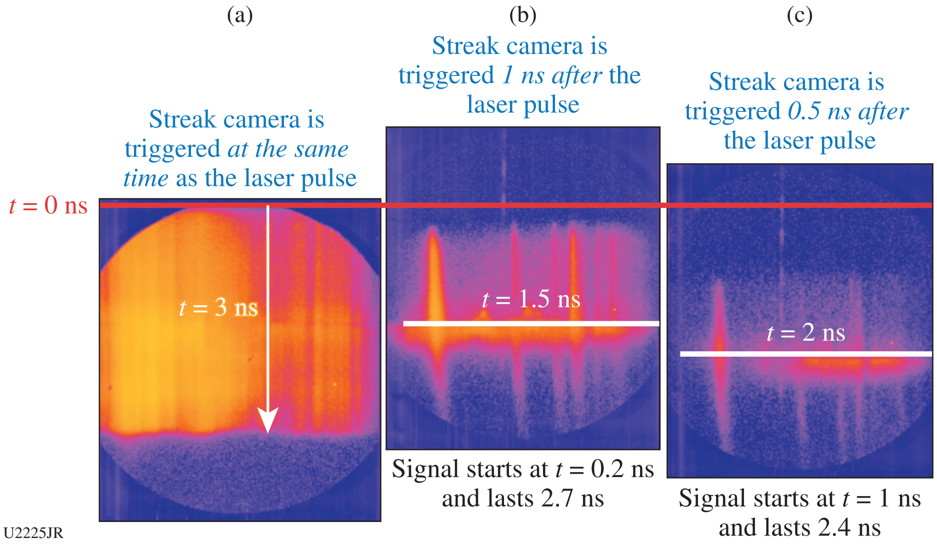

Figure 152.38
Temporally and spectrally resolved absorbed Cl signal (a) with backlighter only, (b) without an external magnetic field, and (c) with a magnetic field.

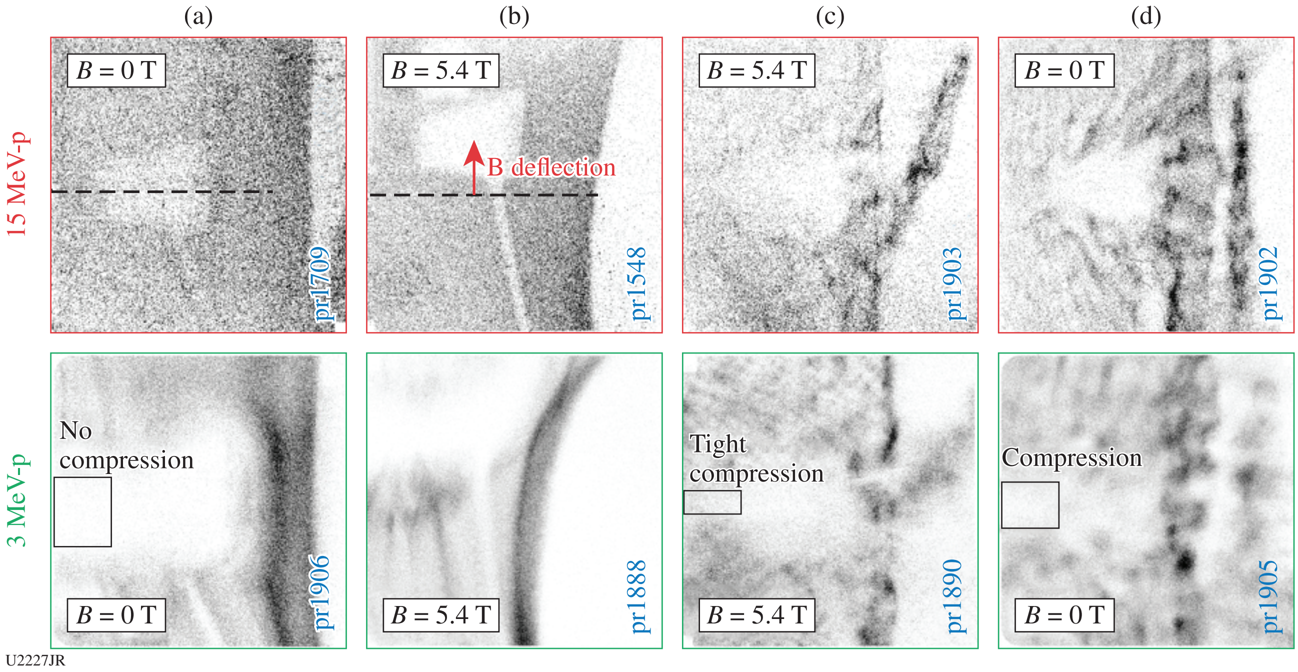

Figure 152.39
Proton deflectometry results for two delays (–0.3 and +2 ns from the laser) and with or without an external magnetic field: (a) 0.3 ns before the laser without a magnetic field, (b) 0.3 ns before the laser with a magnetic field, (c) 2 ns after the laser with a magnetic field, and (d) 2 ns after the laser without a magnetic field.

The data analysis and simulations are ongoing. Magnetohydrodynamic (MHD) simulations will be used to retrieve the compression history by matching the diagnostics at different times, and atomic physics codes will be used to determine the time-resolved plasma temperature inside the cylinder. Together, these will determine the best delay for the OMEGA EP beam on the second shot day.

Experimental Astrophysics on the OMEGA EP Laser

Principal Investigator: R. P. Drake (University of Michigan)

We study hydrodynamic processes by creating long-duration (tens of nanoseconds) steady shocks using the long-pulse UV laser beams on the OMEGA EP laser. Shocks encountering an interface with a density gradient generate shear or vorticity, depending on the geometry, which will induce either the Kelvin–Helmholtz instability (KH) or the Richtmyer–Meshkov (RM) process. Previously, we have independently studied the KH and RM processes; however, both processes will be induced if the interface is at an oblique angle. The contribution from each process depends on the interface angle. Our initial work aims to minimize the RM growth so that the KH growth dominates over time. We will do this by maximizing the parallel (shear) velocity and minimizing the perpendicular velocity.

The experimental target is shown in Fig. 152.40. Three UV laser beams are incident on an ablator package that includes a plastic layer and a plastic-doped bromine thermal insulator layer. This layer absorbs any laser preheat so it cannot adversely affect the target. The laser beams have a 1.1 full-width-at-half-maximum (FWHM) laser spot and a total energy of ~12 J; also, each of the 10-ns pulses is stacked in time to create an almost 30-ns laser pulse for an overall irradiance of ~4.2 × 10^{13} W/cm^2. This long, steady laser pulse creates a strong shock in the ablator package, is then driven into a 100-mg/cm^3 carbon foam, and is finally incident on an oblique interface in a plastic material. The interface has a precision-machined sinusoidal pattern that is either a single mode ($\lambda = 100\ \mu$m, $a = 5\ \mu$m) or dual mode ($\lambda_1 = 100\ \mu$m, $a_1 = 2.5\ \mu$m, $\lambda_2 = 50\ \mu$m, $a_2 = 5\ \mu$m). Our goal is to compare the developing structure with a single mode (where no merger is expected) and the dual-mode case. We also have experimental targets with a planar interface.

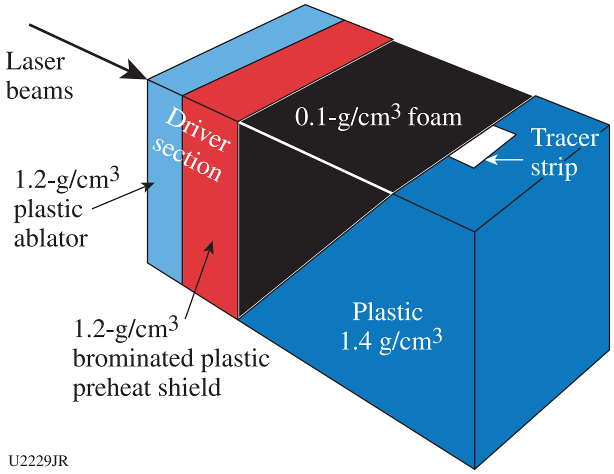

Figure 152.40
Schematic of vortex merger target showing the unstable interface between the low- and high-density material at 40°.

The evolution of the vertical structures was imaged with a spherical crystal imager (SCI) using Cu K$_\alpha$ radiation at 8.0 keV. Figure 152.41 shows an example of a high-resolution, high-

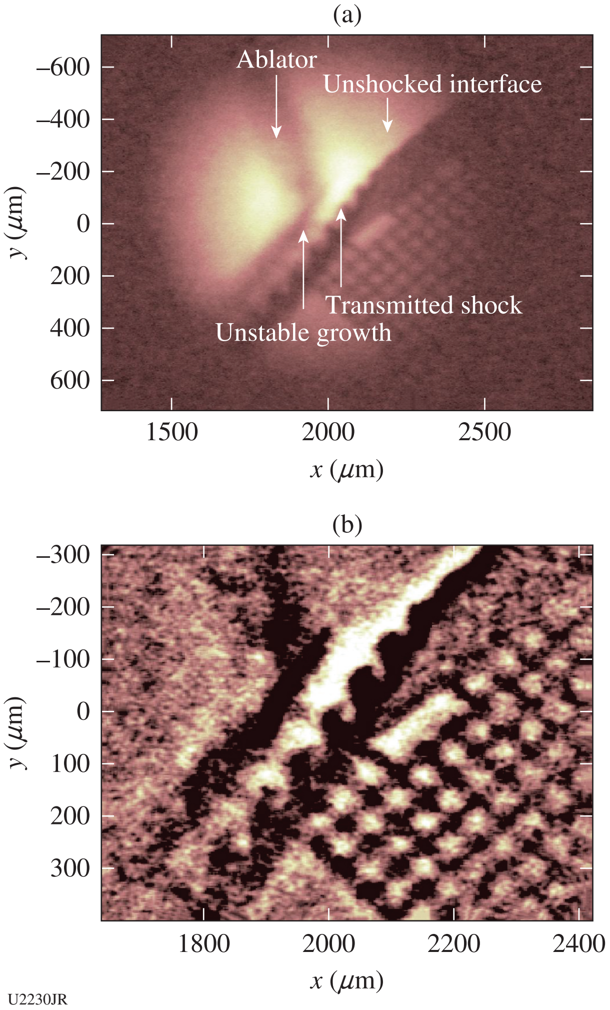

Figure 152.41
(a) X-ray radiograph of an experimental target using a single-mode initial condition at an oblique interface. (b) The radiograph has been cropped and processed to better visualize the unstable growth at the interface.

signal-to-background x-ray radiograph with several notable features indicated. The unperturbed interface is in the upper right portion of the image in Fig. 152.41(a). The shock front is barely visible in the foam, but the position can also be determined from the transmitted shock in the plastic component. The dark, curved feature on the left in Fig. 152.41(a) is the ablator package, which collided with the interface in the lower part of the image and is approaching the interface in the upper part of the image. Between the ablator and shock front, vortex structures can be seen growing. This experimental target had a single-mode interface and was imaged at 65 ns from the start of the main laser pulse. Future experiments will vary the angle of the oblique interface in order to change the contributions of the RM and KH processes.

Phase Transitions and Crystal Structure of Tin Dioxide at Multimegabar Pressures

Principal Investigator: T. S. Duffy (Princeton University)
Co-investigators: R. F. Smith and F. Coppari (LLNL);
J. K. Wicks (Princeton University); and T. R. Boehly (LLE)
Graduate Students: D. Kim and R. Dutta (Princeton University)

Silica is the most abundant oxide component of terrestrial mantles and serves as an archetype for the dense, highly coordinated silicates of planetary interiors. Understanding the behavior of silica at ultrahigh pressure is necessary to model the structure and dynamics of large rocky exoplanets known as super-Earths. Pressures in the mantles of such exoplanets may exceed 1 TPa, which is beyond the range of standard static high-pressure experimental techniques. Dynamic compression using the OMEGA laser offers an alternative means to explore structures and equations of state of planetary materials at these extreme conditions.

SiO_2 is one of a family of dioxides whose high-pressure behavior has been of strong interest because of their extensive polymorphism, highly coordinated structures, and varied transition pathways. The challenge in structure determination of silicates and oxides at exoplanet interior pressures is to obtain sufficient x-ray diffraction intensity from weakly diffracting, low-symmetry phases at ultrahigh pressures. The use of analog materials that undergo similar phase transition sequences at lower pressures has a long history in geoscience and high-pressure research and provides a useful pathway for the exploration of high-pressure structures. In this study, we have examined the behavior of SnO_2 at exoplanetary conditions using OMEGA and OMEGA EP. In addition to its role as an analog material, tin oxide is also of interest since its high-pressure phases have been predicted to be potential ultra-incompressible materials.

Our ramp compression experiments use a target package consisting of a thin sample foil sandwiched between a diamond pusher and a LiF window. The OMEGA laser is used to ablate the diamond front surface driving a ramp compression wave into the sample. A quasi-monochromatic x-ray source is generated by irradiating a metal foil to create predominately He-like x rays. *In-situ* x-ray diffraction is performed using the powder x-ray diffraction image-plate (PXRDIP) diagnostic. The pressure is determined from measurements of the free-surface velocity of the sample/lithium fluoride interface.

We have carried out density-functional-theory calculations that indicate that tin oxide is expected to transform from the orthorhombic cotunnite-type phase to the hexagonal Fe_2P-type structure above 200 GPa. Our measured x-ray diffraction data for SnO_2 are ~300 GPa and are shown in Fig. 152.42. We observe multiple diffraction lines from the sample, indicating that we have the potential to constrain high-pressure structures and equations of state at multi-megabar pressures for SnO_2. Analysis to distinguish among the possible crystal structure at this pressure is ongoing. In future work, we will extend these measurements to higher pressure as well as study the behavior of other dioxides including GeO_2 and SiO_2.

Dynamics of Magnetic Reconnection in High-Energy-Density Plasmas

Principal Investigators: W. Fox (Princeton Plasma Physics Laboratory); D. Schaeffer and A. Bhattacharjee (Princeton University); G. Fiksel (University of Michigan); and D. Haberberger (LLE)

We have developed and conducted experiments on the OMEGA and OMEGA EP Laser Systems to study the related phenomena of magnetic reconnection and collisionless shocks. Magnetic reconnection occurs when regions of opposite directed magnetic fields in a plasma can interact and relax to a lower-energy state; it is an essential plasma-physics process that governs the storage and explosive release of magnetic energy in systems such as the Earth's magnetosphere, the solar corona, and magnetic-fusion devices. The energy thereby liberated can produce heat flows and can enable the acceleration of a large number of particles to high energies. During previous NLUF reconnection experiments on OMEGA EP, we also unexpectedly observed the formation of magnetized collisionless shocks. Like reconnection, collisionless shocks are common in space and astrophysical systems. Magnetized shocks form from the nonlinear steepening of a magnetosonic wave and convert highly kinetic supersonic inflows to high-pressure subsonic outflows. In the process, they can also accelerate particles to

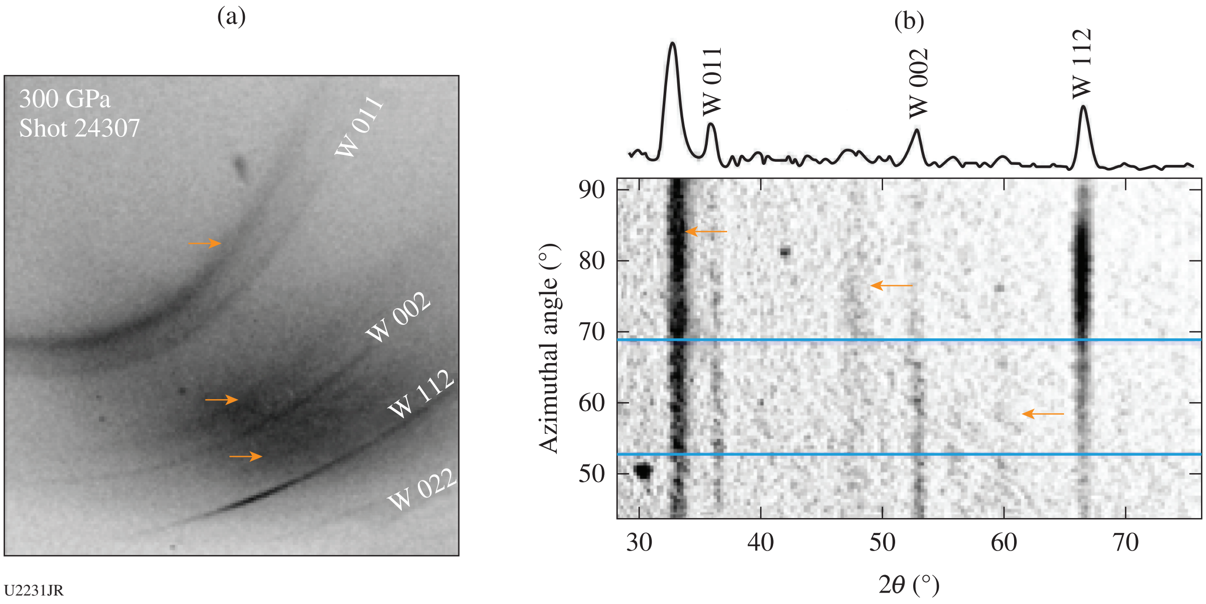

Figure 152.42
Diffraction data for SnO_2 at 300 GPa. (a) One of the image plates for shot 24307. Lines from the tungsten pinhole (used for collimation and calibration) are labeled. Diffraction lines from the sample are indicated with orange arrows. (b) Image-plate data transformed to ϕ, 2θ coordinates, where ϕ is the azimuthal angle around the incident x-ray beam and 2θ is the diffraction angle. A lineout from the region between the blue horizontal lines is shown at the top of (b). Again, peaks from SnO_2 are indicated with orange arrows. These results demonstrate that diffraction data can be obtained from weakly scattering, low-symmetry oxide samples at high pressures using the OMEGA laser.

extremely high energies. Those experiments were recently published in Ref. 1 and are under review in Ref. 2 as part of an invited talk at the 58th APS DPP meeting.

In this campaign we successfully carried out two experimental shot days on OMEGA EP and one shot day on OMEGA. The experiments on OMEGA EP utilized a new flat-foil platform for studying Biermann-mediated reconnection, while the experiments on OMEGA ported the magnetized colliding plasmas platform developed previously by our group and first published in Ref. 3.

The experiments on OMEGA EP used magnetic fields generated by the Biermann battery effect as the seed field for reconnection. Two oppositely directed Biermann fields were driven by the interaction of two lasers with a flat-foil target. Unlike previous Biermann-mediated experiments, our experiments utilized a flat target with a gap between the laser spots to provide a low-density region where the two laser plumes collide. The experiments on OMEGA used a single MIFEDS-driven coil but were otherwise similar to our MIFEDS platform developed for our previous NLUF campaigns on OMEGA EP.

The first shot day (March 2017) on OMEGA EP used proton radiography and the recently developed single-channel electron spectrometer (SC-ESM) to study the interaction between expanding plasma plumes and the resulting electron acceleration. We obtained spectacular proton radiography images that measure the magnetic field (see Fig. 152.43). Proton radiographs showed significant generation of Weibel filamentation and plasmoid formation in the gap region, which indicates fast reconnection. The SC-ESM also observed a population of energized electrons. This population was consistent with reconnection-accelerated particles but could also be caused by laser–plasma interaction (LPI) effects.

The second shot day (July 2017) on OMEGA used the Thomson-scattering diagnostic to measure the temperature and density of a single plasma plume interacting with a background magnetic field and ambient plasma (see Fig. 152.44). These measurements complement previous efforts on OMEGA EP that used proton radiography and angular filter refractometry (AFR) to diagnose large-scale magnetic topology and density profiles. They also provided information on conditions necessary for magnetized collisionless shock formation. We successfully obtained data at a range of times, distances from the target, ambient plasma conditions, and magnetic-field conditions. The results filled in several previous gaps. The measurements directly give plasma parameters and agree well with the 2-D radiation–hydrodynamics code *DRACO*. They also indicate that the formation of magnetized shocks is sensitive to the configuration of the main laser beams. The experiments, and their extension to counter-streaming plumes, will be continued on an upcoming NLUF shot day.

The third shot day (August 2017) on OMEGA EP continued the previous experiments on Biermann-mediated reconnection. We used AFR, which was unavailable on the previous shot day, proton radiography, and the SC-ESM to study the interaction of the colliding plumes. We obtained excellent AFR images, which show a complex interplay between magnetic turbulence and reconnection (see Fig. 152.43). The combination of proton and AFR images are currently being analyzed and compared to particle-in-cell simulations. We saw similar energized electron populations as on the first OMEGA EP day, but we also confirmed using the sub-aperture backscatter (SABS) diagnostics that LPI may play a significant role in energizing particles. This will be pursued in upcoming NLUF experiments.

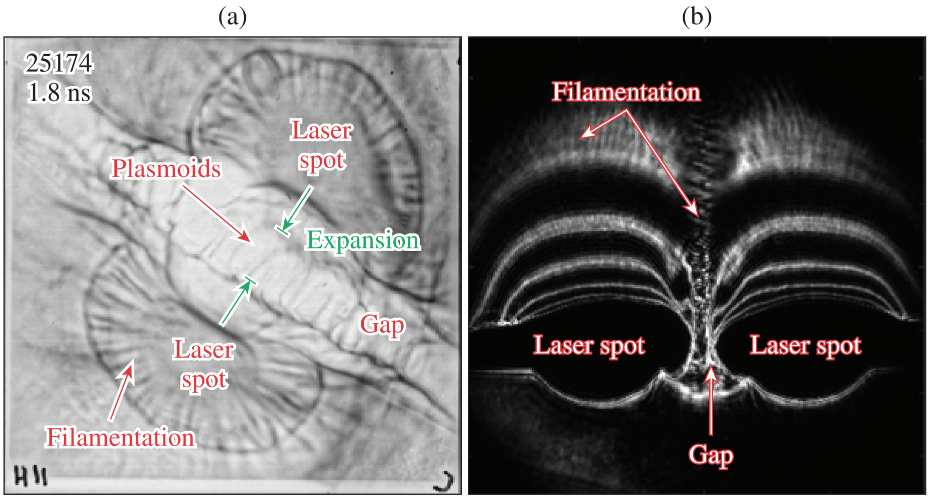

U2309JR

Figure 152.43
Interaction of two Biermann-generated magnetic plumes 1.8 ns after laser ablation on OMEGA EP. The gap in the flat-foil target can be seen between the laser spots. (a) Proton radiography reveals the formation of Weibel filaments at the edge of the Biermann fields and plasmoids in the gap region. (b) AFR also shows the formation of filamentation at the plume edges and in the gap region.

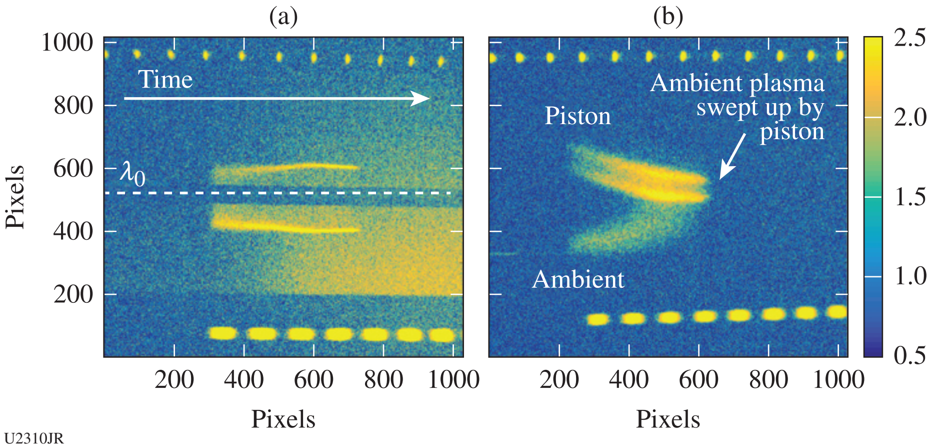

U2310JR

Figure 152.44
Streaked Thomson-scattering measurements of the interaction of a piston plasma with a magnetized ambient plasma: (a) electron plasma wave feature and (b) ion-acoustic wave feature. The scattered spectra show that the ambient ions are swept up by the piston and form a hot, high-density downstream region.

Magnetized Accretion Shocks and Magnetospheres in the Laboratory

Principal Investigator: P. Hartigan (Rice University)

Co-investigators: C. C. Kuranz, G. Fiksel, J. Levesque, and R. Young (University of Michigan); J. Foster and P. Graham [Atomic Weapons Establishment (AWE)]; A. Frank (University of Rochester); A. Liao (Rice University); C. K. Li and R. D. Petrasso [Massachusetts Institute of Technology (MIT)]; and D. H. Froula (LLE)

The goal of our NLUF campaign is to use the magneto-inertial fusion electrical discharge system (MIFEDS) on OMEGA to create analogs of magnetized, hypersonic plasma flows that are ubiquitous in astrophysics. In previous experiments we explored several related topics, including the dynamics of magnetized star-forming clouds, magnetized supersonic Kelvin–Helmholtz instabilities, stellar magnetospheric infall, and planetary magnetospheres. Our current experiments relate most closely to stellar wind interactions with atmospheric outflows from magnetized exoplanets. The experimental setup drives a supersonic flow that impinges upon a current-carrying wire, producing a bow shock. Ablation flow from the wire encounters the supersonic flow, creating a working surface where the flows meet. Altering the amount of current in the wire changes the strength of the magnetic field in the ablation flow.

Last year we succeeded in producing a layer of concentrated magnetic flux embedded in the strongly shocked plasma of the working surface. However, the optical imaging diagnostics we used did not spatially resolve this layer well, and parts of the shocked layers were optically thick, preventing us from directly probing this layer where the two flows collide. To improve upon this design, in FY17Q1 we deployed two new diagnostic techniques that both penetrate into the working surface. First, we used spatially resolved Thomson scattering as a means to map how the velocities and densities vary across the shocked layers. In the spectra shown in Fig. 152.45(a) both the ablation flow from the wire (left side of the image in blue) and the incident flow that is driven from the laser target (right side of image in blue) are traced as a function of position. The two flows collide to generate a shocked layer with high temperature and density. According to theoretical models, the field in the wire should be swept by the ablation flow into a compressed layer that coincides with the working surface.

To diagnose the field geometry and strength, we employed proton radiography (Fig. 152.46). The results, which are quite striking, show the two main characteristics predicted by the simulations: (1) a voided area caused by protons being deflected away from the wire by the toroidal field caused by the current in the MIFEDS wire, and (2) a caustic produced by the

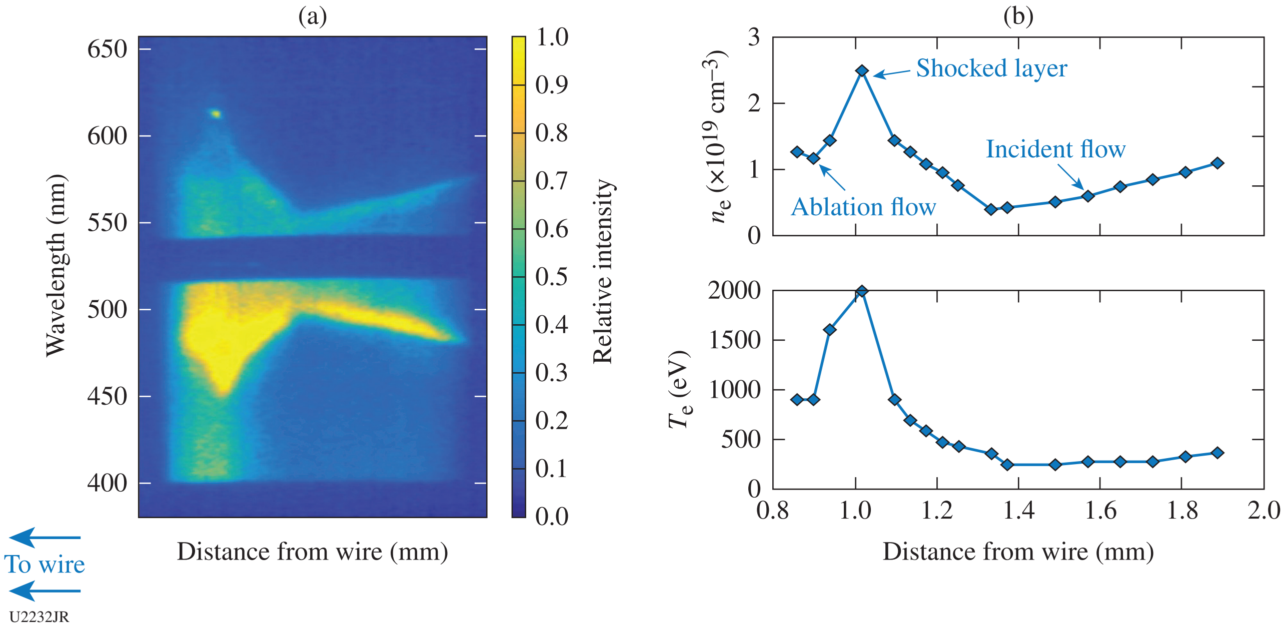

Figure 152.45
(a) Electron wave spectra resolved across the magnetized shock and (b) derived quantities. The density profile indicates a shock at the d = 1-mm position of ~100-μm thickness at half maximum.

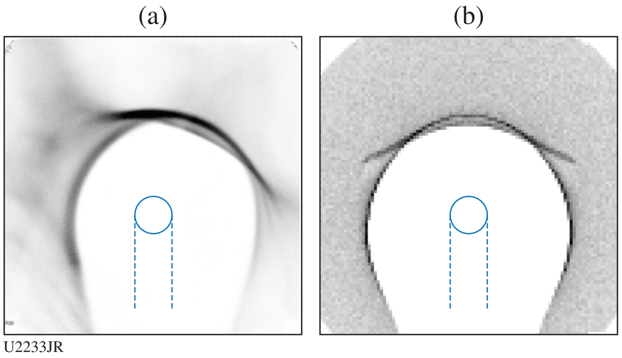

Figure 152.46
(a) Real and (b) synthetic 3-MeV proton radiographs with a fiducial, indicating the actual location of the wire (blue). The synthetic image (b) was constructed by placing a flux layer in the deprojected magnetic-field model with the position and thickness indicated by the electron plasma wave–derived shock structure (see Fig. 152.45). The apparent position of the flux layer (brimmed hat) defines the magnetized flux layer coincident with the shocked gas.

accumulation of magnetic flux in the working surface. These observations allowed us to characterize the thickness and density of the magnetized flux sheet. Interestingly, the flux density we derived from the proton radiography was significantly less than that predicted by pressure equilibration; diffusion of the magnetic field resulting from inertial ions is a likely cause of these differences.

This experiment will serve as a template for future studies of magnetized shock layers. Following the temporal evolution of the system is a promising area of research, and with small changes to the experimental setup we should be able to further improve the spatial resolution and possibly measure the degree of mixing between the two fluids within the working surface.

Our NLUF research currently supports the thesis preparation of three graduate students in laboratory astrophysics: A. Liao (Rice University), and J. Levesque and R. Young (University of Michigan).

Influence of Plasma Density on the Generation of Hundreds of MeV Electrons via Direct Laser Acceleration

Principal Investigators: A. E. Hussein, T. Batson, K. Krushelnick, and L. Willingale (University of Michigan); A. V. Arefiev (UCSD); P. M. Nilson, D. H. Froula, R. S. Craxton, A. Davies, and D. Haberberger (LLE); and H. Chen and G. J. Williams (LLNL)

The OMEGA EP Laser System was used to study the acceleration of electrons to many times the ponderomotive energy by high-energy, picosecond-duration laser pulses interacting with an underdense plasma target. A high-intensity picosecond pulse propagating through underdense plasma will expel electrons along its path, forming a positively charged plasma channel.[4] Electrons that are injected into this channel can gain significant energy through direct acceleration by the laser field.[5] This acceleration mechanism is known as direct laser acceleration (DLA). Experiments on the OMEGA EP laser employed four of the chamber beams to study, optimize, and diagnose the influence of plasma density on the DLA mechanism. The existence of an optimal plasma density for the generation of high-energy, low-divergence electron beams was demonstrated. This result is consistent with results from 2-D particle-in-cell (PIC) simulations using the code *EPOCH*.

A schematic of the experiments on OMEGA EP is given in Fig. 152.47. A long-pulse UV beam (2.5 ns, 1200 J) ionized a CH flat-foil target to generate an expanding plasma plume. The backlighter beam (1 ps, 400 J) interacted with the plasma plume in an oblique geometry to generate a channel and accelerate an electron beam. The plasma density was varied by changing the timing between the long-pulse UV beam and the short-pulse (backlighter) beam. The sidelighter beam (1 ps, 200 J) was focused onto a Cu foil to generate a proton probe via target normal sheath acceleration (TNSA) for imaging electromagnetic fields onto a stack of radiochromic film (RCF). Shadowgraphy imaging, polarimetry of magnetic-field formation, and plasma density measurements by angular filter refractometry (AFR) were fielded using the 4ω optical diagnostic probe. The electron spectrum along the axis of the short-pulse beam was measured

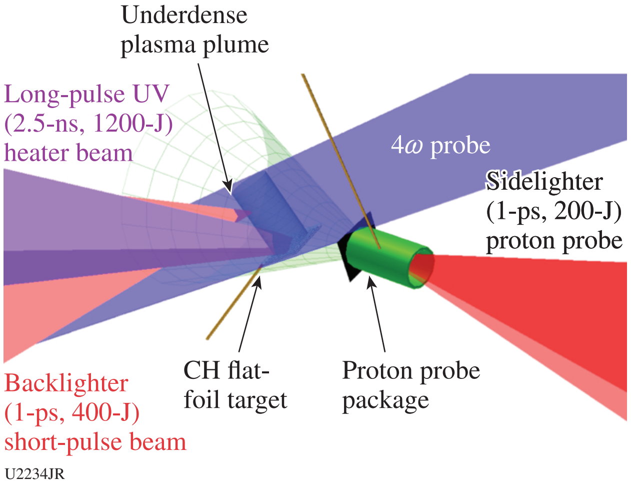

Figure 152.47
Experimental configuration. A long-pulse beam generated an expanding CH plasma plume as the target of the short-pulse beam for channel formation and electron acceleration by direct laser acceleration.

using an absolutely calibrated magnetic spectrometer [electron positron proton spectrometer (EPPS)].

Previous experiments explored the formation and evolution of plasma channels on an RCF film stack.[4,5] In these images, the upward deflection of DLA-accelerated electrons was observed as a result of the refraction of the laser pulse in the plasma-plume density gradient.[5] AFR measurements of plasma-plume expansion were used to extract a 2-D Gaussian density profile. This density profile agreed reasonably with density profiles of a CH expanding plasma plume obtained using the 2-D hydrodynamic code *SAGE*.

Two-dimensional PIC simulation conditions were designed to match the OMEGA EP Laser System. A 1.053-μm-wavelength laser, with coincident focal spots of 3.4 μm and 17 μm, with intensities of 3.776×10^{19} W/cm^2 and 2.81×10^{18} W/cm^2, respectively, was simulated. The plasma density profile was defined by the Gaussian profile from AFR measurements. Simulations were performed with a resolution of 30 cells per wavelength in the longitudinal direction (x) and six cells per wavelength in the transverse direction (y). The laser was linearly polarized in y and propagated in x. Ions were treated as mobile, and the plasma (electron) density was varied to simulate the temporal evolution of the plasma plume in experiments. Simulated densities ranged between 0.1 n_c and 0.008 n_c, where the quoted value corresponds to the peak density along the laser trajectory and n_c is the critical density.

Simulated electron spectra are shown in Fig. 152.48(a) and reveal the existence of an optimal plasma density for electron acceleration to energies exceeding 230 MeV. Experimental electron spectra are shown in Fig. 152.48(b). The quoted density in this figure refers to the peak electron density along the trajectory of the main interaction beam, as estimated by *SAGE* simulations and AFR measurements. Experimental measurements revealed an enhancement of peak electron energy at a peak density of 0.01 n_c. The enhancement of peak electron energy, up to nearly 600 MeV, was significantly higher than predicted by 2-D simulations.

The proton-probe diagnostic captured electromagnetic-field structures of the plasma channel. Although the initial time t_0 of the short-pulse interaction cannot be exactly determined because of timing jitter of the order of 20 ps, relative timing between each film in the RCF stack can be calculated from proton time-of-flight calculations. An example radiograph is given in Fig. 152.49(a), where clear formation and filamentation can be observed using a normal film pack, 8 cm from the interaction region. The centroid of the resultant electron beam on another RCF stack was found to deflect above the axis of laser propagation, as shown in Fig. 152.49(b). This is consistent with upward refraction of the laser pulse in the density gradient. Information about beam pointing and angular divergence as a function of plasma density could be extracted from the on-axis RCF stack. Beam divergence tends to decrease as a function of plasma density, with some evidence of channel filamentation, creating multiple beamlets, at lower densities.

These experiments demonstrated the existence of an optimal plasma density for the generation of high-energy electron beams by the interaction of a high-intensity picosecond pulse with underdense plasma. Experimental results also indicate a relation between plasma density and beam divergence. Continued work will focus on the role of quasi-static channel fields on

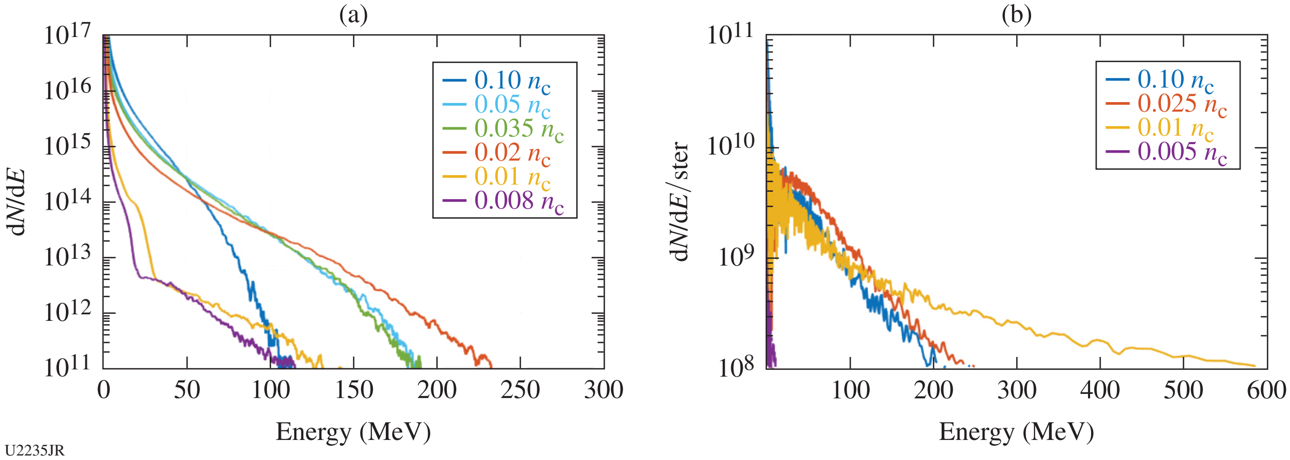

Figure 152.48
(a) Electron spectra simulated for various peak densities and (b) experimental measurements of electron spectra along the axis of the short-pulse beam.

electron energy enhancement, beam pointing, and divergence to elucidate the mechanisms and action of DLA at different plasma densities.

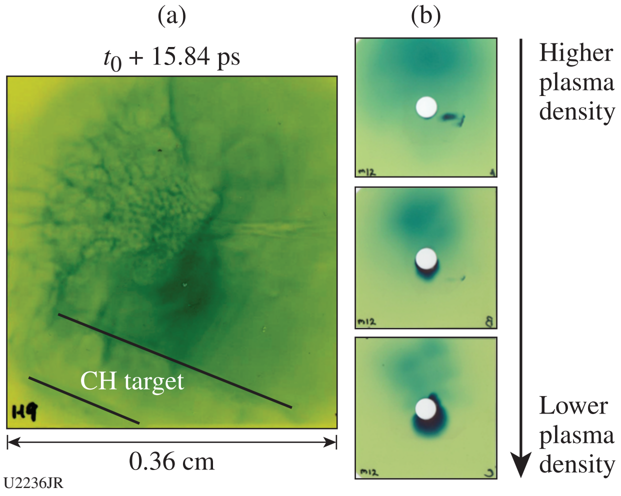

Figure 152.49
(a) Proton probe image of a plasma channel. (b) Radiochromic film along the axis of short-pulse (backlighter) beam propagation can be used to study electron beam pointing and divergence as a function of plasma density.

High-Energy-Density Chemical Physics and Planetary Evolution

Principal Investigator: R. Jeanloz (University of California, Berkeley)
Co-investigators: M. A. Millot, D. E. Fratanduono, P. M. Celliers, and J. H. Eggert (LLNL); S. Brygoo and P. Loubeyre (CEA); and T. R. Boehly, G. W. Collins, and J. R. Rygg (LLE)

During FY17, our international research team conducted two campaigns with diamond-anvil cell targets on the OMEGA laser (DirectDAC17A and 17B) for a total of 16 shots. The configuration is a direct-drive geometry (Fig. 152.50), with up to 12 beams delivering up to 6 kJ in 1-ns square pulses to the 1-mm aperture in the tungsten carbide seats holding the diamond anvils. VISAR (velocity interferometer system for any reflector) velocimetry and streaked optical pyrometry monitored the shock propagation in the sample pressure chamber to diagnose the pressure–density equation of state and the optical properties (reflectivity, absorption coefficient) using a quartz reference.[6] Most of the shots were dedicated to the study of the metallization of hydrogen (deuterium) using the combination of high precompression (6 to 13 GPa) and double shock

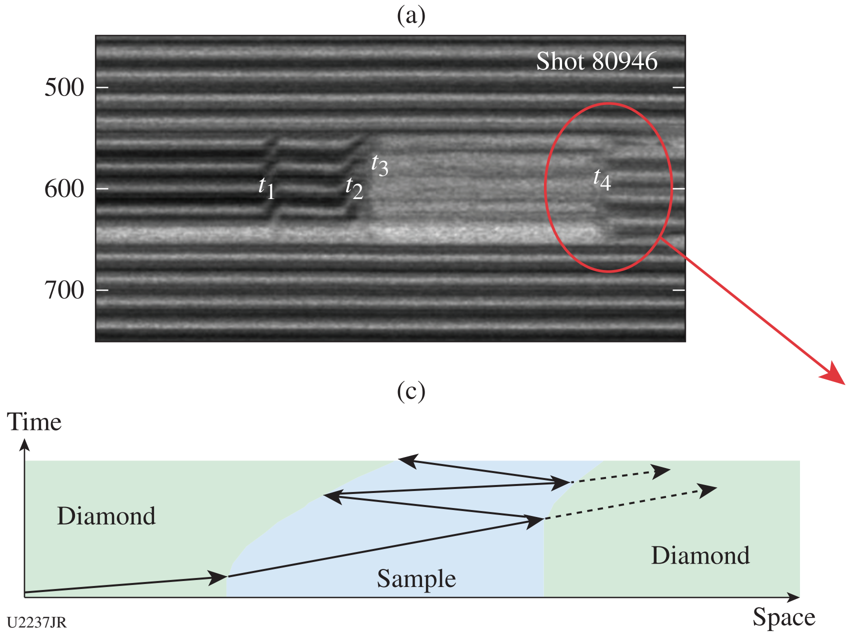

Figure 152.50
(a) Typical VISAR velocimetry record and (b) sketches of the re-shock experimental configuration showing the arrival of the elastic wave at the diamond/sample interface (t_1), followed by the arrival of the inelastic wave (t_2) and the catchup of these two waves inside the D_2 sample, transforming it in an opaque fluid. (c) Impedance mismatch at the arrival of the shock wave at the sample/diamond interface induces the generation of a second shock wave into the deuterium sample (t_4). The bright fringes after t_4 indicate that deuterium becomes a good reflector upon reshock, indicative of high electrical conductivity.

compression to access high-density states in the vicinity of the predicted first-order transition from the insulating molecular fluid to a metallic atomic fluid.

Our team also successfully demonstrated the feasibility of using diamond-anvil cell targets on the OMEGA EP laser during a one-day campaign. Preliminary analysis of the data indicates that OMEGA EP makes it possible to reach higher shock pressures using longer pulse durations. Future experiments might also benefit from the excellent pulse-shape capability available on OMEGA EP to generate multishock compression and map out the metallization transition of several key planetary constituents.

Prepared by LLNL under Contract DE-AC52-07NA27344. LLNL-TR-739623.

Particle Acceleration Resulting from Magnetically Driven Reconnection Using Laser-Powered Capacitor Coils

Principal Investigator: H. Ji (Princeton University)
Co-investigator: L. Gao (Princeton Plasma Physics Laboratory)

Magnetic reconnection is a ubiquitous astrophysical phenomenon in which magnetic energy is rapidly converted into plasma kinetic energy in the form of flow energy and thermal energy as well as nonthermal energetic particles. Energy particles are often regarded as an observational signature of the magnetic reconnection, which can be a more-efficient generation mechanism than other competing processes such as collisionless shocks. Despite its long history, most laboratory work in this area has focused on the mechanisms of fast reconnection as well as the generation of plasma flow and thermal energy during magnetic reconnection, mostly resulting from the limitations in either experimental setups or diagnostic capabilities. The goal of our research is to build an effective new platform to achieve and measure conspicuous particle acceleration by magnetically driven axisymmetric reconnection using laser-powered capacitor coils. In FY14, our team successfully measured and reported the first direct measurement of the magnetic fields generated by these laser-powered capacitor coils. With strong magnetic fields approaching the MG level and by tuning plasma parameters, we will be able to access magnetically driven, collisionless reconnection for efficient particle acceleration.

In FY17, we successfully carried out one experimental shot day on OMEGA EP to study the above-mentioned physics goals. A schematic of the experimental setup on OMEGA EP is shown in Fig. 152.51. The main interaction target is comprised of two parallel copper plates connected by two copper wires. Two OMEGA EP 2.5-kJ, 1-ns laser pulses pass through the laser entrance holes on the front plate and are focused on the back foil, generating a beam of superthermal hot electrons. The hot electrons stream onto the front plate and build up an electrical potential between the plates. This in turn drives

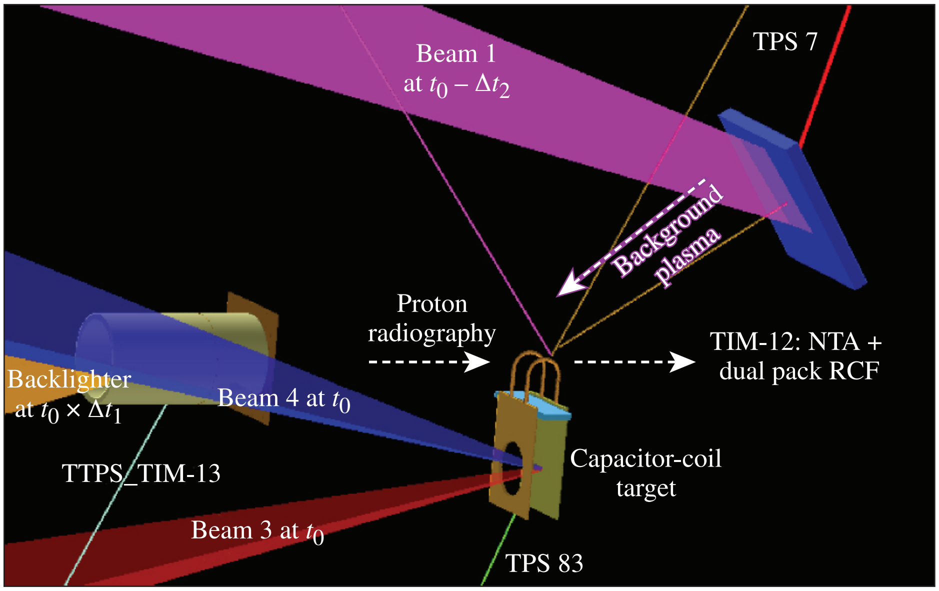

Figure 152.51
Experimental setup for the recent reconnection experiments on OMEGA EP based on the laser-powered capacitor coils. BL: backlighter; NTA: near-target arm; TIM: ten-inch manipulator; TPS: target positioner system; TTPS: TIM target positioner system.

large currents in both wires and creates magnetic reconnection because antiparallel magnetic-field lines exist in the middle plane. Another OMEGA EP 50-J, 1-ns laser pulse irradiates a plastic target and generates a tenuous background plasma for the reconnection region.

A suite of existing OMEGA EP diagnostics were fielded to identify quantitative confirmation of reconnection. Ultrafast proton radiography was utilized to probe the reconnection process at various times with high spatial and temporal resolutions. The new OMEGA EP high-resolution x-ray spectrometer (HiRes) was fielded to monitor Cu K_α emission from both front and back Cu plates. Three fixed port x-ray pinhole cameras viewed the time-integrated x-ray emission from the entire target. The Osaka University electron spectrometer was used to measure the particle spectrum from reconnection. The HiRes data showed strong Cu K_α emission from the front Cu plate, indicating hot electrons generated during the main interaction streaming onto the front plate and exciting these K-shell emissions. This measurement is a direct confirmation of the charging mechanism for building the electrical potential between the two plates. The hot electrons therefore have energies of at least 8 keV. Detailed atomic physics analysis is ongoing to understand the spectrum of hot electrons generated when the two main laser pulses hit the back copper foil. This will facilitate a better understanding of the mechanism for creating these strong magnetic fields. Our electron spectrometer data consistently showed a peak in the electron power spectrum with maximum electron energy ~1 MeV from reconnection. These experimental results are being compared with our PIC simulations.

X-Ray Measurements of Laser-Driven Relativistic Magnetic Reconnection Using OMEGA EP

Principal Investigators: K. Krushelnick, P. Campbell,
L. Willingale, and G. Fiksel (University of Michigan);
and P. M. Nilson and C. Mileham (LLE)

Recent experiments were conducted on the OMEGA EP Laser System to study a magnetic-reconnection geometry established by firing a short-pulse laser alongside a long-pulse UV beam onto solid targets. A 1-ns, 1250-J UV beam was focused to an intensity of 2×10^{14} W/cm^2 onto a 25-μm-thick copper target. Misalignment of temperature and density gradients in the ablated plasma plume generated azimuthal Biermann battery magnetic fields (of the order of MG). As this long-pulse–produced plasma developed, a 10-ps pulse containing 500 J was focused to relativistic intensity ($I > 10^{18}$ W/cm^2) in close proximity. In contrast to the slowly expanding Biermann battery fields ($v \approx c_s$), relativistic currents driven by the short-pulse laser generate a strong azimuthal magnetic field (of the order of 10 to 100 MG) that spreads radially with a velocity near the speed of light. This dramatic difference in scales yields a highly asymmetric field geometry, with the rapidly expanding short-pulse–generated field driving into a quasi-static Biermann battery field.

Proton radiography was implemented to diagnose the magnetic-field dynamics of the interaction. A second short-pulse laser (300 J in 1 ps) accelerated protons via the TNSA mechanism from 20-μm-thick gold targets to energies exceeding 60 MeV. A stack of RCF detected the deflection of the proton beam by the electromagnetic fields of the target. The time of flight for a proton depends on the kinetic energy. Because of the Bragg peak in the proton stopping power, each layer in the RCF stack detects a different energy and therefore a different time in the interaction.

As shown in Fig. 152.52, the proton radiography captures the rapid expansion of the short-pulse–generated magnetic field

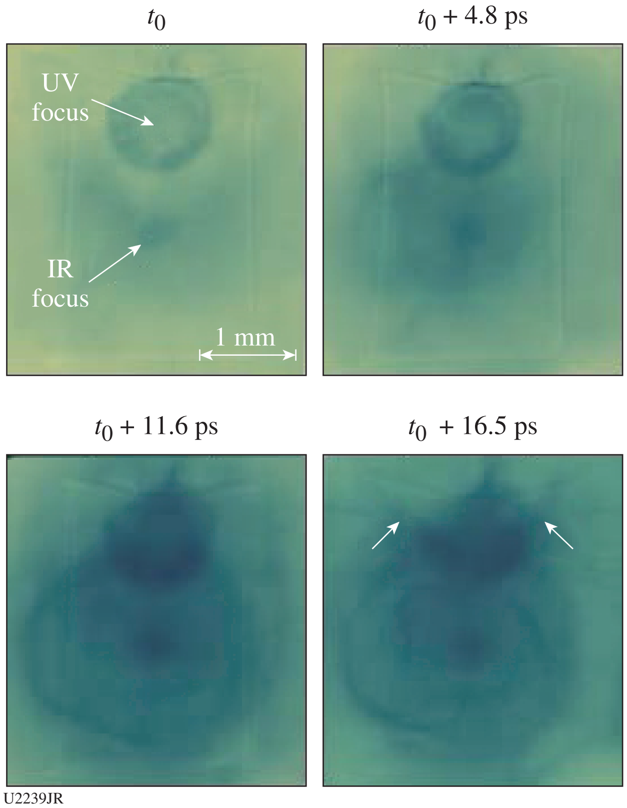

Figure 152.52
Proton radiography captures the interaction of the rapidly expanding, short-pulse–generated magnetic field with the quasi-static Biermann battery field. Superimposed arrows at time = t_0 + 16.5 ps indicate the regions of enhanced signal potentially associated with outflows.

into the quasi-static Biermann field. At t_0, the Biermann field has evolved for 750 ps when the short-pulse IR beam arrives on target and the focal-spot separation is 1.25 mm. After 11.6 ps, there is a local enhancement in proton flux along the edge of the Biermann field structure as the fields meet and interact, indicating a strengthening of the field gradient. At later times, there is evidence of outflow structures emanating from the magnetic-field interaction.

In future experiments, the relative beam timing and focal-spot separation will be tuned to optimize and study these features of the interaction. The copper targets will be replaced with a lower-Z material to improve the quality of the proton radiography, and the dimensions will be increased to mitigate target-edge effects. In addition to the experiments, our future work will include a quantitative analysis of the proton-radiography results, moving toward full 3-D PIC simulations.

Properties of Magnetohydrodynamic Turbulence in Laser-Produced Plasmas

Principal Investigator: D. Q. Lamb (University of Chicago)

During the first shot day (19 April 2017) of our experiments (TDYNO NLUF Campaign) we used the OMEGA laser to study the turbulent dynamo amplification of magnetic fields, a ubiquitous process in astrophysical systems. The experiments employed a platform (Fig. 152.53) similar to the one we fielded on OMEGA for our very successful first TDYNO Campaign (FY15–FY16), during which we demonstrated nonlinear amplification by turbulent dynamo for the first time in a laboratory environment. The main goal of our first shot day was to map the time history of the magnetic-field amplification, probing the various phases of turbulent dynamo: the kinematic phase, when fields are weak with respect to the turbulent motions; the nonlinear phase, when the Lorentz force back-reacts on the plasma's momentum; and the saturation phase, when the magnetic energy reaches a sizable fraction of the kinetic reservoir and amplification stops (Fig. 152.54). We designed the experimental platform using numerical simulations on one of the nation's leadership supercomputers (Fig. 152.55). The platform is uniquely suited to generating turbulent plasmas in the large magnetic Reynolds numbers regime, where the dynamo can operate. The configuration consists of two diametrically opposed foil targets that are backlit with temporally stacked beams, delivering 5 kJ of energy on each side in a 10-ns span. The beams drive a pair of counter-propagating plasma flows that carry seed magnetic fields generated by the Biermann battery effect. The flows propagate through a pair of grids that destabilize the flow and define the driving scale of the turbulence. The flows meet at the center of the chamber to form a hot, turbulent interaction region where the weak seed magnetic fields are amplified to saturation values.

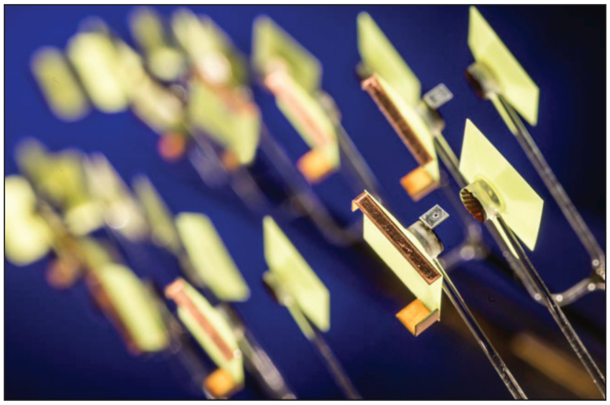

U2240JR

Figure 152.53
Experimental platform for the NLUF campaign to study turbulent dynamo amplification, a ubiquitous astrophysical process. The target assembly consists of two polystyrene foils and a pair of meshes, held together by a pair of cylindrical shields and a "tuning-fork" stalk. The foils and meshes were carefully designed to optimize the conditions in the interaction region for turbulent field amplification. The shields and flaps protect the interaction region, the imploding D^{3}He capsule, and the diagnostics from direct view of the laser spots.

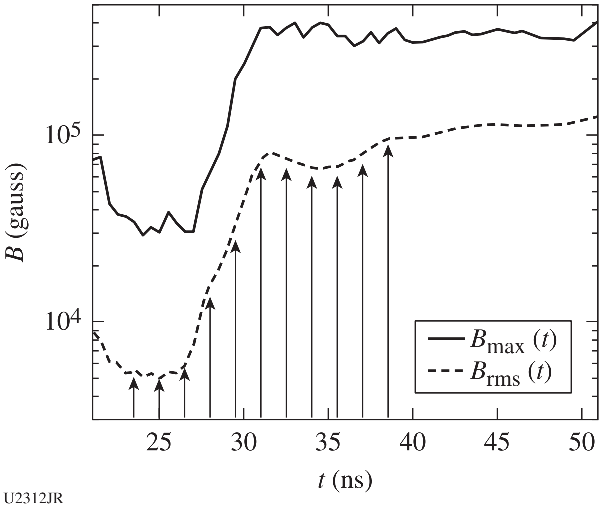

U2312JR

Figure 152.54
Simulated time history of the magnetic field's strength (in gauss) in the interaction region, showing the kinematic (exponential), nonlinear, and saturation phases of the dynamo for root mean square (rms) and peak values of the magnetic field. The arrows denote the different times at which we fired the proton radiography diagnostic: the 1.5-ns cadence allowed us to collect enough experimental data to temporally resolve the rise of the magnetic field.

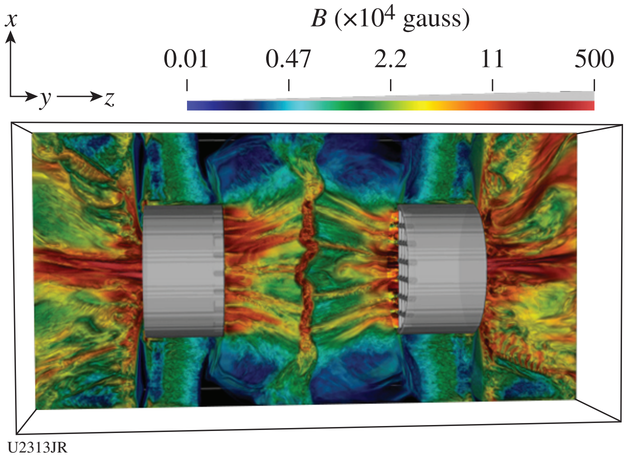

Figure 152.55
Three-dimensional radiation magnetohydrodynamic simulation of the experimental platform, performed with the multi-physics code *FLASH*. A large simulation campaign on Argonne National Lab's *Mira* BG/Q supercomputer guided us in the design of a platform capable of probing the turbulent dynamo regime. The figure displays a 3-D rendering of the magnetic field's magnitude (in gauss) after the jets collide.

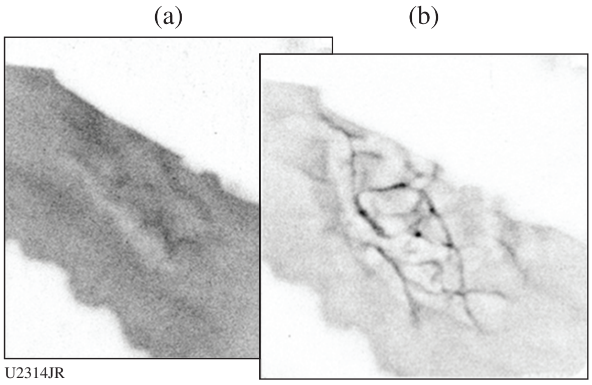

Figure 152.56
Proton radiographs (14.7 MeV) at $t = 25$ ns and $t = 29.5$ ns, corresponding to the times when the turbulent region first forms and weak seed fields are advected in (a) the center and (b) halfway through the exponential amplification phase when the filamentary structures start to develop. Analysis of the radiographs will reveal the topology and magnetic-field strength that the protons traversed on their way to the CR-39 film pack. The wealth of experimental diagnostics has enabled us to characterize the magnetized plasma, study the turbulent dynamo mechanism, and map its temporal evolution.

With a modest redesign of our original experimental platform, we were able to develop a faster and more-accurate alignment procedure; this enabled us to perform *15* shots during our first shot day—a record number given the complexity of our platform. The shots yielded a wealth of experimental data. The diagnostics we fielded allowed us to fully characterize the turbulent interaction region and quantify its plasma properties in space and time. More specifically, x-ray imaging enabled us to directly visualize the formation and evolution of the turbulent region. From the x-ray intensity fluctuations we reconstructed the density power spectrum of the magnetized turbulence and inferred its power law. Moreover, the spatially resolved spectrum from the Thomson-scattering diagnostic yielded clear ion-acoustic and electron features—at different times—that allowed us to characterize the plasma properties, including the ion and electron temperatures; the bulk flow and turbulent velocities; and the electron density in a 1.5-mm field of view. Therefore, we were able to probe for the first time both the turbulent interaction region *and* the inflowing plasma. Finally, to recover the time history of the magnetic-field amplification, we fielded the proton radiography diagnostic in all shots (Fig. 152.56). Utilizing the proton-radiography data and the novel magnetic-field mapping techniques we have developed, we are able to reconstruct the strength and topology of the magnetic field during *all* phases of dynamo amplification, with a 1.5-ns cadence (Fig. 154.54). This plenitude of experimental data is under analysis and promises to greatly expand our understanding of the puzzle that is astrophysical turbulence.

Creation of a Magnetized Jet Using a Hollow Ring of Laser Beams

Principal Investigator: E. Liang (Rice University)

Progress toward the objectives of this NLUF project as listed in the original application far exceeded expectations in its second year. We carried out a one-day joint OMEGA and OMEGA EP laser experiment in November 2016, using 20 OMEGA beams to form a hollow ring focal pattern to create a magnetized jet from a flat plastic target. Some of the targets were doped with 2% Fe. The hollow ring radius varied from 800 to 1200 μm. Twelve shots were successfully completed, half of which were joint shots with OMEGA EP. The Thomson-scattering (TS) diagnostic was used to measure the on-axis electron and ion density, temperature, and flow velocity at 2.5 mm from the laser target for each shot. The TS results confirmed the predictions of new *FLASH* 3-D simulations, after allowance was made for the TS probe beam's heating of the electrons. The on-axis densities, temperatures, and velocities are comparable for the 800- and 1200-μm-radius rings, suggesting that the optimal OMEGA ring radius lies between 800 and 1200 μm. In six of the shots, we used 3-MeV and 14-MeV monoenergetic protons from D^{3}He capsule implosions to measure the magnetic fields in the jet via proton radiography. For the other six shots we used continuum OMEGA EP protons to probe the magnetic fields. Both sets of proton radiography images gave consistent results, which compare favorably with 3-D *FLASH* simulation predictions of approximately megagauss axial fields for both the 800- and 1200-μm cases. This shows that the plasma properties of the hollow ring jet, including its collisionality and MHD properties, will be significantly impacted by the self-generated magnetic fields. We used an x-ray framing camera to take x-ray images of the jet at 1-ns time intervals. The images show well-collimated laminar outflows for both the 800- and 1200-μm cases. This is in excellent agreement with 3-D *FLASH* predictions. When we compare the x-ray images of the undoped and 2% Fe-doped jets, we find that the Fe-doped jet is narrower and the x-ray emission stronger, as predicted by *FLASH.* A poster on the 2016 results was presented at the Omega Laser Facility Users Group (OLUG) Workshop in April 2017. The Principal Investigator (PI) also gave invited talks on the NLUF results at the NNSA symposium in Chicago in April 2017 and at LANL in July 2017. Updated results on both the OMEGA data and *FLASH* simulations will be presented at the American Physical Society Division of Plasma Physics (APS DPP) meeting in Milwaukee in October 2017. A National Ignition Facility (NIF) Discovery Science proposal based on the OMEGA results and *FLASH* simulations was submitted to the NIF in September 2017.

Development of a Photoionized Plasma Experiment on OMEGA EP

Principal Investigator: R. C. Mancini (University of Nevada, Reno)

Experiments on basic high-energy-density science on OMEGA EP provide a unique opportunity to create states of matter at extreme conditions of temperature, density, and radiation flux relevant to astrophysics. The focus of this project is to study the fundamental atomic and radiation physics of plasmas driven by a broadband intense flux of x rays; i.e., photoionized plasmas. Most laboratory work performed to date on high-energy-density laboratory plasmas pertains to collisional plasmas; i.e., those where electron collisional processes play a dominant role in the plasma ionization and atomic kinetics. However, relatively little attention has been paid to studying and understanding the fundamental properties of laboratory photoionized plasmas, where both photoionization and photoexcitation driven by a broadband x-ray flux are dominant. These plasmas are important for understanding a myriad of astrophysical sources including x-ray binaries, active galactic nuclei, and the accreting disks formed in the vicinity of black holes. The information that we obtain on these objects is based on the analysis of spectroscopic measurements recorded by orbiting telescopes such as Chandra and XMM-Newton. Yet, the analysis of the spectra relies on sophisticated atomic and radiation physics models that have been developed only on a best-theory effort. Therefore, there is a critical need for performing systematic photoionized plasma laboratory experiments to benchmark theory and modeling codes.

We are developing a silicon photoionized plasma experiment on OMEGA EP in which a plastic-tamped silicon foam is ionized by the 30-ns-duration, broadband x-ray flux produced by the "gatling-gun" radiation source. This source is comprised of three copper hohlraums that are driven by three OMEGA EP beams, each delivering 4 kJ of UV energy in a 10-ns square pulse shape. The laser beams sequentially illuminate one hohlraum at a time, thereby producing an x-ray drive characteristic of 90-eV radiation temperature for a time period of 30 ns. The silicon sample is placed at a distance of 7 mm from the source. It has an initial mass density of 100 mg/cm^3 and a thickness of 0.1 mm and is coated with two 1-μm-thick layers of plastic. Heated by the x-ray flux, the silicon sample expands by a factor of 10 and ionizes into the L-shell range of silicon ions, thereby producing a photoionized plasma with an atom number density of a few times 10^{19} atoms/cm^3 and a relatively uniform spatial distribution.

In the first phase of the experiment's development, we performed OMEGA EP shots in which the expansion and ionization of the tamped silicon foam was monitored with a gated imaging x-ray spectrometer that recorded the L-shell self-emission of the plasma. The radiation temperature of the gatling source was measured with a VISAR diagnostic. The expansion to 1-mm thickness and ionization of the silicon sample were both confirmed by the observations during the experiment.

Figure 152.57 displays L-shell emission from line transitions in B- and Be-like silicon ions recorded at $t = 6$ ns and $t = 9$ ns. No measurable line emission in these ions is noted before $t =$ 6 ns. The x-ray flux starts at $t = -15$ ns and lasts until $t = +15$ ns. Therefore, these observations are taken during the second half of the x-ray drive duration. This is reasonably consistent with the pre-shot expectation based on radiation–hydrodynamics modeling of the experiment. This observation is now being used to refine the numerical simulation. The spectra demonstrate the formation of a highly ionized silicon plasma driven by the x-ray flux. It also provides data to extract the electron temperature.

The next step in the experiment's development is to perform x-ray K-shell transmission spectroscopy of the silicon photoionized plasma with a streaked instrument and a separate titanium backlighter driven by the fourth beam of OMEGA EP. The transmission spectroscopy will permit the extraction of the silicon charge-state distribution and an independent check on the temperature from the L-shell emission spectra analysis.

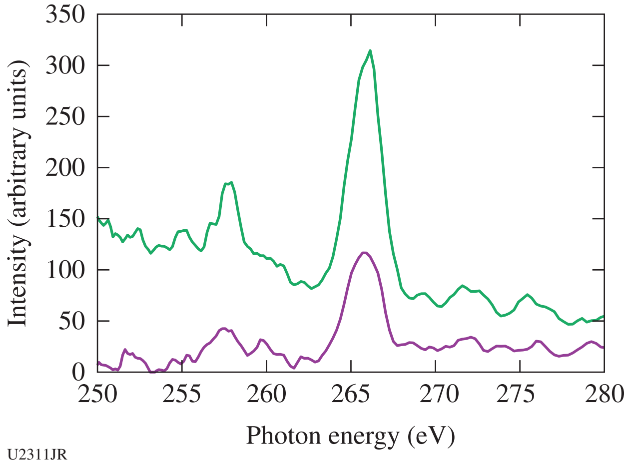

Figure 152.57
Photoionized silicon plasma L-shell self-emission recorded in OMEGA EP shot 26079 with a gated spectrometer at $t = 6$ ns (purple curve) and $t = 9$ ns (green curve). The emission spectral features at photon energies of 257 eV and 266 eV are caused by L-shell line transitions in B-like and Be-like silicon ions.

Explorations of Inertial Confinement Fusion, High-Energy-Density Physics, and Laboratory Astrophysics

Principal Investigators: R. D. Petrasso, C. K. Li, and J. A. Frenje (MIT)
Co-investigators: F. H. Séguin and M. Gatu Johnson (MIT)
Graduate students: N. Kabadi, B. Lahmann, H. Sio, R. Simpson, G. Sutcliffe, and C. Wink (MIT)
Undergraduate Student: M. Manzin (MIT)

MIT work in FY17 included a wide range of experiments applying proton radiography, charged-particle spectrometry, and neutron spectrometry methods developed by MIT and collaborators to the study of laboratory astrophysics, high-energy-density physics (HEDP), and ICF plasmas.[7–17] This was an outstanding year for the HEDP Division's scientists and students and their work on NLUF-related research. Based on NLUF work resulting in the development of the multiple-monoenergetic-particle source (MMPS) and its application to a wide range of physics experiments involving the observation and measurement of laboratory plasma phenomena and associated electromagnetic fields through radiography and other means, Drs. C. K. Li, R. D. Petrasso, and F. H. Séguin (Fig. 152.58) were chosen as recipients of the APS 2017 John Dawson Award for Excellence in Plasma Physics Research.* The MMPS is a laser-driven capsule containing D^3He fuel that produces monoenergetic charged-fusion products including 3.0-MeV protons, 14.7-MeV protons, and 3.6-MeV alpha particles during a 0.1-ns time interval, used either as a backlighter for multiple-monoenergetic-particle radiography or as a source of monoenergetic particles for other nonimaging experiments. The many subjects MIT has studied with the MMPS during the NLUF program include ICF experiments, plasma jet propagation, and magnetic reconnection, utilizing the MMPS as a backlighter for radiography, and quantitative studies of ion stopping and ion-electron equilibration in plasmas. These NLUF-developed techniques have also recently been ported to the NIF (LLNL).

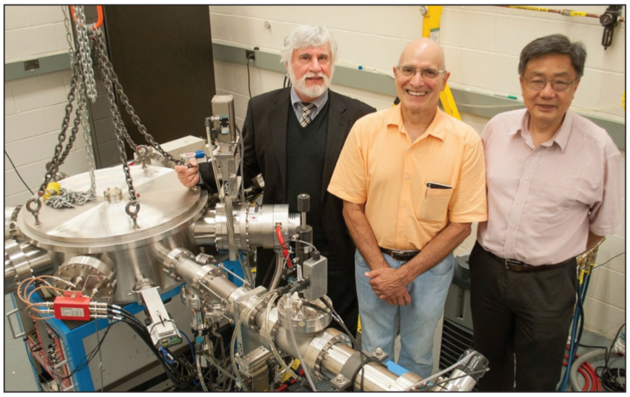

Figure 152.58
The three MIT scientists chosen as recipients of the American Physical Society's 2017 John Dawson Award for Excellence in Plasma Physics Research, standing next to the target chamber of the MIT-PSFC HEDP Division's accelerator facility (left to right: F. H. Séguin, R. D. Petrasso, and C. K. Li). The accelerator facility played a crucial role in the development and calibration of the multiple-monoenergetic-particle–source diagnostic platform used in the research cited in the Dawson Award.

The MMPS has been used by several MIT students in research critical to their outstanding Ph.D. theses. These include Drs. M. Manuel and M. Rosenberg, who received the APS *Rosenbluth Outstanding Doctoral Thesis Award* in 2014 and 2016, respectively, and Dr. A. Zylstra, who has now been nominated for the same award. In addition to the HEDP Division's own students, investigators from many other institutions have enlisted MIT's collaboration in their HEDP experiments on OMEGA to gain the unique information supplied by radiography with the MMPS. Those institutions include LANL, the University of Rochester, LLNL, the University of Chicago, Princeton University, UCSD, the University of Michigan, and the University of Oxford.

---

*The MIT scientists shared the Dawson Award with three scientists at other institutions (A. MacKinnon, Lawrence Livermore National Laboratory; M. Borghesi, The Queen's University, Belfast; and O. Willi, Heinrich Heine University, Düsseldorf). Those scientists had applied a different kind of proton source to radiography of plasmas, using TNSA, in which a laser pulse strikes a planar target and generates a strong electric field, charge separation, and a resultant picosecond-duration proton beam with a continuous energy spectrum.

In the meantime, other important NLUF accomplishments have included experimental measurements of nuclear reactions relevant to stellar and big-bang nucleosynthesis using high-energy-density plasmas on OMEGA and extensive experiments on kinetic physics. Many of these experiments have been enhanced by MIT student H. Sio's development of the new particle x-ray temporal diagnostic (PXTD) on OMEGA for simultaneous time-resolved measurements of several nuclear products as well as the x-ray continuum produced in HEDP. The PXTD system makes it possible, for the first time, to take accurate and simultaneous measurements of x-ray emission histories, nuclear reaction histories and their time differences along with measurements of $T_\mathrm{i}(t)$ and $T_\mathrm{e}(t)$ for studies of kinetic, multi-ion effects, and ion-electron equilibration rates in ICF plasmas.

Study of Magnetized Collisionless Shocks in Laser-Produced Plasmas

Principal Investigator: A. Spitkovsky (Princeton)
Co-investigator: C. M. Huntington (LLNL)

The FY17 MagShock EP Campaign was dedicated to the study of collisionless magnetized shocks in ablated plasma flows and exploration of new experimental concepts. Collisionless shocks commonly form in supernova remnants and in the heliosphere. The shock thickness is determined by the Larmor radius of the incoming protons, and the collisional mean free path must be much longer. The setup is shown in Fig. 152.59(a). The experiments used the OMEGA EP Laser System in which a 3-D–printed Helmholz coil powered by MIFEDS was inserted; two targets were mounted on MIFEDS. A 400- to 800-J, 1-ns pulse was used to ablate plasma that propagated along the coil's magnetic field (this component is called "background" plasma). A 1.3-kJ, 1-ns pulse was used to drive a fast-flow orthogonal to the magnetic field [this component is called "piston" plasma; see Fig. 152.59(b)]. The interaction between the flows was expected to drive a compression in the background plasma and the magnetic field [see Fig. 152.59(c)]. At a strong enough drive, this compression becomes a collisionless shock. This compression was diagnosed using proton radiography with TNSA from a short 1-ps laser pulse. The protons were recorded on CR-39 film, which was our primary diagnostic. On some shots, the 4ω optical probe was also utilized.

The experiments resulted in the detection of a magnetized collisionless shock propagating through the plasma. The main feature of the magnetic compression in the data was the appearance of a white band in the proton image, indicating additional deflection of the protons. The band was followed by a sharp caustic of enhanced proton concentration [Figs. 152.60(a)–152.60(c); shots separated by 2 ns]. The band and the caustic propagated at 300 km/s. The thickness of the band made it possible to constrain the magnetic compression ratio to 2.3, and the caustic was interpreted as the signature of the contact discontinuity between the piston and compressed background plasma [Fig. 152.60(d) lineout along the blue line in Fig. 152.60(b)]. This compression ratio corresponds to a Mach-3.4 shock. The shock is in the collisionless regime since the mean free path of the background protons is larger than the size of the plasma. These results were confirmed on several shots that performed the time-series study. Several time offsets were also tried before the piston plasma was launched, presumably probing different background densities. Extensive numerical simulations of the experiment were performed with 3-D PIC simulations [Figs. 152.59(c) and 152.59(d)], including simulated proton radiography through the fields of the simulation. The experimental results agree quite well with the predictions of the simulations. These findings will be presented at APS DPP Meeting in October 2017 as an oral contribution.

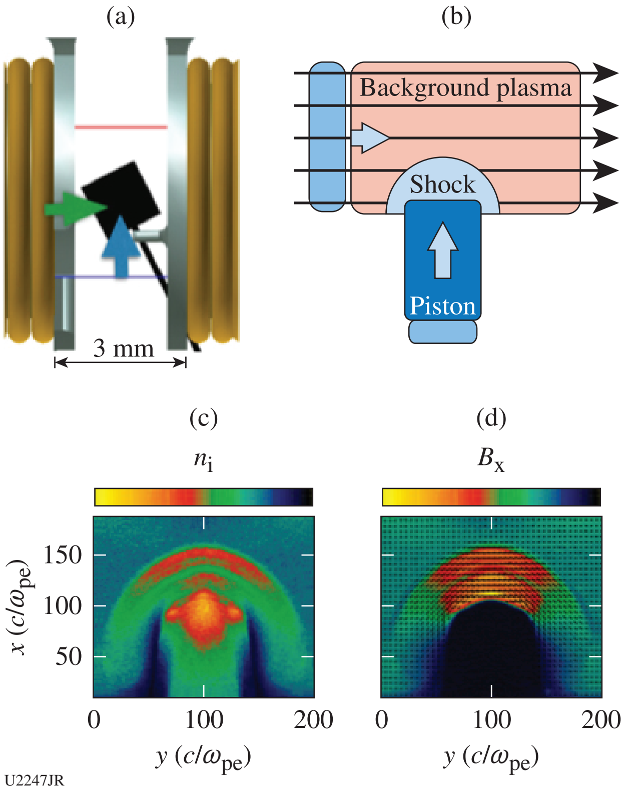

Figure 152.59
(a) Experimental setup for MagShock-EP-16AB, (b) schematic of fast-piston plasma interacting with a magnetized background plasma, and [(c),(d)] particle-in-cell (PIC) simulations of density and magnetic compression launched by a piston plasma.

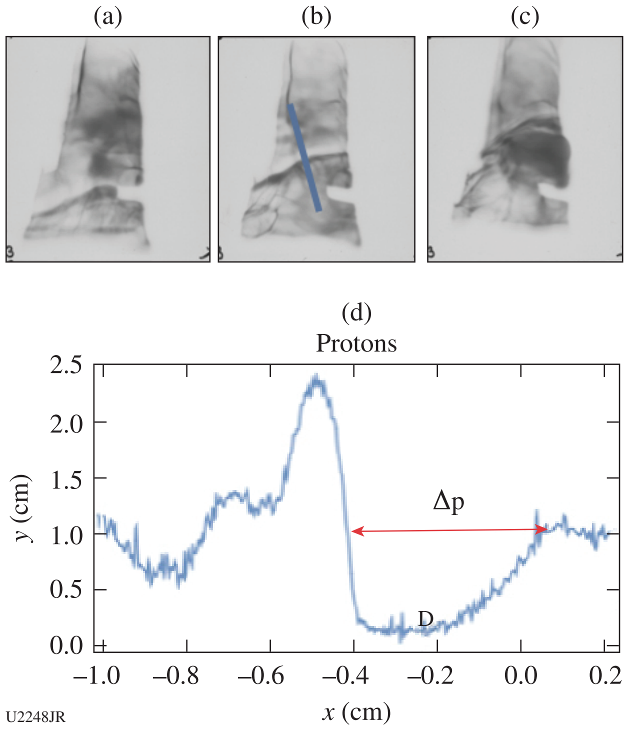

Figure 152.60
[(a)–(c)] Proton radiography of the interaction at different times. Notice the movement of the white band and the sharp caustic feature behind it. (d) Proton density in a cross-section cut, indicated by the blue line in Fig. 152.60(b).

In a second campaign in August, we attempted to probe the configuration through the orthogonal direction, resulting in rotation of the entire apparatus. The results are currently being analyzed. A clear shock signature was not seen, most likely because the background plasma density was lower than expected.

We thank the OMEGA EP personnel for their assistance in planning and executing this campaign.

Demonstration of Talbot–Lau X-Ray Deflectometry Electron Density Diagnostic in Laser–Target Interactions

Principal Investigator: D. Stutman (Johns Hopkins University)

An experiment aimed at demonstrating Talbot–Lau x-ray deflectometry (TXD) in high-energy-density plasmas was performed on the Multi-Terawatt (MTW) laser, where a laser-produced x-ray backlighter was used to illuminate a Talbot–Lau interferometer and obtain electron density maps of solid targets. These experiments confirmed that the TXD technique has the potential to become a basic and widespread diagnostic for HEDP experiments. To benchmark the technique in the HED environment, the interferometer must be tested in the presence of a plasma target. To this aim, a CH foil will be radiated by three UV OMEGA EP beams. A fourth beam will be used to obtain an x-ray backlighter source to illuminate the Talbot–Lau deflectometer, which will provide an electron density map of the ablated foil. Simulation and theory have failed to accurately predict the electron density profile from the ablation dynamics. TXD will provide electron density information in ranges not available today ($<n_c$) and will therefore advance the field of HED.

The proposed two-year research includes the implementation of a TXD on the OMEGA EP laser (FY18Q4). Preparatory experiments have been performed on MTW to test and optimize the x-ray backlighter. The first year has focused on diagnostic conceptual design and preparation of the experiment in collaboration with S. P. Regan and C. Stoeckl from LLE. The diagnostic design and implementation in the OMEGA EP laser are underway and being directed by C. Sorce and C. Mileham from the LLE Experimental Support Group. The conceptual design is shown in Fig. 152.61. Similar to the MTW setup, all the gratings will be mounted on a common optical base or rail. The common rail will allow us to accurately pre-align the gratings on site during pre-shot setup. The experiments will be defined and optimized in collaboration with P. A. Keiter (University of Michigan), so that the main goal of benchmark-

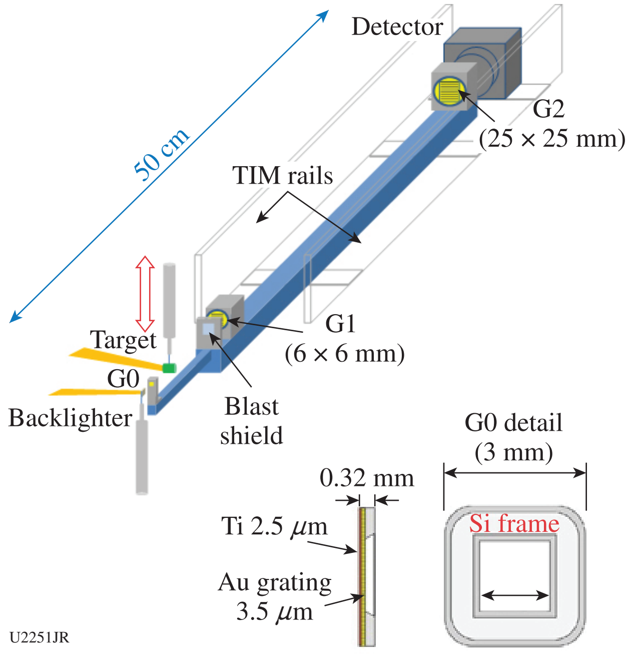

Figure 152.61
Conceptual design of the Talbot–Lau x-ray deflectometry (TXD) diagnostic for the OMEGA EP experiments. The inset shows source grating details. TIM: ten-inch manipulator

ing TXD as an electron density diagnostic for HEDP will be compatible with the goal of advancing the understanding of plasma ablation of plasma-irradiated foils.

Hot-Electron Generation with 10^{16}-W/cm^2 Infrared Lasers in the Shock-Ignition–Relevant Conditions

Principal Investigator: M. S. Wei (GA)
Co-investigators: C. M. Krauland (GA); S. Zhang, J. Li, and F. N. Beg (UCSD); C. Ren, W. Theobald, D. Turnbull, D. Haberberger, C. Stoeckl, R. Betti, and E. M. Campbell (LLE); and J. Trela and D. Batani (CELIA)

Shock ignition (SI) is an alternative ICF scheme that achieves ignition with a strong convergent shock launched by a high-intensity (~10^{16}-W/cm^2) laser spike at the end of the low-intensity (~10^{14}-W/cm^2) assembly pulse. SI spike-pulse energy coupling to the fusion target is uncertain because of laser–plasma instability (LPI) such as filamentation, stimulated Brillouin scattering (SBS), stimulated Raman scattering (SRS), two-plasmon decay (TPD), and the resultant hot-electron generation. Therefore, it is important to characterize the LPI and the hot-electron beam energy, temperature, and divergence in SI-relevant conditions to further assess the SI scheme.

This GA-led NLUF HotEScaleEP-17A Campaign conducted on OMEGA EP in August 2017 is an extension of our previous experiments (HotEScaleEP-15A), where we successfully demonstrated the propagation of an infrared (IR) laser beam (1.053 μm, 100 ps, up to 2.5 kJ, ~10^{16} W/cm^2) over a long-scale plasma (1.4-keV, 450-μm scale length) and the generation of a hot-electron beam with small divergence and moderate energies (T_{hot} ~ 90 keV). This year we continued using the IR laser with two beams (up to 2.3 kJ) in the co-propagating (co-prop) geometry to extend the pulse duration to 200 ps. The IR pulse (i.e., 200 ps with the co-prop beams or 100-ps single beam) had a nominal vacuum laser intensity of ~2×10^{16} W/cm^2 at the quarter- or tenth-critical density (n_{c}) surface. We used three-layer (25 μm CH/20 μm Cu/50 μm Al) solid disk targets designed to stop hot electrons up to 200 keV. A hot, large-scale CH plasma was created by a 2-ns, 2.2-kJ UV laser (B3 or B4) with 750-μm distributed phase plates (DPP's) ($I \sim 2 \times 10^{14}$ W/cm^2) to mimic the large corona plasma in SI. At 1.5 ns after the start of the UV pulse, the single or co-prop IR beams were injected. A suite of optical (the 10-ps 4ω probe and the newly available OMEGA EP SABS) and x-ray diagnostics [e.g., SCI, ZVH, bremsstrahlung MeV x-ray spectrometer (BMXS), and hard x-ray detector (HXRD)] were utilized to characterize LPI and the hot-electron energy, spectral, and angular distribution.

In our HotEScaleEP-17A experiments, we found that hot-electron generation by the co-prop IR beams (200 ps) was sensitive to the plasma temperature as shown in Fig. 152.62. Such dependence was not observed in the single IR beam (100-ps) interaction. With the higher-temperature (1.5-keV) plasma, the Cu K$_\alpha$ photon yield produced by the co-prop IR beams increased 170% compared to the data with 1.0-keV plasma. Meanwhile, the measured hard x-ray signal was also increased about 130% to 180% in the 17- to 200-keV energy range. HXRD data suggested a hot-electron temperature of less than 100 keV. The AFR image obtained from the 4ω probe diagnostic showed that the co-prop IR beams propagated beyond the $n_{\text{c}}/4$ in high-temperature plasma and produced a bright self-emission spot at the n_{c} surface as shown in Fig. 152.63. Resonance absorption may have contributed to hot-electron generation at the n_{c} surface. The bright self-emission spot was not observed from the interaction of either the co-prop IR beam with the 1.0-keV plasma or the single IR beam (100 ps) with the same density scale plasma with a temperature from 1.0 to 1.4 keV. The AFR image also captured the density perturbation between $n_{\text{c}}/10$ and $n_{\text{c}}/4$ surface as the result of strong nonlinear LPI's. OMEGA EP SABS recorded spectrally resolved sidescattering of the IR beam in the 400- to 750-nm spectrum range showing SRS. The 4ω self-emission observed at the n_{c} surface indicated that SRS and TPD were saturated since the co-prop IR beams propagated beyond the $n_{\text{c}}/4$ surface (TPD and SRS boundary). The data analysis and PIC modeling are ongoing.

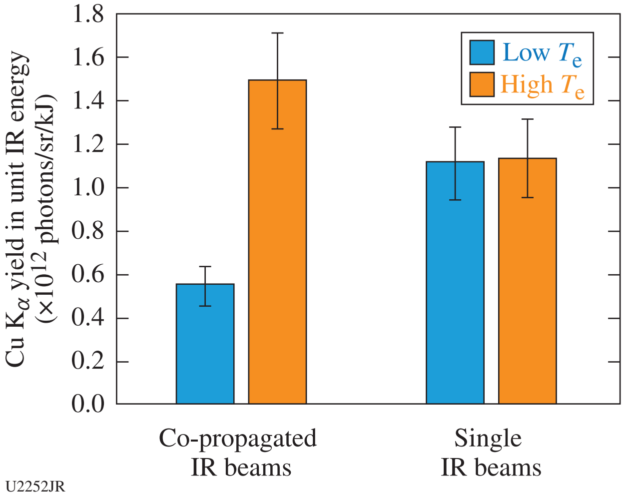

Figure 152.62
The Cu K$_\alpha$ yield (normalized to the IR beam energy) from the interaction of the single and two co-prop IR beams with low- (1.0-keV) and high- (1.4- to 1.5-keV) temperature plasmas was measured using a zinc von Hamos x-ray spectrometer.

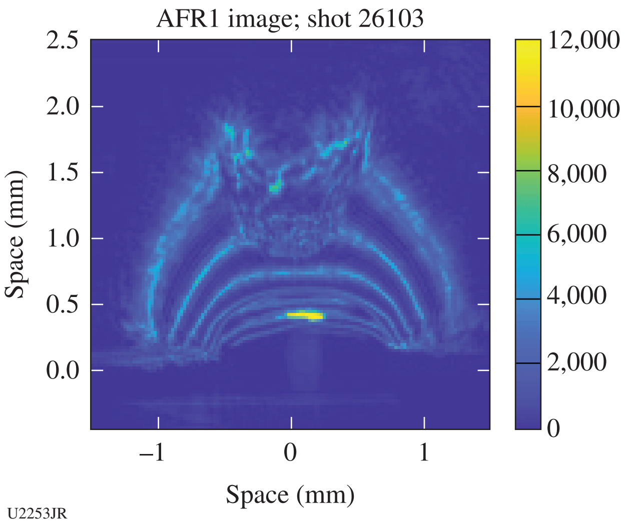

Figure 152.63
The 4ω probe–measured AFR image of the co-prop IR beams in the high-temperature (1.5-keV) plasmas The co-prop IR beams strongly interacted with the long-scale plasma and reached the critical-density surface, producing bright self-emission.

FY17 Laboratory Basic Science (LBS) Program

Sixteen LBS projects previously approved for FY17 target shots were allotted Omega Laser Facility shot time and conducted a total of 199 target shots at the Omega Laser Facility in FY17 (see Table 152.VIII). The FY17 LBS experiments are summarized in this section.

During FY17, LLE issued a solicitation for LBS proposals to be conducted in FY18. A total of 28 proposals were submitted. An independent committee reviewed and ranked the proposals; on the basis of these scores, 16 proposals have been allocated 21 shot days at the Omega Laser Facility in FY18. Table 152.IX lists the approved FY18 LBS proposals.

Exploring Pair Plasmas and Their Applications

Principal Investigator: H. Chen (LLNL)

In FY17, an LLNL/SLAC/University of Michigan team continued this project on OMEGA EP with one LBS shot day. These experiments use the short-pulse beams to produce jets of electron–positron antimatter pairs. The FY17 campaign focused

Table 152.VIII: LBS experiments approved for target shots at the Omega Laser Facility in FY17.

Principal Investigator	Institution	Title
H. Chen	LLNL	Exploring Pair Plasmas and Their Applications
A. R. Christopherson	LLE	Shock-Ignition Timing Measurements on OMEGA
J. R. Davies	LLE	Measuring the Nerst Effect and the Thermal Dynamo
S. Jiang	LLNL	Characterizing Pressure Ionization in Ramp-Compressed Materials with Electron-Induced Fluorescence
E. V. Marley	LLNL	Time-Resolved Measurement of the Radiative Properties of Open L-Shell Zinc
D. A. Martinez	LLNL	Optimizing Backlighters for Imaging Low-Density Plasmas for Eagle Pillar Studies
M. A. Millot	LLNL	Equation of State, Structure, and Optical Properties of Silicates at Multi-Mbar Pressure for Super-Earth Mantle and Accretion Modeling
A. Pak	LLNL	Laser-Driven Collisionless Shock Acceleration of Ions (E-Shock)
H.-S. Park	LLNL	Astrophysical Collisionless Shock Experiments with Lasers
H. G. Rinderknecht	LLNL	Measuring Strong Plasma Shock-Front Structure Using Thomson-Scattering Imaging
M. J. Rosenberg	LLE	Electron Energization During Magnetic Reconnection in High-Energy-Density Plasmas
A. M. Saunders	LLNL	Absolute Equation-of-State Measurements from Spherical Converging Shock Waves on the OMEGA Laser
R. F. Smith	LLNL	Determining the High-Pressure Properties of Silicon Carbide Using Decaying Shocks in *In-Situ* X-Ray Diffraction
R. F. Smith	LLNL	Experimentally Constraining the High-Pressure Thermal Conductivity of Iron
C. E. Wehrenberg	LLNL	Recovery of Dynamically Compressed Samples
A. B. Zylstra	LANL	Charged-Particle Stopping Power and Scattering Measurements in a Warm Dense Plasma

on measuring the pair yield enhancement with nanostructured targets. The experiments successfully demonstrated that the laser-positron energy conversion can be improved by using novel structured targets. A total of 12 shots were performed.

The OMEGA EP short-pulse beams (~1 kJ in 10 ps) irradiated 1-mm-thick Au targets with and without the nanostructure on the laser-interaction surface. It was found that for the same laser energy, positron yields and acceleration both were increased dramatically by using a nanostructure. This finding is important to future experiments and applications using laser pair jets. Previous experiments used primarily gold targets and showed that quasi-monoenergetic relativistic positron jets are formed during high-intensity irradiation of thick gold targets,[18,19] and also that these jets can be strongly collimated[20] using the magneto-inertial fusion electrical discharge system (MIFEDS).[21] The external field produces a 40-fold increase in the peak positron and electron signal.[20] The positron yield was found to scale as the square of the laser energy[22,23] in this regime. The yield also increases with the Z of the target material. Together with the nanostructured target yield enhancement, these favorable scalings are expected to enable the laboratory study of relativistic pair plasmas to aid one's understanding of some of the most exotic and energetic systems in the universe.[23,24]

Shock-Ignition Timing Measurements on OMEGA

Principal Investigators: A. R. Christopherson, D. T. Michel, R. Betti, A. K. Davis, S. Depierreux, W. Seka, C. Stoeckl, and W. Theobald (LLE); and J. Trelou, A. Casner, M. Lafon, C. Neuville, and X. Ribeyre (CEA)

The objective of the Shock-Ignition Timing Campaign was to measure the ablation pressure and hot-electron preheat from the ignitor spike. Small [650-μm-outer-diam (OD)] CH shells were irradiated with two pulse shapes—one with a spike and one without a spike—as shown in Fig. 152.64(a). The compression of the shell resulting from the ignitor shock was measured by the x-ray framing camera (XRFC). This is illustrated in Fig. 152.64, where (a) represents the ablation-front trajectories of the implosions with and without a spike, while (b) is an image from the XRFC showing how the ablation front and hot-

Table 152.IX: LBS experiments approved for target shots at the Omega Facility in FY18.

Principal Investigators	Institution	Title
S. J. Ali	LLNL	Effect of Grain Size on the Dynamic Failure of Diamond
H. Chen	LLNL	Exploring the Applications of Laser-Produced Relativistic Electron–Positron Pair-Plasma Jets
T. Doeppner	LLNL	Equation-of-State Measurements of Shock-Heated Foams Using X-Ray Thomson Scattering and Fluorescence
S. Jiang	LLNL	Characterizing Pressure Ionization in Ramp-Compressed Materials with Electron-Induced Fluorescence
G. Kagan	LANL	Separation of Ion Species in Collisional Plasma Shocks
A. Krygier	LLNL	Shock Metamorphism and Lattice Deformation Kinetics in Meteor Impacts
T. Ma	LLNL	Proton Isochoric Heating for Warm-Dense-Matter Studies
E. V. Marley	LLNL	Radiative Properties of an Open L-Shell, Non-LTE Plasma
P. M. Nilson	LLE	Applying Marshak Waves to the Iron Opacity Problem
H.-S. Park	LLNL	Study of High Alfvénic Mach Number Plasma Dynamics and Magnetized Shocks
D. N. Polsin	LLE	Structure and Melting of High-Pressure Sodium
M. J. Rosenberg	LLE	Electron Energization During Magnetic Reconnection in High-Energy-Density Plasmas
J. R. Rygg	LLE	Atomic and Electronic Structure of Warm Dense Silicon
R. F. Smith	LLNL	Thermal Conductivity of Fe and Fe-Si at Earth Core Conditions
W. Theobald	LLE	Shock Formation and Hot-Electron Preheating in Planar Geometry at Shock-Ignition–Relevant Laser Intensities
A. B. Zylstra	LANL	Charged-Particle Stopping Power Near the Bragg Peak

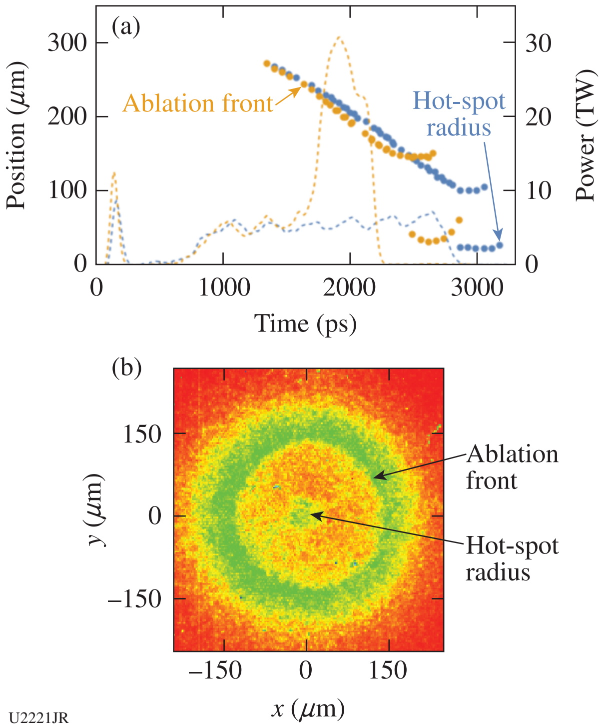

Figure 152.64
(a) The ablation-front trajectories for the implosion with (dotted orange curve) and without (dashed blue curve) the spike, which clearly accelerates faster after the shock has been launched. The dashed lines represent the laser power in TW. (b) An x-ray framing-camera image that is used to determine the ablation-front position and the hot-spot radius.

spot radius are measured. A maximum ignitor shock ablation pressure of ~180 Mbar was inferred from a post-shot *LILAC* simulation approximately constrained to the data.

One way to experimentally determine preheat by hot electrons is to measure the premature expansion of the shell before the ignitor shock breaks out. This preheat causes the hot spot to emit earlier than it would without preheat. In Fig. 152.64(a), the implosion with the ignitor shock starts emitting earlier than the no-spike case. Understanding the relative importance of hot-electron preheat versus ignitor shock breakout time on the earlier emission is the subject of an ongoing investigation.

Measuring the Nerst Effect and the Thermal Dynamo

Principal Investigator: J. R. Davies (LLE)

The objective of this experiment was to observe the dynamo effect caused by cross-field heat flow. The dynamo effect occurs because of sheared rotation of plasma around magnetic-field lines, which acts to twist the field lines, generating a component in the direction of the rotation. The dynamo effect has been extensively studied in the context of astrophysical jets.

A magnetic field in a plasma moves not only with the bulk plasma motion but also with the electron heat flow, which can be ascribed to the field being preferentially frozen to the electrons responsible for heat flow because of their lower collision frequency. In magnetized plasma there exists heat flow perpendicular to the temperature gradient and the magnetic field, known as cross-field heat flow. Cross-field advection of the field has largely been ignored, but it could readily lead to a dynamo effect in the absence of plasma rotation.

To generate a thermal dynamo, we placed a carbon disk inside a MIFEDS coil, giving an axial magnetic field, and irradiated the edge of the disk with ten OMEGA beams, five from each side, creating a radial temperature gradient, which will lead to an azimuthal cross-field heat flow and the generation of an azimuthal magnetic field. To probe the magnetic field, we used D^{3}He protons passing through a grid on one side of the target.

Unfortunately, MIFEDS started to trigger erratically and only one magnetized shot was obtained, at maximum field, which deflected all of the protons out of the detection angle, as shown in Fig. 152.65. The grid is not visible, which may be a result of being attached to the target or simply being too close to the target or backlighter. Although this one shot indicates that the thermal dynamo effect does occur, shots with lower magnification, a lower magnetic field, and a working grid setup would be required to confirm and quantify the effect.

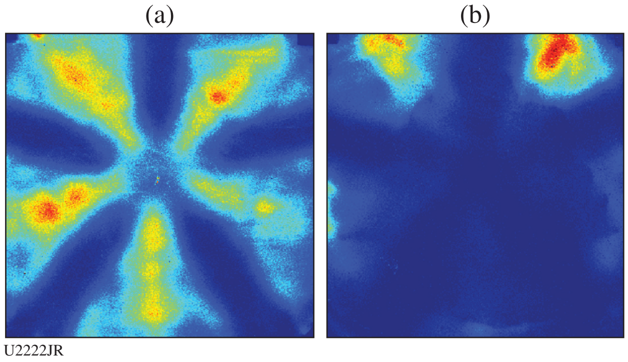

Figure 152.65
Proton radiographs of (a) unmagnetized and (b) magnetized disks irradiated at the edges by five OMEGA beams on each side. The empty regions (blue) in the unmagnetized case correspond to the beam paths. In the magnetized target, almost all of the protons have been deflected away from the detector.

Characterizing Pressure Ionization in Ramp-Compressed Materials with Electron-Induced Fluorescence

Principal Investigator: S. Jiang (LLNL)
Co-investigators: Y. Ping, R. F. Smith, A. Jenei, and J. H. Eggert (LLNL)

This campaign used one day on OMEGA EP to measure ionization in compressed materials as a function of density, using K-shell fluorescence spectroscopy. The K-shell line emissions were induced by hot electrons generated through short-pulse laser–solid interactions. The high pressure was achieved by ramp compression using the long-pulse drivers while keeping the temperature low. A large, thick target was used to avoid heating from the short pulse, as shown in Fig. 152.66(a). The configuration is intended to compress the material up to 1.5× to 2× its original density without raising the thermal ionization effect. There is still little consensus on pressure ionization under these conditions despite extensive theoretical and experimental efforts.

A schematic of the experimental setup is displayed in Fig. 152.66(a). The main diagnostic used in this campaign was the high-resolution imaging x-ray Thomson spectrometer (IXTS). The Cu K_α and Co K_β fluorescence lines were successfully observed with a high signal-to-noise ratio, as can be seen in Fig. 152.66(b). Under the designed experimental conditions, pressure ionization has a negligible effect on the innermost electron shells (K,L), but it can affect the M shell. Therefore, the Cu K_α line is not subject to an energy change and can be used as a reference. On the other hand, the Co K_β line is more prone to a shift. Figure 152.66(b) shows the measured Co K_β peaks under different driver energies and time delays. While some differences can be observed between the undriven and driven conditions, the energy shifts are small enough that they are close to the resolution of the spectrometer (~4 eV). In a future experiment, we will increase the driver energy to reach a higher pressure and also probe other materials.

Time-Resolved Measurement of the Radiative Properties of Open L-Shell Zinc

Principal Investigator: E. V. Marley (LLNL)
Co-investigators: L. C. Jarrott, M. B. Schneider, G. E. Kemp, M. E. Foord, R. F. Heeter, D. A. Liedahl, K. Widmann, C. W. Mauche, G. V. Brown, and J. A. Emig (LLNL)

This campaign was designed to measure the emitted L-shell zinc spectrum from a well-characterized and uniform plasma for comparison to atomic kinetic models. Recent studies have shown a discrepancy between atomic kinetic models and high-*Z* M-shell spectral data. This study was done to test the accuracy of models for L-shell emission.

Planar buried layer targets were illuminated evenly on both sides (Fig. 152.67) to heat the sample composed of Ti and Zn. The sample was buried between two 6.7-μm-thick layers of Be, which inertially tamps the sample, slowing its expansion.

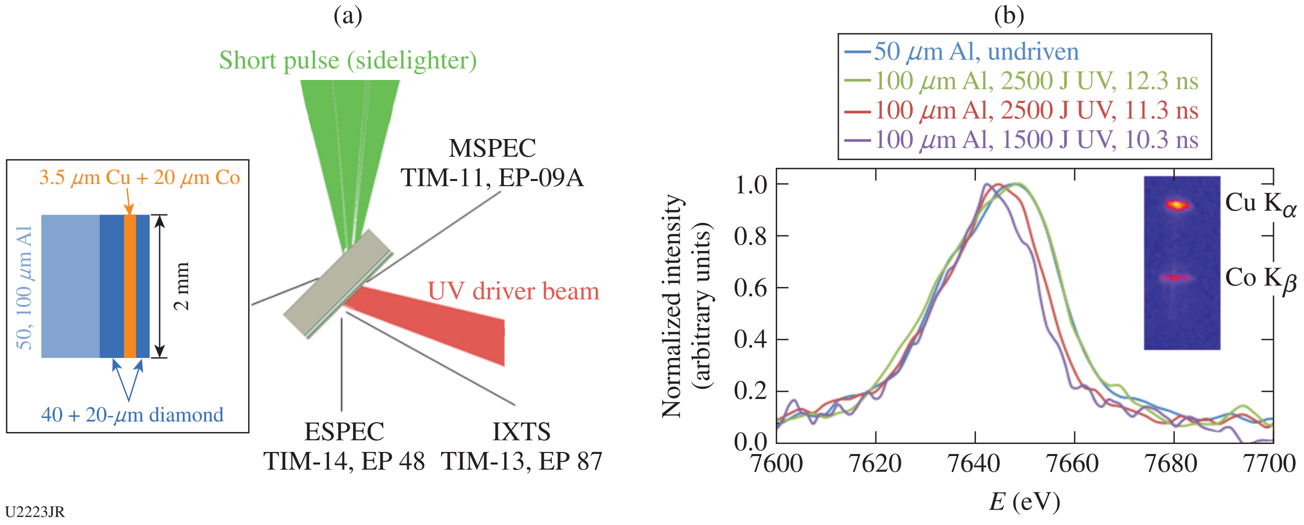

Figure 152.66
(a) A schematic of the experimental configuration. The inset shows the target geometry. (b) Measured IXTS spectra of Co K_β (normalized with the peak intensity). The lineouts are from different driver conditions. An example of the raw image is shown in the inset in (b).

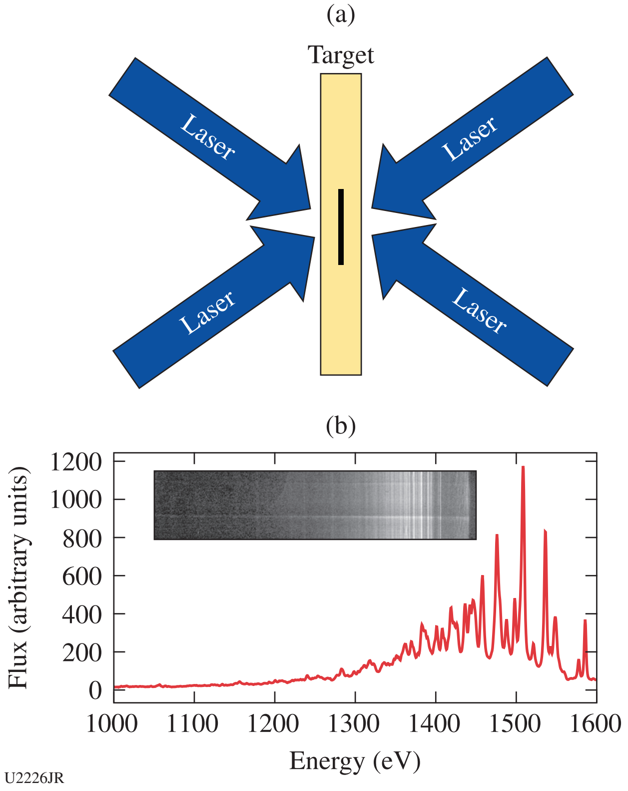

Figure 152.67
(a) Experimental configuration; (b) time-resolved Zn L-shell spectrum with data inset at 2.8 ns of shot 85317.

Time-resolved 2-D images of the target's x-ray emission, viewed both face-on and side-on, were recorded using pinhole cameras coupled to framing cameras. The K-shell spectrum from the Ti was used to determine the electron temperature of the plasma. The time-resolved spectrum was recorded using a crystal spectrometer coupled to a framing camera. A second crystal spectrometer/framing-camera system was used to record time-resolved zinc L-shell emission. More L-shell spectra were recorded with a spectrometer coupled to a streak camera to give a continuous record of the ion population shifts over time. A third spectrometer, which utilized a variably spaced grating and a slit, was coupled to a framing camera to give a temporally and spatially resolved spectral measurement of the zinc L shell. This measurement will help to verify the uniformity of the plasma at different times during the experiment. All of the framing cameras, used for imaging as well as for spectroscopy, were co-timed on the shot day so that plasma conditions could be determined for the measured zinc L-shell spectra.

Two different pulse shapes were used: a 3.2-ns square pulse and a 3.0-ns square pulse with a 100-ps picket preceding it by 1 ns. The second pulse tested whether creating a pre-plasma before the main pulse would create a smoother interface, allowing for a more-efficient coupling of energy into the target. The results look promising. A complete set of data from all six co-timed diagnostics was recorded for both pulse shapes during the campaign at sample temperatures ~1 keV.

Optimizing Backlighters for Imaging Low-Density Plasmas for Eagle Pillar Studies

Principal Investigator: D. A. Martinez (LLNL)
Co-investigators: J. Kane and R. F. Heeter (LLNL); and B. Villette and A. Casner (CEA)

The LBS Eagle Pillar experiments were designed to optimize the backlighter for imaging the plasma plume created by an ablated CH solid-density cone target in conditions similar to counterpart NIF Discovery science experiments. The CH target was driven for 30 ns using three Cu hohlraums (Fig. 152.68) heated in succession, which will eventually create

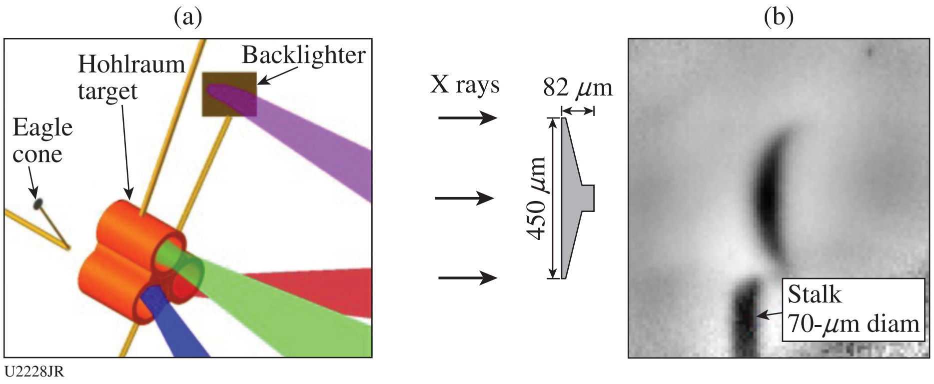

Figure 152.68
(a) Layout of the experiment showing all beams on target. (b) A hohlraum drives a cone target for 30 ns and is imaged with a Ti (shown) or U backlighter.

a comet-like flow behind the solid target (away from the drive). This flow is expected to coalesce behind the solid target, and the hohlraum x-ray drive will confine the plasma to generate a plasma pillar. To observe this requires a backlighter with sufficiently low photon energy to image the warm, low-density plasma. This campaign used Ti (4.7-keV) and U (1.2-keV) area backlighters to try to image the ablating CH target. Seven shots were taken with a backlighter delay between 20 and 35 ns with respect to the start of the drive, using both U and Ti backlighters. Because of debris risk, the experiment used image plates with a 200-μm Be blast shield, increasing the average photon energy for the U backlighter to the 3- to 4-keV range. Images obtained from the U backlighter were comparable to the Ti backlighter, both suggesting this photon energy was too high. The U backlighter also showed significant structure in the backlighter profile as shown in Fig. 152.69. More work is needed to sufficiently reduce the photon energy to image the ablated plasma.

Equation of State, Structure, and Optical Properties of Silicates at Multi-Mbar Pressures for Super-Earth Mantle and Accretion Modeling

Principal Investigator: M. A. Millot (LLNL)

Co-investigators: F. Coppari, D. E. Fratanduono, and S. Hamel (LLNL); N. Dubrovinskaia and L. Dubrovinsky (Bayreuth University, Germany); and R. Jeanloz (University of California, Berkeley)

During FY17, our international research team conducted two campaigns at the Omega Laser Facility to investigate the equation of state, structure, and optical properties of silicates at multi-Mbar pressures using shock compression.

Following our previous study on the melting line of SiO_2 using stishovite crystals,[25] we conducted a shock compression study of $MgSiO_3$ bridgmanite (perovskite) samples synthesized at Bayreuth University, Germany, to investigate the pressure–density–temperature equation of state and the melting temperature of $MgSiO_3$, representative of the material making up the interiors of rocky planets and the cores of gas giants. Preliminary analysis of the velocity interferometry (VISAR) and streaked optical pyrometry (SOP) data indicates that we successfully observed reflecting shocks up to 15 Mbar.

Another set of experiments used OMEGA EP pulse-shaping capabilities to launch a carefully timed series of two steady shocks into stishovite samples to make it possible to determine the atomic structure of SiO_2 at Neptune core conditions using x-ray diffraction. Composite three-beam pulse shapes enabled us to generate the complex drive conditions, while focusing Beam 1 on a Ge foil was used to generate a 1-ns pulsed x-ray source. Preliminary analysis indicates that x-ray diffraction (XRD) patterns (Fig. 152.70) for single- and double-shock compressed silica were obtained up to 9 Mbar.

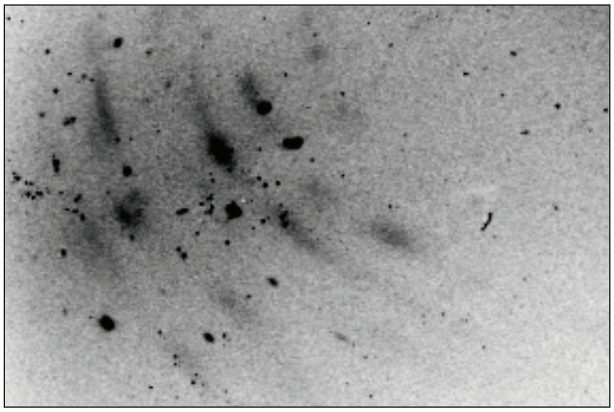

Figure 152.70
Example of an x-ray–diffraction pattern of silica shock compressed to ~3 Mbar along the stishovite Hugoniot.

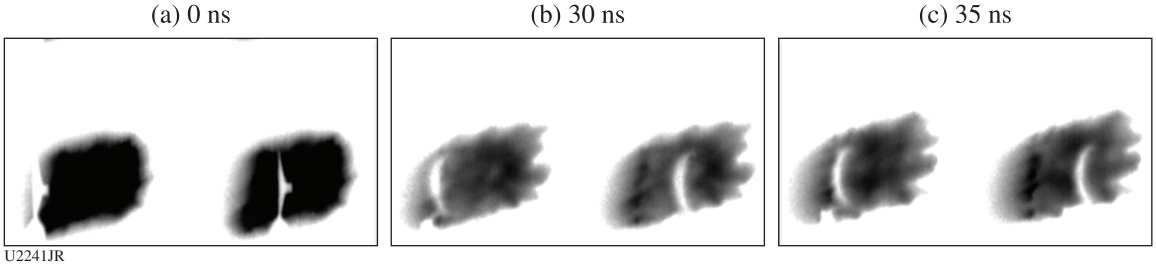

Figure 152.69
Time sequence of the target imaged through a pinhole array backlit with a U backlighter. Multiple images were obtained to remove the backlighter structure. The (a) 0-ns image had lower filtering but the (b) 30- and (c) 35-ns images had 200 μm Be.

Laser-Driven Collisionless Shock Acceleration of Ions (E-Shock)

Principal Investigator: A. Pak (LLNL)
Co-investigators: A. J. Link (LLNL); D. Haberberger and D. H. Froula (LLE); S. Tochitsky, C. Joshi, and F. Fiuza (University of California, Los Angeles)

This LBS shot day explored the acceleration of ions into narrow energy distributions caused by the reflection from the strong electrostatic field of a collisionless shock wave. As Fig. 152.71(a) indicates, a near-critical-density CH target was first produced by the x-ray drive generated from the ablation of a gold foil by a 1-ns-long laser pulse (UV Beamline 3). After waiting for the CH target to expand to a peak density of ~10×10^{21} cm^{-3}, the ultra-intense backlighter beam was used to irradiate the target and drive the collisionless shock wave. Nearly simultaneously, the sidelighter beam produced a beam of protons through target normal sheath acceleration (TNSA) to radiograph the shock-formation process.

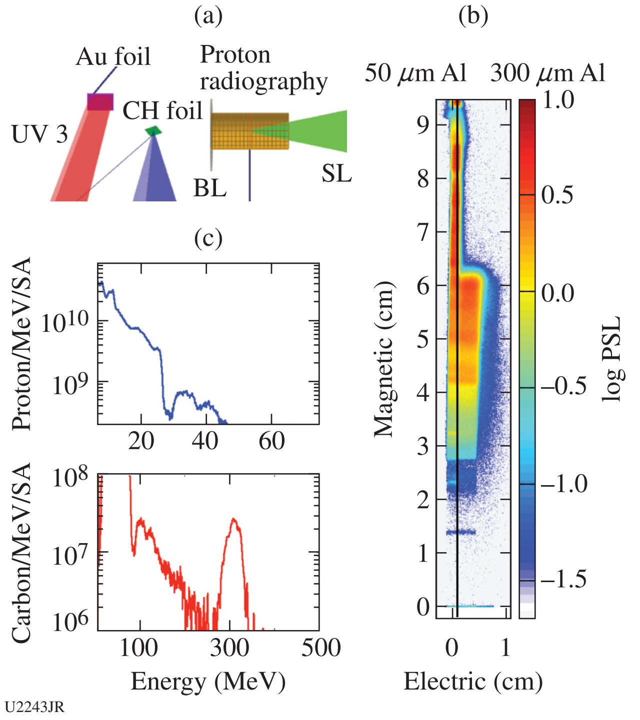

Figure 152.71
(a) Experimental configuration. (b) Data from the modified Thomson parabola ion energy (TPIE) setup with differential filtering and no electrical bias. The vertical black line denotes filter change. (c) The proton and carbon spectra. BL: backlighter; SL: sidelighter; PSL: photostimulated luminescence.

In these experiments, the pinhole of the Thomson parabola ion energy (TPIE) diagnostic was replaced with a new ~5-mm-wide × 0.25-mm-long slit to extend the angular acceptance of the diagnostic. The electric bias of the TPIE was turned off, and differential filtering of 50 μm and 300 μm Al was used at the image-plate detector to differentiate between ion species. TPIE data from this configuration are shown in Fig. 152.71(b).

In this experiment, narrow energy distributions of both protons and carbon ions were observed to be accelerated to similar velocities of ~0.25 c. The acceleration of disparate charge to mass ratio ion species to similar velocities is consistent with acceleration from the moving near-relativistic electric field associated with a collisionless shock wave. A distribution of protons centered at 36 MeV (velocity = 0.28 c), and with an energy range $\Delta E/E$ of ~30% was observed, as well as a distribution of C^{6+} ions centered at 308 MeV (velocity = 0.23 c) and $\Delta E/E$ of ~12%. The difference in velocity between the two ion species is thought to arise from the remaining sheath field of the expanded target, which preferentially accelerates the lighter species. Analysis of the radiography and accelerated beam profile data is in progress.

Astrophysical Collisionless Shock Experiments with Lasers

Principal Investigator: H.-S. Park (LLNL)
Shot Principal Investigator: G. F. Swadling (LLNL)

Experiments ACSEL-17A and 17B investigated the physical processes that lead to the formation of astrophysical collisionless shocks. These shots continued a broad, long-running, cross-institutional collaboration. A total of 26 target shots were completed in two shot days, primarily investigating interactions between beryllium ablation outflows; this material was selected to provide a low-*Z*, single-species plasma, which greatly simplifies Thomson-scattering interpretation and analysis, while maintaining the large collisional scale lengths required to observe the development of interpenetrating flow instabilities. In these experiments, the OMEGA beams heat the surfaces of a pair of opposed planar disk targets (see Fig. 152.72), ablating counter-propagating plumes of high-velocity (up to 1.5×10^{6} ms^{-1}), high-temperature (~keV) plasma. The outflow parameters are such that the coulomb mean-free path for interflow collisions is long, but the interaction of the flows is still susceptible to the growth of the interstream instabilities that are believed to mediate the formation of collisionless shocks.

This year, experiments focused on taking spatially resolved Thomson-scattering measurements across the interaction

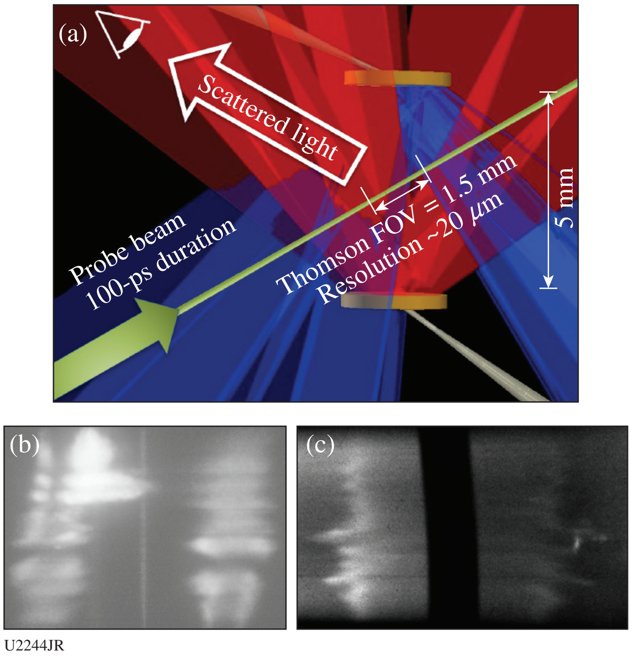

Figure 152.72
(a) Diagram of experimental setup for spatially resolved Thomson-scattering measurements. (b) Ion-acoustic wave (IAW) and (c) electron plasma wave (EPW) data. The vertical direction in the spectrograms is the direction of spatial displacement along the probe beam, as shown in the diagram. The horizontal direction is the direction of spectral dispersion. Striations in the vertical direction in the IAW image are characteristic of Weibel filamentation. Modulations in the EPW image indicate strong transverse modulations in the electron density across the interaction region. FOV: field of view.

region to quantitatively investigate the development of the ion-Weibel instability. Thomson scattering was combined with proton radiography measurements; a D^{3}He exploding-pusher capsule provided a dichromatic (3.3- and 14.4-MeV) proton source for radiography, probing the plasma at two separate times during each experiment. Images were recorded on CR-39, with processing and analysis of the CR-39 plates carried out by collaborators at MIT.

The OMEGA Thomson-scattering diagnostic records both ion-acoustic and electron plasma wave features of the Thomson-scattering spectrum. Analysis of the detailed shape of these spectra made it possible to extract information about the spatial variation in electron temperature, electron density, ion temperature, and flow velocity across the interaction of the two flows. The primary goal in FY17 was to make a direct measurements of spatial density modulations of the ion flows and the underlying electron density of the plasma. High-quality data were recorded and are expected to provide a wealth of data on the development of the ion-Weibel instability in these experiments; examples of the spectrograms are shown in Fig. 152.72. Striations in the intensity of the ion-acoustic feature along the probe beam are characteristic of the development of the ion-Weibel instability, while the presence of modulations in the electron plasma wave data suggests that the ion-Weibel instability is in the nonlinear growth phase.

Measuring Strong Plasma Shock-Front Structure Using Thomson-Scattering Imaging

Principal Investigator: H. G. Rinderknecht (LLNL)
Co-investigators: H.-S. Park and J. S. Ross (LLNL);
and D. H. Froula (LLE)

This series of shots was designed to directly measure for the first time the spatial structure of a strong shock front in a plasma. The experiments were intended to develop a platform for kinetic plasma studies using the new gas-jet system on OMEGA to quantify collisional phenomena in high-energy-density plasmas and to benchmark high-fidelity physics codes. These experiments were also the first use of the gas-jet system on OMEGA.

The KineticShockLBS-17A Campaign on 24 August used the new gas-jet system to inject a column of hydrogen or neon gas into the OMEGA target chamber. A 1-μm Si$_3$N$_4$ foil positioned near the gas-jet nozzle was driven by ten beams with 2.5 kJ in 0.6 ns, exploding the foil to drive a strong shock into the low-density (~5×10^{18} cm^{-3}) gas. A 526.5-nm probe beam with 40 J in a 100-ps impulse was injected normal to the ablator foil at a 4- to 6-ns delay from the drive beams, and Thomson-scattered light from the probe was imaged along the probe axis. The imaged region was 3.25 to 4.75 mm from the ablator, with a resolution of 20 μm. Despite operational difficulties with the gas-jet system on its first shot day, six shots were completed and excellent data collected on all shots for which the gas-jet successfully operated.

Figure 152.73 shows ion-acoustic wave (IAW) and electron plasma wave (EPW) Thomson-scattering images from shot 86801. Fits to the EPW data demonstrate the characteristics of strong shock formation: heating of electrons in the pre-shock region, followed by an increase in density as the ion shock forms. IAW data appear to show streaming protons in advance of the shock front, heating, and slowing down on the pre-shocked plasma; analysis of these results is underway. These exciting results will be presented in an invited talk at the APS DPP meeting in October 2017 to demonstrate the high value of this platform for future kinetic plasma studies on OMEGA.

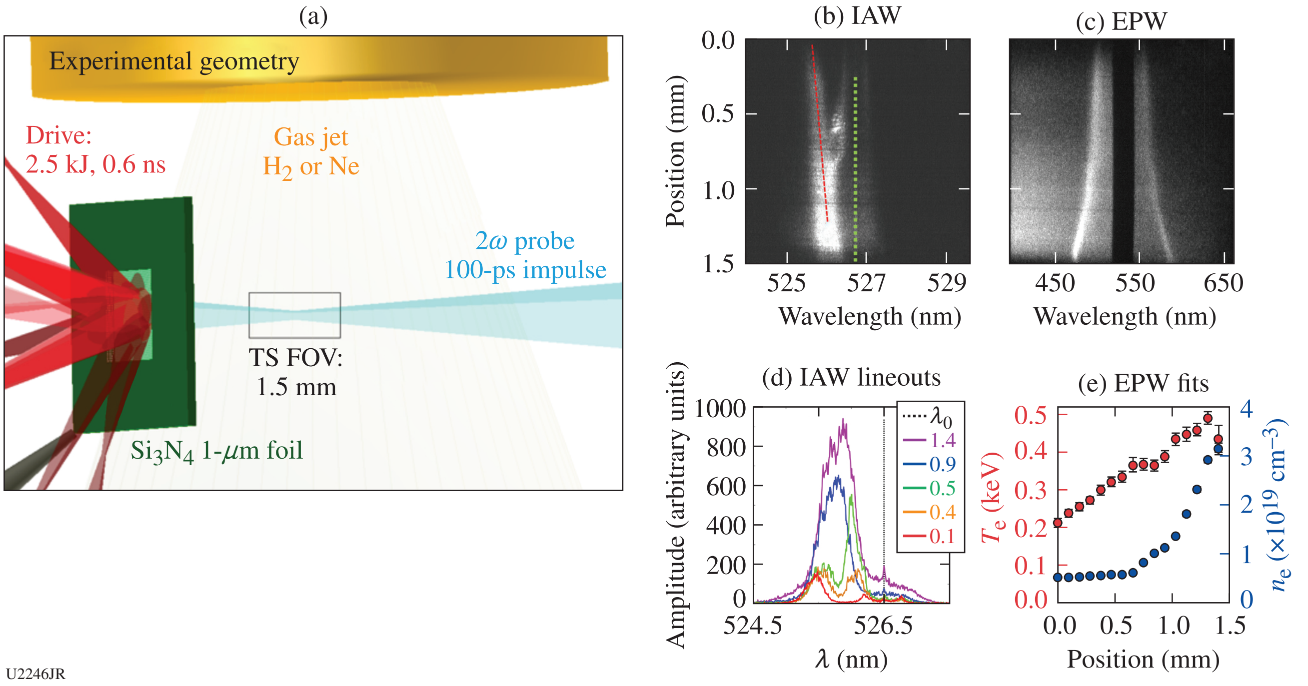

Figure 152.73
(a) Experimental layout; [(b),(c)] raw Thomson-scattering (TS) images; (d) lineouts from ion-acoustic wave (IAW) data showing merging of ion populations in shock; and (e) fits to electron plasma wave (EPW) spectrum showing heating and density jump resulting from shock in shot 86801. FOV: field of view.

Electron Energization During Magnetic Reconnection in High-Energy-Density Plasmas

Principal Investigator: M. J. Rosenberg (LLE)

The MagReconnection-17A shot day on OMEGA (14 March 2017) through the LBS program successfully diagnosed the spectrum of energetic electrons generated in laser-plasma experiments in which magnetic reconnection was driven. These experiments utilized a well-established platform for studying the generation, interaction, and reconnection of magnetic fields in plasmas created by the interaction of multiple laser-produced plasma plumes adjacent to each other using foil targets. The energization of particles during the annihilation of magnetic fields is a common process in astrophysical plasmas, but it is poorly understood and has rarely been investigated in the laboratory. The new, compact single-channel electron spectrometer microscope (SC-ESM) obtained electron spectra over the energy range of ~50 to 300 keV.

Spectra obtained perpendicular to the foil and parallel to the reconnection current sheet that supports the magnetic fields are shown in Fig. 152.74. Experiments with two beam spots [Figs. 152.74(b) and 152.74(c)] drove magnetic reconnection, while experiments with only one beam spot [Fig. 152.74(d)] did not. Energetic electron spectra were measured, with characteristic temperatures of ~30 to 50 keV. Notably, a single-beam experiment [Fig. 152.74(d)] generated energetic electrons, suggesting that additional mechanisms beyond magnetic reconnection, such as laser–plasma instability (LPI), may be producing the energized particles. In addition, Thomson-scattering measurements were successfully obtained to diagnose plasma conditions in the reconnection region, and monoenergetic proton radiography was used to confirm the interaction and reconnection of magnetic fields, as have been observed in previous experiments. Another LBS shot day has been awarded to this campaign, during which we will attempt to determine the source of energetic electrons and obtain spectra unambiguously from magnetic reconnection by eliminating LPI.

Absolute Equation-of-State Measurements from Spherically Converging Shock Waves on the OMEGA Laser

Principal Investigator: A. M. Saunders (LLNL)

Co-investigators: T. Doeppner and R. Nora (LLNL); W. Theobald (LLE); and A. Jenei, D. Swift, J. Nilsen, and R. W. Falcone (Lawrence Berkeley National Laboratory, University of California, Berkeley)

X-ray Thomson scattering (XRTS) is an experimental technique that directly probes the physics of warm dense mat-

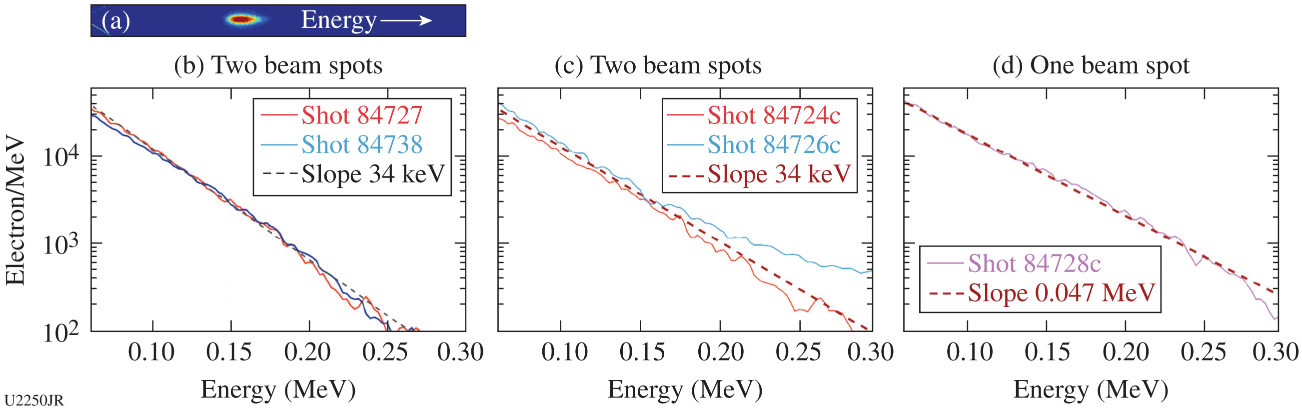

Figure 152.74
(a) A sample raw image-plate scan from SC-ESM; [(b)–(d)] spectra from various laser drive conditions.

ter by measuring electron density, electron temperature, and ionization state. XRTS in combination with x-ray radiography offers a unique ability to measure the absolute equation of state (EOS) of material in extreme conditions.

The OMEGA GbarIPD-17A Campaign took XRTS and x-ray radiography measurements from directly driven carbon-containing spheres compressed to electron densities of the order of 1×10^{24} cm^{-3} and temperatures of ~30 eV. X-ray radiography measurements were obtained for both plastic (CH) and high-density carbon (HDC) spheres. Fifty-two beams compressed the spheres, and six beams drove a foil backlighter. The x rays from the foil backlighter were observed in transmission through the sphere using a gated x-ray framing camera (Fig. 152.75). They show that the shock front travels inward as predicted by simulations. The radial lineouts make it possible to obtain the shock velocity. A more-complicated analysis of post-shock density at each time step will also be performed; the combination of density and shock velocity will allow for an absolute measurement of the EOS.

In conjunction with the radiography measurements, XRTS spectra were obtained from HDC spheres. A zinc He$_\alpha$ x-ray source was used to scatter x rays from the imploding spheres at a scattering angle of 135°. The scattered x rays were collected by a crystal spectrometer in conjunction with a gated x-ray framing camera. Figure 152.76 shows an example of the raw data collected and a lineout of one of the strips. The

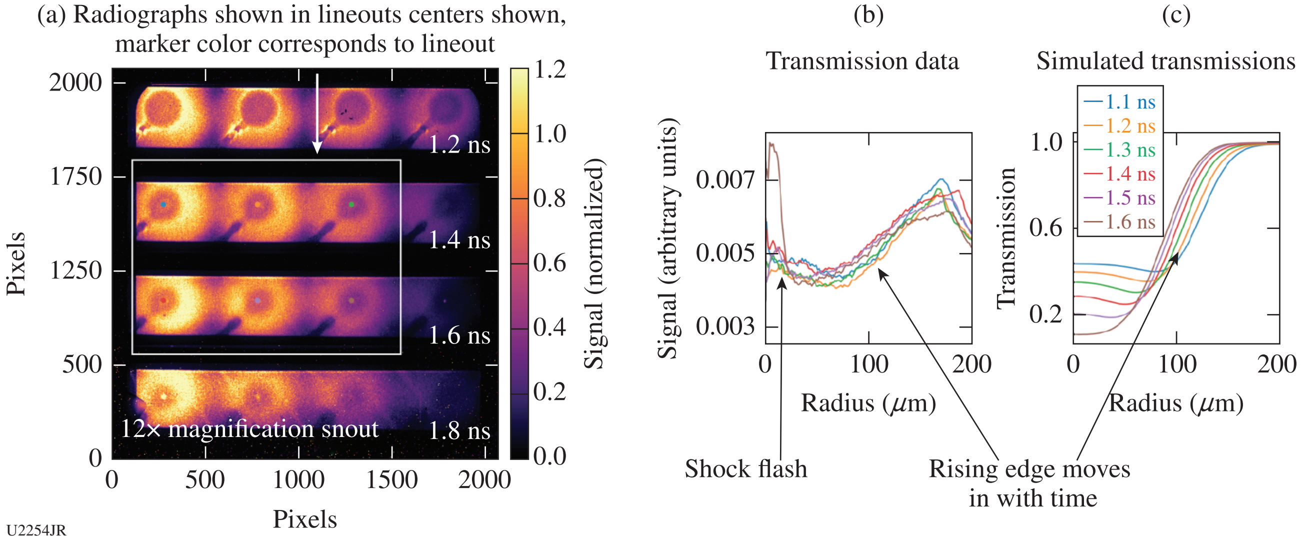

Figure 152.75
X-ray radiography measurements of shock-compressed CH spheres (shot 85691). (a) Example of the raw data obtained from the imploding CH spheres and [(b),(c)] radial lineouts from several of the radiography images, each at a different point in the implosion time.

XRTS data will provide an independent measurement of the mass-averaged electron temperature of the imploding sphere. The temperature measurement will further constrain the EOS measurement obtained from the radiography analysis. In summary, the data obtained in this campaign shed light on the EOS of matter under compression and support EOS measurements previously taken on the NIF.

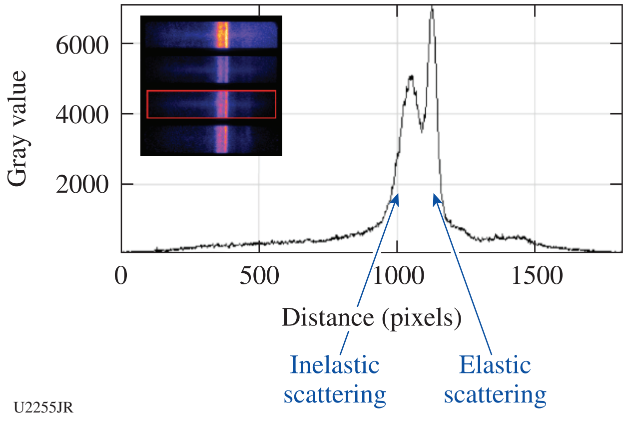

Figure 152.76
X-ray Thomson-scattering measurements from high-density carbon spheres (shot 85696).

Determining the High-Pressure Properties of Silicon Carbide Using Decaying Shocks in In-Situ *X-Ray Diffraction*

Principal Investigators: R. F. Smith (LLNL) and J. K. Wicks (Johns Hopkins University)

The goal of this campaign was to determine the high-pressure properties of single-crystal SiC along the Hugoniot, using a combination of shock decay[25] and nanosecond x-ray diffraction techniques.[26] Silicon carbide is an important material in geology and planetary science. It may be a host of reduced carbon in the Earth's interior since it is found in rocks from the mantle and in inclusions in deep diamonds.[27] It also occurs in meteorites and impact sites. The target design in Fig. 152.77 is modeled off previous campaigns on OMEGA.[25] The raw active shock breakout (ASBO) (shock velocity) and streaked optical pyrometer (SOP) (shock front thermal emission) data make it possible to determine the pressure–temperature onset of melt (see Fig. 152.78). During this shot day the powder x-ray

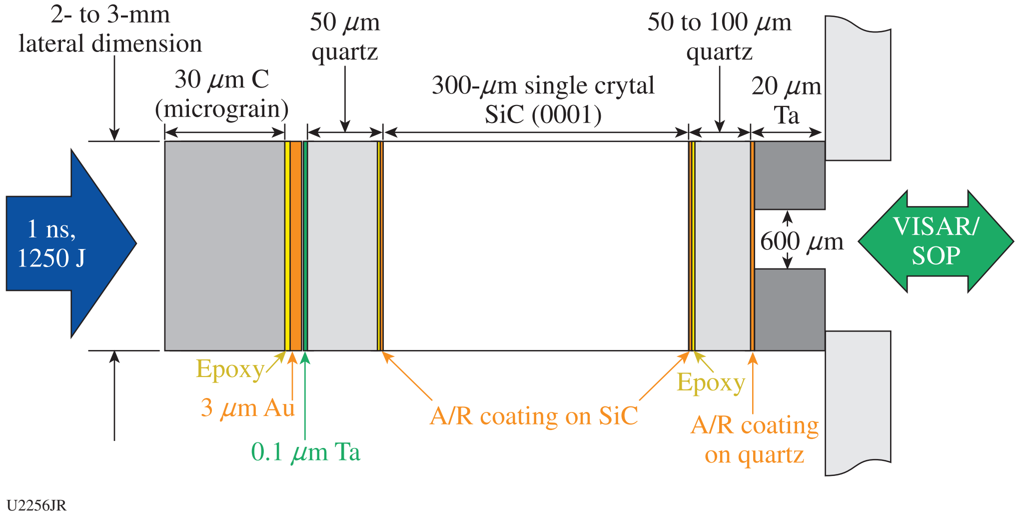

Figure 152.77
Target design for shock-decay experiments in SiC using a 1250-J drive in 1 ns (1100-μm phase plate). The quartz layers serve as calibrants for the OMEGA EP SOP.[25]

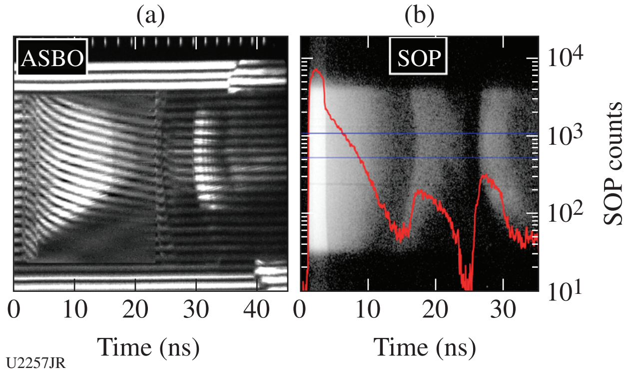

Figure 152.78
(a) Active shock breakout (ASBO) data provided the SiC shock velocity versus time. (b) The OMEGA EP SOP provided the temperature of the shock front as a function of time.

diffraction image-plate (PXRDIP) diagnostic was also used to determine the high-pressure crystal structure (pre-melt).

Experimentally Constraining the High-Pressure Thermal Conductivity of Iron

Principal Investigator: R. F. Smith (LLNL)
Co-investigator: J. K. Wicks (Johns Hopkins University)

High-pressure thermal conductivity is one of the most important and yet most difficult to measure physical property of materials. Within the Earth's interior the thermal conductivity k of Fe and Fe-rich alloys at core pressure–temperature conditions (135 to 360 GPa, 2500 to 5000 K, respectively) is a key parameter for heat transport models and plays an important role in determining the temperature profile and energy balance of our planet. The thermal conductivity of the Earth's core remains poorly constrained because of the extreme difficulty in making thermal transport measurements under the relevant pressure and temperature conditions. Two experimental studies published in Nature in 2016 report values of k for Fe that vary by a factor of 7 at ~130 GPa (34 → 225 W/mK) (Refs. 28 and 29). The goal of the OMEGA experiments was to constrain the thermal conductivity at high pressures, using a ramp-compression platform previously developed on OMEGA[30] (Fig. 152.79), where (1) stagnating plasma simultaneously launches a ramp-compression and heat wave in the sample, (2) a "cool" ramp-compression wave runs ahead of the heat wave (the sample pressure can be constrained using VISAR), and (3) LLE's SOP makes it possible to measure the heat-wave transit time. The raw ASBO/SOP data provide velocity and thermal transport information through stepped Fe samples (Fig. 152.80). Analysis is underway to translate this data into a measurement of thermal conductivity.

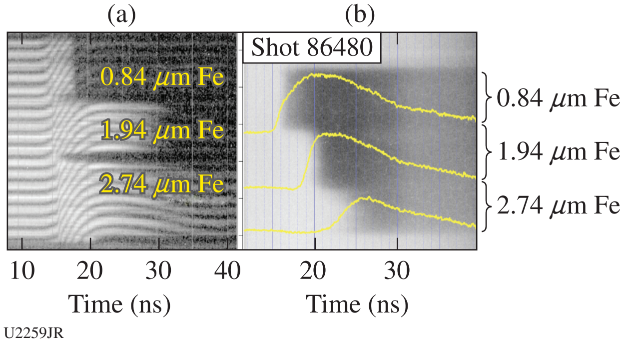

Figure 152.80
(a) ASBO and (b) SOP data for 0.84-/1.94-/2.74-μm Fe step samples provide sufficient information to constrain the high-pressure thermal conductivity of Fe.

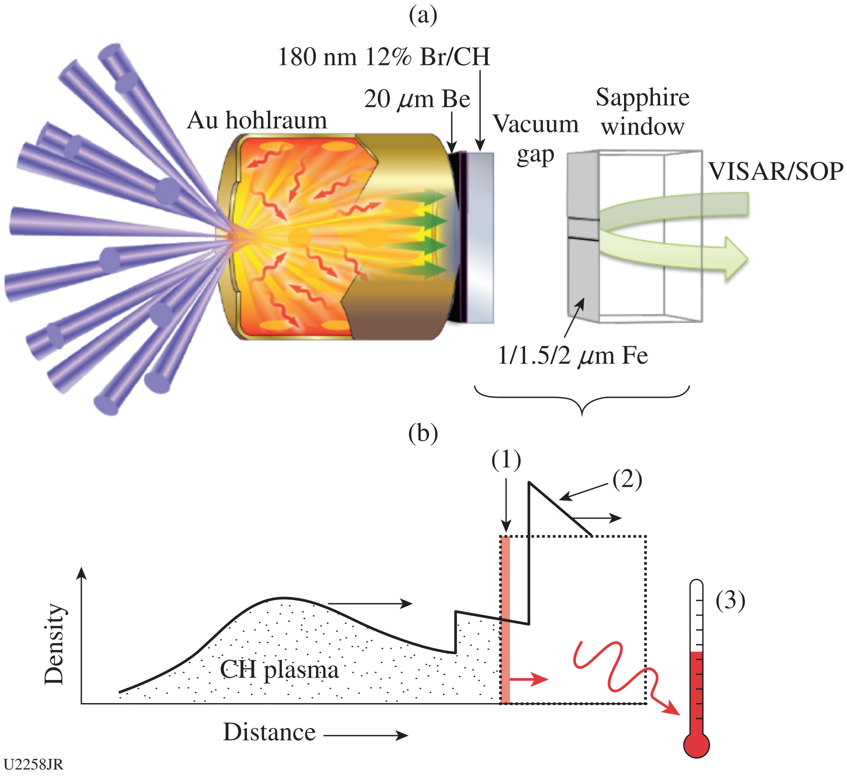

Figure 152.79
(a) Target design used to (b) measure heat flow in a ramp-compression stepped Fe sample.

Recovery of Dynamically Compressed Samples

Principal Investigator: C. E. Wehrenberg (LLNL)
Co-investigators: S. Zhao and M. Meyers (UCSD);
and B. Remington and A. Krygier (LLNL)

This LBS campaign studied the deformation response of a variety of materials to shock compression. Sample materials were mounted onto the front of steel recovery tubes that were in turn mounted on a ten-inch manipulator (TIM). A single OMEGA beam is used to drive a shock into the sample material, and the sample remains in the recovery tube after the shot so that it can be recovered for further *ex-situ* study. Two recovery tubes and a VISAR target were fielded for each shot. Consequently, a large data set of 12 recovered samples and six VISAR traces was produced using only a half-day of shots.

A wide variety of samples were recovered during this campaign. Previous iterations of this campaign have been very successful in studying the deformation response of semiconductors (Si and Ge) to shock compression, producing a series of high-profile papers on pressure-shear–induced amorphization.[31,32] The FY17 campaign studied GaAs, graphite, and olivine and generated the first dynamic compression data on a new class of materials—high-entropy alloys. These samples will be taken to Oak Ridge National Laboratory for TEM (transmission electron microscopy) study.

Charged-Particle Stopping Power and Scattering Measurements in a Warm Dense Plasma

Principal Investigator: A. B. Zylstra (LANL)

The d*E*d*x* Campaign is developing a platform to perform high-precision measurements of charged-particle stopping power (d*E*/d*x*). Stopping power in dense plasmas is important for ICF self-heating and propagating burn, particularly for particles near and below the peak in d*E*/d*x* ("Bragg peak"). While the stopping power has been measured in hot-spot–relevant plasmas using an exploding pusher platform, the current data cannot distinguish between models of interest;[33] for example, the Maynard–Deutsch and Brown–Preston–Singleton theories. This campaign uses shocked-foam targets probed by a separate source of fusion particles to achieve higher precision. The d*E*d*x*-17A shot day demonstrated the viability of this platform, shown in Fig. 152.81. Good data using 3-MeV protons from the D–D fusion reaction were acquired, shown in Fig. 152.81(b). A similar downshift is observed in both shocked (warm) and undriven (cold) foam, which is expected from stopping theory. Future experiments will be modified to use the lower-velocity particles, particularly D^{3}He$_\alpha$, which are more sensitive to d*E*/d*x* and will be able to differentiate between stopping models in this regime.

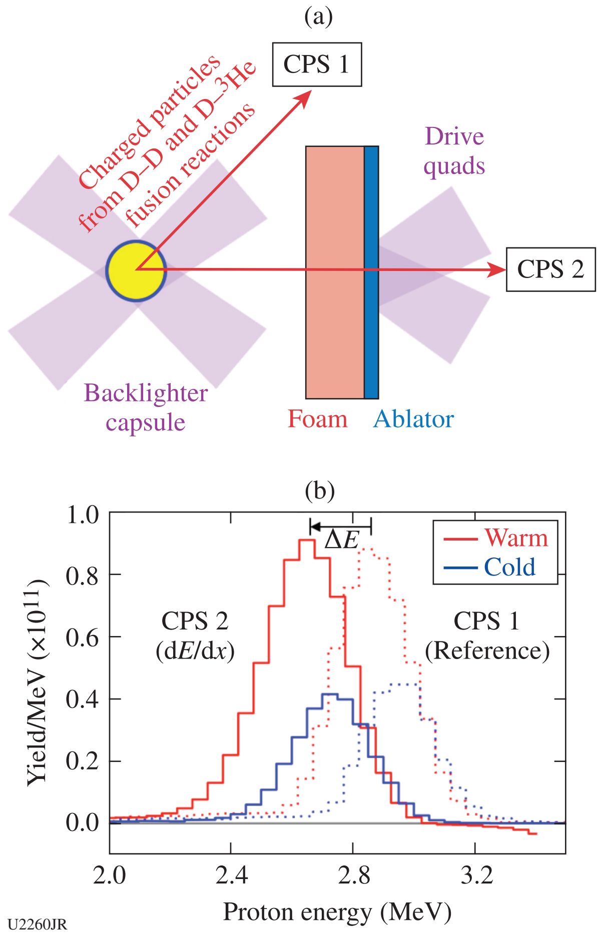

Figure 152.81
(a) Diagram of the experimental geometry. A backlighter capsule produces particles from the D–D and D–^{3}He fusion reactions, which probe a planar shock-compressed foam. (b) Example data of protons from the D–D fusion reaction slowing through warm and cold foams.

FY17 LLNL Omega Facility Experimental Programs

Principal Investigators: R. F. Heeter, F. Albert, S. J. Ali, H. Chen, F. Coppari, T. Doeppner, A. Fernandez Panella, D. E. Fratanduono, E. Gumbrell, C. M. Huntington, L. C. Jarrott, S. Jiang, A. Krygier, A. E. Lazicki, S. LePape, E. V. Marley, D. A. Martinez, J. M. McNaney, M. A. Millot, A. Pak, Y. Ping, B. B. Pollock, P. Poole, H. G. Rinderknecht, M. B. Schneider, R. F. Smith, G. F. Swadling, C. E. Wehrenberg, O. L. Landen, A. Wan, and W. Hsing (LLNL); J. Benstead and M. Rubery (AWE); R. Hua (UCSD); C. C. Kuranz (University of Michigan); and A. Saunders (University of California, Berkeley)

In FY17, LLNL's Indirect-Drive Inertial Confinement Fusion (ICF-ID) and High-Energy-Density (HED) Physics Programs conducted numerous campaigns on the OMEGA and OMEGA EP Laser Systems. Overall these LLNL programs led

413 target shots in FY17, with 282 shots using only the OMEGA Laser System and 131 shots using only the OMEGA EP Laser System. Approximately 27% of the total number of shots (78 OMEGA shots and 35 OMEGA EP shots) supported the ICF-ID Campaign. The remaining 73% (204 OMEGA shots and 96 OMEGA EP shots) were dedicated to experiments for HED Physics. Highlights of the various ICF-ID and HED Campaigns are summarized in the following reports.

In addition to these experiments, LLNL Principal Investigators (PI's) led a variety of LBS Campaigns using OMEGA and OMEGA EP, including 85 target shots using only OMEGA and 70 shots using only OMEGA EP.

Overall, LLNL PI's led a total of 568 shots at LLE in FY17. In addition, LLNL PI's also supported 30 NLUF shots on OMEGA and 46 NLUF shots on OMEGA EP, in collaboration with the academic community.

Indirect-Drive Inertial Confinement Fusion Experiments

Hydrodynamic Response from Nonuniformities in Plastic, High-Density Carbon, and Beryllium

Principal Investigator: S. J. Ali
Co-investigators: P. M. Celliers, S. W. Haan, S. Baxamusa, M. Johnson, H. Xu, N. Alexander, H. Huang, V. A. Smalyuk, and H. F. Robey

The goal of the Capseed Campaign (comprising Capseed 17A, 17B, and 17C) is to measure shock-front velocity nonuniformities in ICF ablator materials and quantify the level of nonuniformity caused by intrinsic effects. This is done using the OMEGA high-resolution velocimeter (OHRV) to obtain velocity maps of the optically reflecting shock front following release of the ablator material into either PMMA [poly(methyl methacrylate)] for the warm experiments or cryogenic deuterium for the cryogenic experiments. For three half-days in FY17 the focus was twofold: (1) complete measurements on the impact of oxygen heterogeneity and oxygen mitigation layers for glow-discharge polymer (GDP); and (2) begin measuring velocity nonuniformities on deep release from Be, GDP, and high-density carbon (HDC) into D_2 with improved velocity sensitivity.

Performance and yield from fusion capsules at the National Ignition Facility (NIF) are highly dependent on the uniformity of the capsule implosion, and hydrodynamic instabilities are a significant source of performance degradation during the implosion. A possible explanation for unexpectedly large in-flight modulations observed during NIF capsule implosions was a surface oxygenation of GDP; laboratory tests of GDP samples under controlled conditions confirmed the heterogeneous surface oxygenation effect. In FY16 the OHRV was used to test this idea further by obtaining 2-D velocity maps for both oxygen-modulated and unmodulated samples. Modulated samples showed clear evidence of the propagation of a rippled shock wave as a result of the photo-induced oxygen heterogeneity. To mitigate this effect, the target fabrication team proposed depositing a 20-nm oxygen barrier layer of alumina. Tests of the mitigation in the 17A and 17B campaigns determined, via OHRV measurements on warm GDP samples, that this barrier layer introduced no additional perturbations in the shock velocity. In 17C the velocity roughness on deep release from GDP into D_2 with and without this barrier layer was also measured and no significant difference was determined. The velocity nonuniformities in both samples were close to the detection limit of the diagnostic, as described in Fig. 152.82.

The remaining shots in 17A were used to measure velocity nonuniformities slightly below the first shock level in HDC and

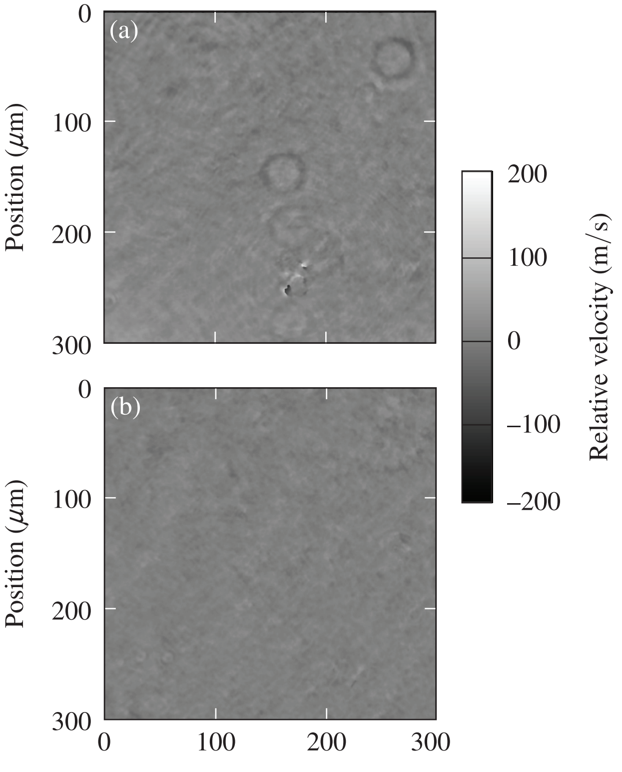

Figure 152.82
Velocity maps from (a) alumina-protected and (b) unprotected glow-discharge polymer (GDP) releasing into D_2. Root mean square (rms) velocity roughness was 8.6 m/s for (a) and 6 m/s for (b), with a diagnostic detection limit of 6 m/s.

at the first shock level in sputtered Be, both releasing into D_2. The velocity nonuniformity for the Be shots varied significantly (35±6 m/s and 24±6 m/s) but in both cases, was ~3 to 5× larger than would be expected from the surface roughness. Nonuniformity in HDC was measured at 7 and 10 Mbar and was found to decrease with increasing pressure (from 124±17 m/s for 7 Mbar to 85±17 m/s for 10 Mbar) but was again a few times larger than predicted from surface roughness alone. These experiments are continuing into FY18, with further cryogenic measurements planned.

Diamond Sound-Speed Measurements Between 8 and 14 Mbar

Principal Investigator: A. Fernandez-Panella
Co-investigators: D. E. Fratanduono and P. M. Celliers

This half-day on the OMEGA laser was designed to collect high-quality data on the sound speed of diamond in the multi-Mbar range, where currently little data exist, for the purpose of constraining equation-of-state models. It was the continuation of the DiamondSS-15B Campaign, where two data points were obtained at 10 Mbar.

The DiamondSS-17A Campaign used planar targets and a direct-drive configuration with a CH ablator, a quartz pusher, and two targets side by side [quartz (standard) and diamond]. The velocity profiles at the free surface were recorded using VISAR as the primary diagnostic (Fig. 152.83). Throughout the day, the laser drive energy was changed in order to probe different shocked pressure states in diamond. The laser pulse was designed to produce a small pressure perturbation that propagated through both the standard and the sample. The wave propagation analysis described in Ref. 34 was applied to extract the sound speed of both materials, quartz and diamond, from their velocity profiles (Fig. 152.84).

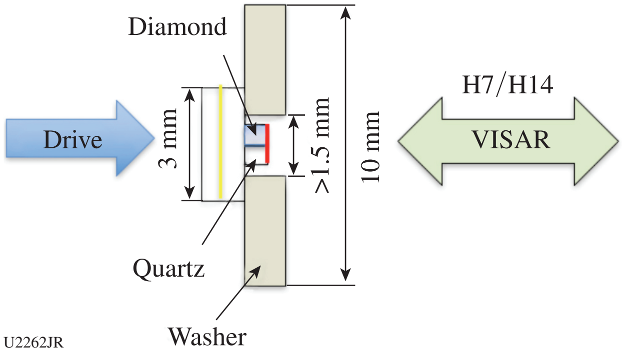

Figure 152.83
Experimental setup and target design for the DiamondSS-17A Campaign.

The results indicate that sound-speed measurements are sensitive enough to constrain EOS models. The Livermore LEOS table 9061 shows good agreement with the data. Further measurements in an extended pressure range are desirable in order to better constrain the models. The results of this campaign are being used to optimize the design for the DiamondSS-18A Campaign, where Be ablators will be used instead of CH to reach higher pressure states; a different pair of etalons will be chosen to increase the accuracy of the velocity measurements to enable extraction of not only the sound speed but also the Grüneissen coefficient.

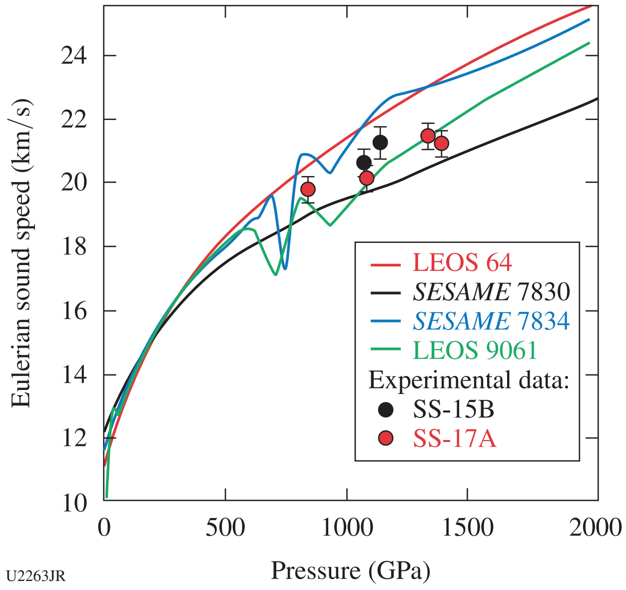

Figure 152.84
Plot of the diamond sound speed versus pressure.

Thomson-Scattering Measurements from Foam- and Gas-Covered Gold Spheres

Principal Investigator: G. F. Swadling
Co-investigators: J. S. Ross, M. Rosen, K. Widmann, and J. D. Moody

The FoamCoSphere-17A Campaign performed foam- and gas-covered high-Z sphere experiments illuminated in direct-drive geometry to investigate atomic physics models, radiative properties of the laser-spot plasma, and the interpenetration of multi-ion species plasmas relevant to ICF indirect-drive–ignition hohlraums. These experiments use laser irradiation at 10^{14} to 10^{15} W/cm^2, similar to the intensities found in hohlraums fielded on the NIF.

For the foam experiments the Au sphere was embedded in a low-density (3.8-mg/cm^3) CH foam [Fig. 152.85(a)]. For the gas-covered experiments, the spheres were located inside a gas bag filled to 1 atm of propane, or 1 atm of a 70/30 mix of propane and methane, to achieve initial electron densities of 4.0% of the critical density of the 3ω drive beams and to mimic the interaction of the hohlraum Au wall with the low-density hohlraum fill gas. Significant target development work was required to prepare the open-geometry foam-covered targets; we look forward to leveraging this target development work in future shot days.

The plasma temperature and density at various radial positions in the blowoff plasma are characterized using Thomson scattering, while x-ray flux from the gold sphere was recorded using the Dante and DMX soft x-ray spectrometer diagnostics. The laser beams use a shaped laser pulse (1-ns square foot, 1-ns square peak) designed to pre-ionize the gas/foam before the main drive pulse.

The electron temperature and density, the plasma-flow velocity, and the average ionization state are measured by fitting the theoretical Thomson-scattering form factor to the observed data. An example of the Thomson-scattering data from ion-acoustic fluctuations is shown in Fig. 152.85. Continued data analysis and simulations are in progress to better understand the plasma evolution and heat transport.

Study of Interpenetrating Plasmas on OMEGA

Principal Investigator: S. LePape

This campaign is designed to study the dynamics of plasma interpenetration in an environment relevant to hohlraums used on the NIF to drive HDC capsules. The question this campaign is trying to answer is whether a fluid description of plasma flows in a low-gas-fill hohlraum (<0.3 mg/cm^3 of helium gas in the hohlraum) is accurate, or if a kinetic description of the flows must be used. Following the first series of shots in 2016 that looked at the time evolution in one point in space in the gap between the two flows, this series of shots focused on 1-D spatially resolved Thomson-scattering data in addition to looking at the effect of helium gas density on the flows' interaction. During this series of shots the helium gas density was changed as well as the ring material (carbon, aluminum, and gold) and the laser energy used to drive the target.

Two main diagnostics are fielded on these experiments: (1) a soft x-ray time-resolved imager looking at the self-emission of the plasmas along the ring axis (Fig. 152.86) and (2) a spatially resolved Thomson-scattering diagnostic (Fig. 152.87) to diagnose electron and ion temperature, flow velocities, and densities.

Time-resolved x-ray images [Figs. 152.86(c) and 152.86(d)] indicate that the helium gas holds the plasma expansion and as time goes by when helium is present, a bright layer appears, presumably being the helium compressed between the low-Z and high-Z plasma.

Figure 152.87 shows a 1-D spatially resolved spectrum acquired on a carbon/carbon shot without helium, providing

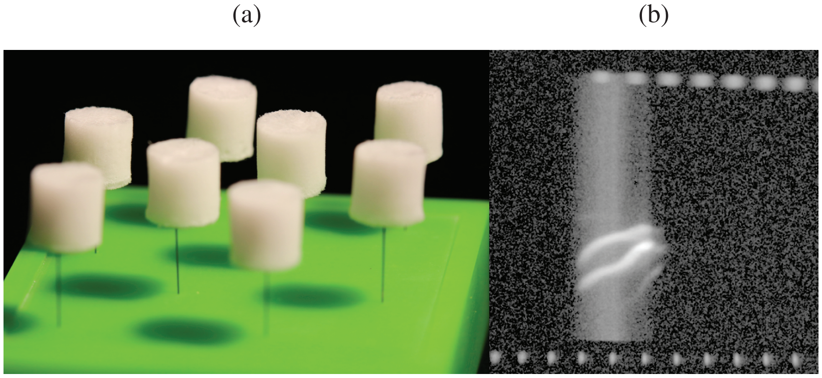

Figure 152.85
(a) Au spheres (1-mm diameter) centered in a 5-mm-diam foam. (b) Example of the Thomson-scattering ion feature, where the Thomson-scattering k vector is directed radially, giving sensitivity to the ablation velocity of the Au plasma.

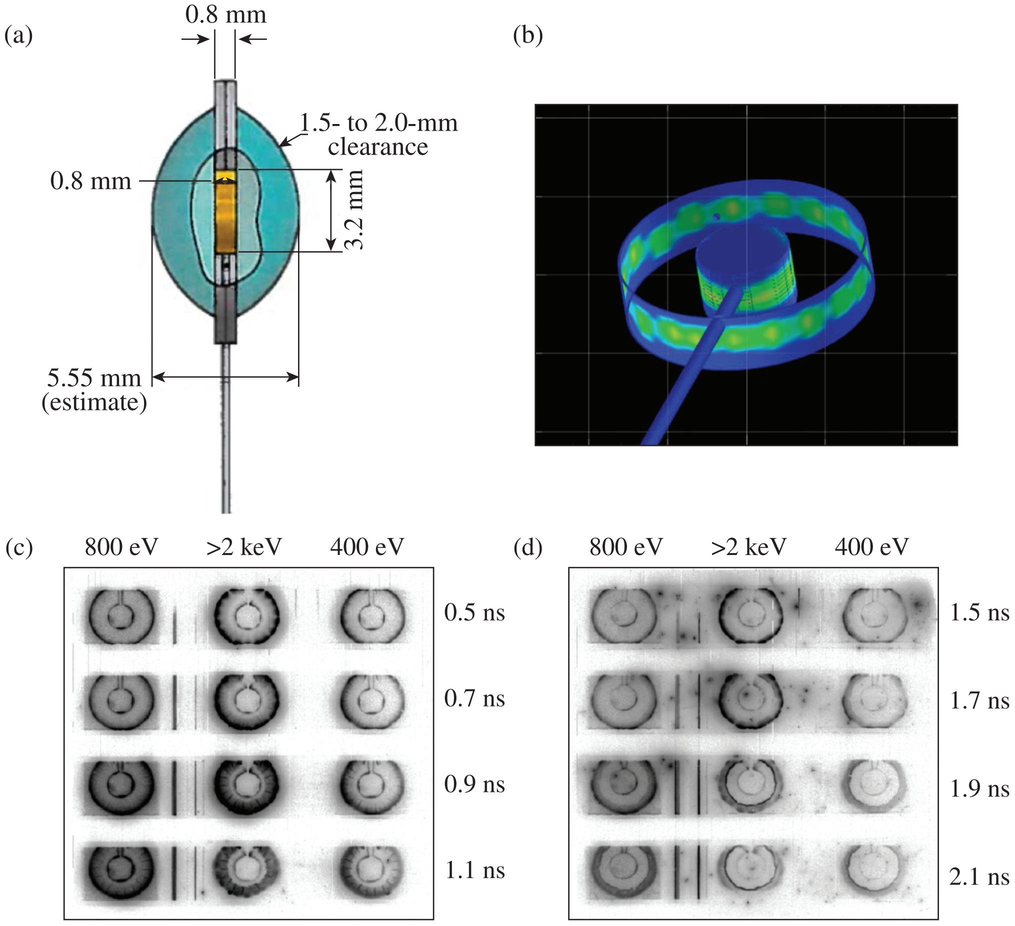

U2265JR

Figure 152.86
(a) Schematic of a gas-bag target. The ring and rod with which the laser interacts are enclosed into a gas bag that holds the helium gas. (b) *VISRAD* calculation of the laser-deposited energy on the ring and high-density carbon (HDC) rod. [(c),(d)] Time-resolved x-ray images of the plasma self-emission. The inner feature is the carbon rod; the outer feature is the low- or high-Z ring. In (c), gold ablates into HDC without a helium fill; in (d), gold ablates into HDC with 0.2 mg/cm^3 of helium gas.

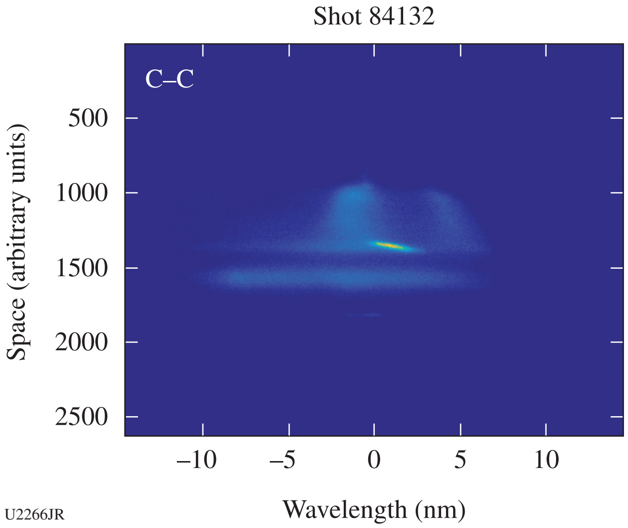

U2266JR

Figure 152.87
One-dimensional spatially resolved Thomson-scattering data of a carbon plasma flowing into a carbon plasma.

information on plasma temperature, densities, and plasma stagnation length. High-quality data were obtained. The results of this campaign are being analyzed.

Measurements of Anisotropy in Non-LTE Low-Density Iron–Vanadium Plasmas

Principal Investigator: L. C. Jarrott
Co-investigators: M. E. Foord, R. F. Heeter, D. A. Liedahl, M. A. Barrios Garcia, G. V. Brown, W. Gray, E. V. Marley, C. W. Mauche, K. Widmann, and M. B. Schneider

Accurate characterization of the effects of geometrical anisotropies on K-shell line emission is very important for improving line-ratio–based temperature measurements in low-density, non-LTE (local thermodynamic equilibrium) plasmas. OpticalDepth-17A built on the OpticalDepth-16A Campaign, which established a working platform for accurately characterizing low-density, mid-*Z*, non-LTE plasmas. Specific goals of this platform included a characterization of heat conduction in the nominal target point design by comparing a layered sample target material to a mixed sample target material. Additionally, this campaign attempted to improve on-target laser drive efficiency by virtue of a picketed pulse shape to improve the laser–target interaction interface. Both OpticalDepth Campaigns used three laser–target configurations, varying target angle to verify the accuracy of data acquired. The primary target was a 10-μm-thick, 1000-μm-diam beryllium tamper with an embedded volumetrically equal mixture of iron and vanadium, 0.2 μm thick and 250 μm in diameter. The second target type was identical to the primary target except that the sample material was layered (50 nm Fe/100 nm V/50 nm Fe) rather than mixed. The third target type was a null target where the beryllium tamper contained no sample material. Three beam-target orientations were used over the course of 14 experimental shots (Fig. 152.88).

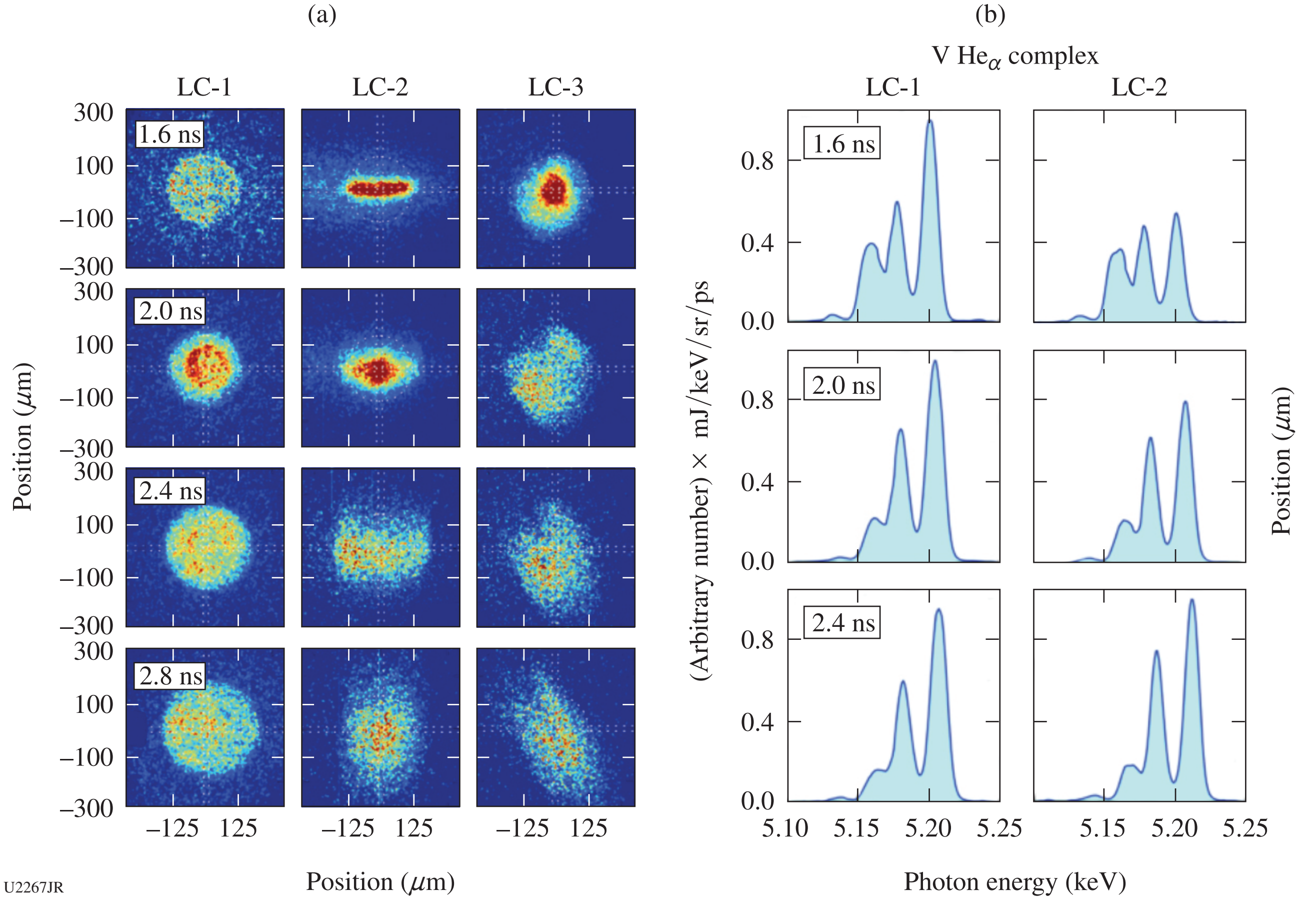

Figure 152.88
(a) X-ray framing-camera images (all from TIM-3) using our three laser/target orientation configurations, showing a face-on view (LC-1), side-on view (LC-2), and 45° view (LC-3). (b) Spectrum measured by the MSPEC spectrometer of the x-ray emission from K-shell transitions in highly charged vanadium and iron using laser/target configurations 1 and 2.

In the first configuration (LC-1), the multipurpose gated x-ray spectrometer (MSPEC) situated in TIM-2 had an edge-on view of the target, while an identical MSPEC in TIM-6 had a face-on view. In the second configuration (LC-2), the target orientation with respect to TIM-2 and TIM-6 was reversed compared with the first configuration. In the third configuration (LC-3), all primary ten-inch–manipulator (TIM)-based diagnostics had a viewing angle of 45° with respect to target normal. Using multiple target-beam orientations resulted in an *in-situ* cross-calibration of the spectrometers and pinhole imagers. The data included simultaneous measurements of (1) time-resolved iron and vanadium K-shell spectra viewed from both the target edge and the target face, and (2) time-resolved images of the expanding plasma, viewed from both the target edge and target face, to infer plasma density for both layered and mixed sample target materials. The K-shell spectral data provided time-resolved electron temperature measurements of the expanding plasma, with preliminary analysis implying a plasma temperature above 2 keV.

Imaging Electric-Field Structure in Strong Plasma Shocks

Principal Investigator: H. G. Rinderknecht
Co-investigators: H.-S. Park, J. S. Ross, S. C. Wilks, and P. A. Amendt

This series of shots was designed to measure the electric fields produced by strong shocks in single- and multi-species plasmas. Strong shocks ($M > 1.6$) produce electric fields as a result of streaming of the electron precursor ahead of the ion shock, which is not accurately reproduced in hydrodynamic models. This experiment is intended to quantify electric-field strength and position in a shock platform previously characterized in FY16 (Ref. 35) to be used to constrain high-fidelity physics codes.

The KineticDynamics-17A Campaign performed proton radiography of a shock-tube target platform developed in the KineticShock-16 series. Ten beams with 2.5 kJ in a 0.6-ns impulse drove a 2-μm-thick SiO_2 ablator attached to one end of the tube, launching a strong shock into the 1 atm of gas contained in the tube. A D^3He-filled backlighter capsule was imploded to produce 3.0- and 14.7-MeV protons, which transited perpendicular to the shock front and were recorded using CR-39. Deflections of the protons caused by electric fields were recorded as changes in the proton fluence with position on the detector, as shown in Fig. 152.89. Gas fills of H_2 (two shots), Ne (three shots), and H_2 + 2% Ne (six shots) were probed while varying the backlighter timing relative to the shock.

Radiographs were collected on all shots, demonstrating electric-field formation at both the shock front and the ablator/gas interface. X-ray framing-camera images recorded perpendicular to the radiography axis confirm that the flow velocity is consistent with previous experiments (450 μm/ns) and identify

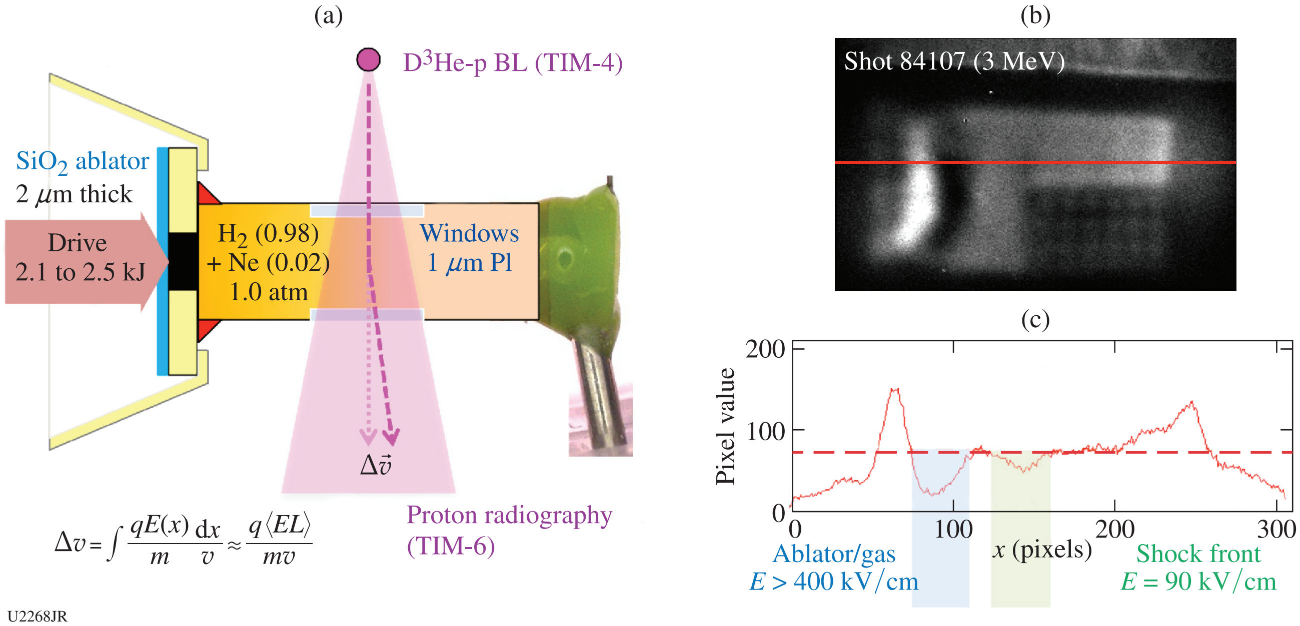

U2268JR

Figure 152.89
(a) Experimental configuration, (b) 3-MeV proton radiograph, and (c) lineout of proton fluence for shot 84107.

the position of the SiO_2 ablator at the radiography sample time on each shot. Analysis is ongoing and results were presented at the APS DPP Meeting in October 2017.

Measuring Thermal Conductivity of D_2

Principal Investigators: S. Jiang and Y. Ping
Co-investigators: P. M. Celliers and O. L. Landen

This campaign successfully developed a platform of refraction-enhanced x-ray radiography for planar cryogenic targets and obtained usable radiographs. The campaign fielded two half-days on OMEGA during FY17. The series of cryogenic shots was designed to measure the thermal conductivity of liquid D_2 at 1 to 10 eV, which helps to benchmark different transport models used in ICF ignition target design. Figure 152.90 shows the experimental configuration. The CH and liquid D_2 were heated to different temperatures by the x rays generated from heating lasers incident on a thin Zn foil. This builds up a density gradient because of thermal conduction. The evolution of the CH/D_2 interface was measured using refraction-enhanced x-ray radiography with high spatial resolution. The temperature can be constrained by the wave velocities in CH/D_2. A vanadium foil backlighter was used to generate the probing x rays. The backlit x-ray images were collected with a four-strip framing camera. Useful radiographs at different delays were recorded (shown in Fig. 152.90), including undriven and driven data at 0.5 ns, 1.5 ns, 2 ns, and 2.5 ns. Analysis of the measured data is in progress.

Characterization of Laser-Driven Magnetic Fields

Principal Investigator: B. B. Pollock
Co-investigators: C. Goyon, G. J. Williams, D. Mariscal, G. F. Swadling, J. S. Ross, S. Fujioka, H. Morita, and J. D. Moody

BFieldLoop-17A and -17B continued the laser-driven magnetic-field experimental campaign on OMEGA EP. The goal for 17A was to study the impact on the magnetic-field–generation process of modifying the target geometry, while the primary

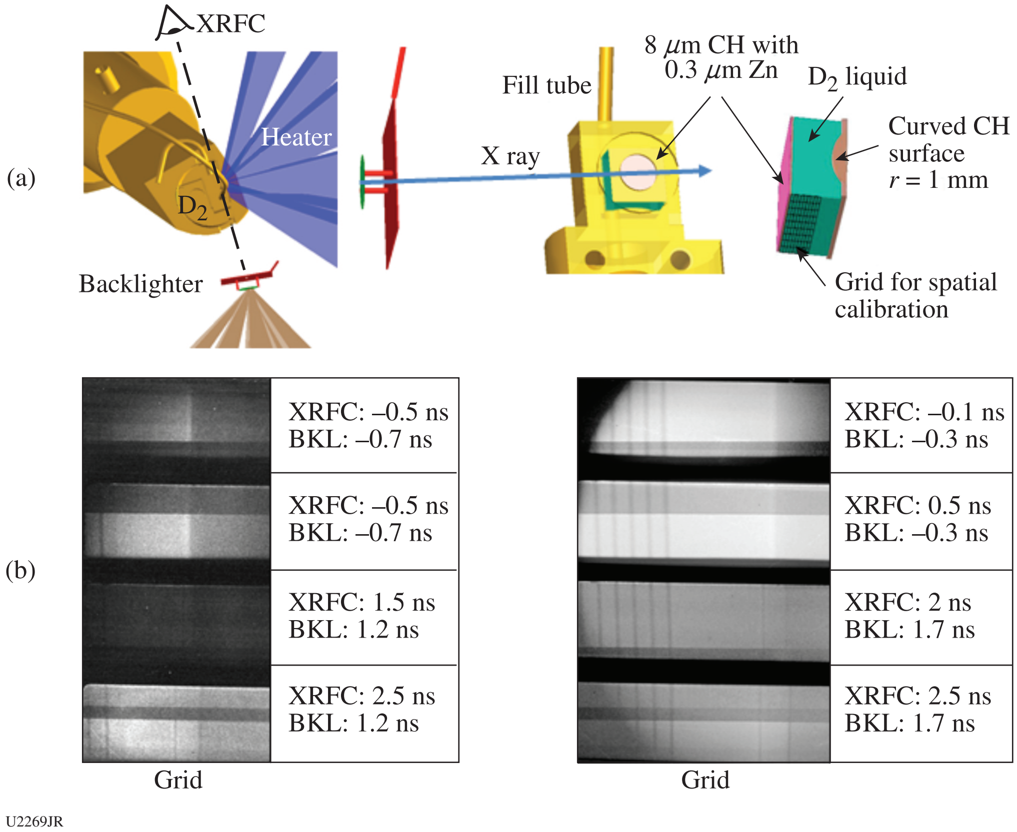

Figure 152.90
(a) The experimental configuration, target geometry, and (b) raw radiographs from an x-ray framing camera (XRFC). The delays of both the framing camera and the x-ray backlighter (BKL), with respect to the heating pulses, are shown in the table next to each radiograph.

objective for 17B was the extension of the probing time for the field. Figure 152.91 shows the general experimental geometry. The field is produced by currents flowing in a U-shaped gold foil target. One or two long-pulse beams are directed through holes in the front side of the target to produce a plasma on the interior rear side of the target. Plasma produced in this region expands toward the front side, setting up a voltage across the target that drives the current. The fields are measured by proton deflectometry, where the protons are produced through target normal sheath acceleration by the OMEGA EP backlighter beam incident on a separate, thin Au foil.

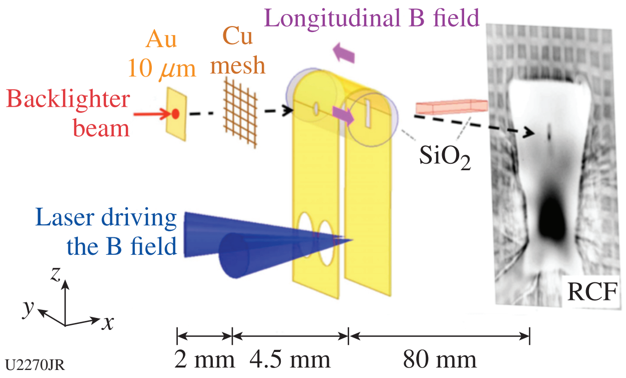

Figure 152.91
Experimental configuration for BFieldLoop experiments. RCF: radiochromic film.

Previous experiments showed that for a 1-TW long-pulse laser drive, fields of ~200 T can be produced in the interior of the loop portion of the target. The 17A experiment modified the front of the target by removing the bottom portion where the laser holes are located. This target modification showed a difference in the resulting proton images recorded on the radiochromic film (RCF), and modeling is ongoing to quantify the modification to the field strength and topology.

For 17B, a gold shield was added between the main target and the backlighter target to protect the rear surface of the backlighter and allow for late-time probing of the magnetic fields. Prior to 17B the ability to measure magnetic fields after the long-pulse beams turned off had been limited. By using a 750-ps long-pulse B-field drive beam, the addition of this shield allowed the probe time to be extended from 750 ps (the end of the drive beam) to 16 ns. Preliminary analysis of these results indicates that the magnetic field persists long after the drive laser turns off, decaying exponentially with a time constant of ~2 ns. This is consistent with a circuit theory treatment of the interaction, where the drive laser acts as a voltage source while turned on; after the voltage is turned off, the current (and consequently the magnetic field) decays with the *L*/*R* time constant of the target. For the geometry of the 17B targets, this *L*/*R* time is ~2.6 ns.

Study of Shock Fronts in Low-Density Single- and Multi-Species Systems

Principal Investigator: R. Hua (UCSD)
Co-investigators: Y. Ping, S. C. Wilks, R. F. Heeter, and J. A. Emig (LLNL); H. Sio (MIT); C. McGuffey, M. Bailly-Grandvaux, and F. N. Beg (UCSD); and G. W. Collins (LLNL, LLE)

This series of shots is designed to study the shock-front structure of low-density single- and multi-species systems in a planar geometry, using proton radiography from a broadband TNSA source and x-ray emission spectroscopy. Unlike most other low-density shock experiments that are mostly carried out in convergent geometry with near-monoenergetic D^{3}He proton radiography, the planar geometry of these experiments enables one to distinguish the shock front from its pusher, and the TNSA protons provide broadband energy measurements.

In this platform, the strong shock of interest is initiated by launching three long-pulse beams from OMEGA EP onto a 2-μm SiO$_2$ foil (Fig. 152.92). By ablation, the foil pushes into a cylindrical kapton tube that is prefilled with either pure helium or a helium/neon mixture. A short-pulse beam is fired a few nanoseconds after the shock-driving beams, onto a TNSA proton target normal to the axis of the kapton tube. The protons are driven through two windows on the tube into a stack of RCF's on the other side. Photons emitted from the shock front through another window are recorded by a 1-D spatially resolved soft x-ray spectrometer [called variable-spaced grating (VSG)]. The details of the design and its feasibility have been published.[7]

With pure helium fill, a proton accumulation layer at the shock front, resulting from a self-generated electric field, has been recorded on the RCF. A discussion of the field information inferred from the proton behavior was published recently.[12] Shocks in the mixed gas displayed different features. Not one, but two proton accumulation layers are observed. In addition, line emission from the added neon gas is recorded by the VSG, which provides the potential to constrain the temperature and density of the shock front. Further analysis of these results is in progress. Results of these campaigns are being used to further optimize the platform to make more measurements in FY18.

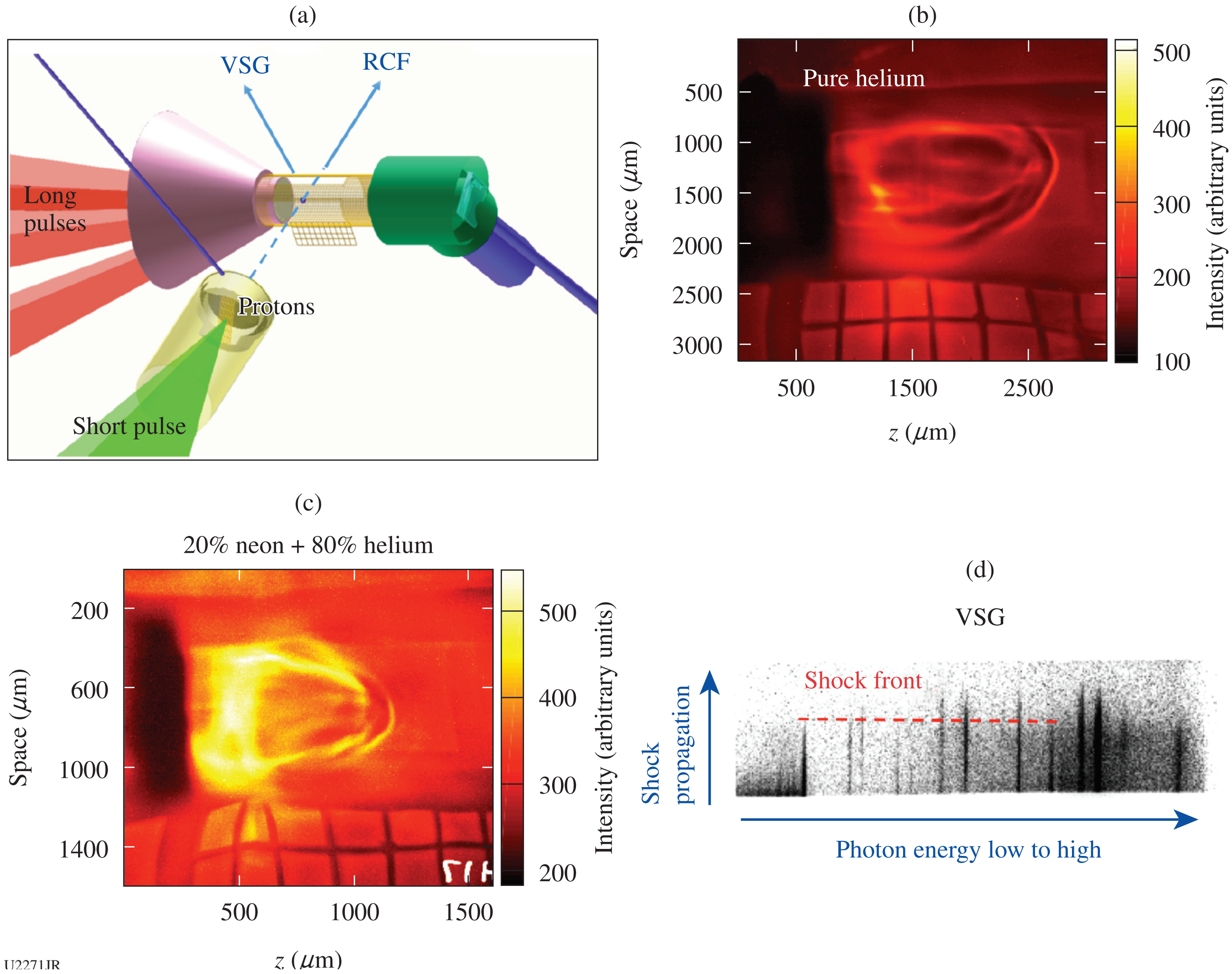

Figure 152.92
(a) Experimental setup; RCF data from (b) a pure helium shot and (c) a mixture shot (20% neon and 80% helium); (d) VSG spectrometer data from a mixture shot.

High-Energy-Density Experiments

1. Material Equation of State and Strength Measured Using Diffraction

Measurement of Pb Melt Curve Along the Hugoniot Using* In-Situ *Diffraction

Principal Investigator: C. E. Wehrenberg

Co-investigators: R. Kraus, F. Coppari, J. M. McNaney, and J. H. Eggert

This series of shots was designed to measure the melt curve of Pb on the Hugoniot using *in-situ* x-ray diffraction on OMEGA EP's PXRDIP diagnostic. The physics package consists of a 40-μm epoxy ablator, a 12.5-μm lead foil, and a 100-μm LiF window for VISAR. A single UV beam is used to drive a steady shock through the ablator and into the Pb sample. A separate beam drives a Ge x-ray source target, and the diffracted x rays are collected on image plates mounted on the inside of the PXRDIP box. The solid or liquid state of the shock-compressed lead is determined by the presence of a diffraction signal as either sharp lines (solid) or a single diffuse line (liquid). Figure 152.93 shows a diffraction pattern containing both the diffuse liquid signal from lead under 47 GPa of shock compression and sharp diffraction lines generated by the Pt pinhole.

This campaign is performed in conjunction with similar campaigns on the NIF and the Linac Coherent Light Source

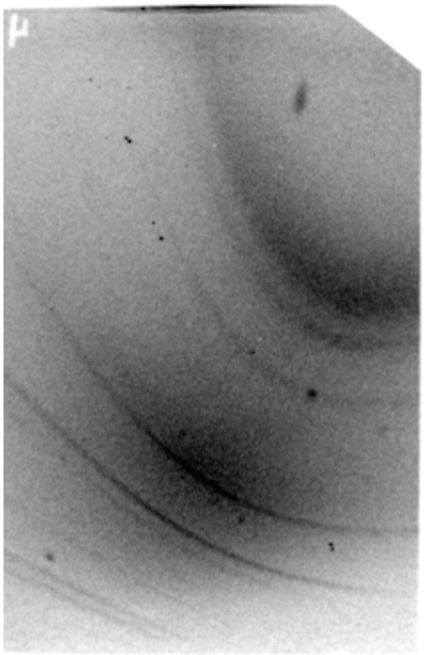

Figure 152.93
Example diffraction image showing a diffuse signal generated by liquid Pb under shock compression at 47 GPa and sharp diffraction lines generated by the Pt pinhole.

(LCLS). The epoxy ablator setup, which eliminates reverberations between the ablator and any glue layers, and the Ge x-ray source target were developed on the NIF campaign before being applied on these shots. On this OMEGA EP day, alternating beams to increase the shot rate achieved 11 shots that provided a large data set to map the melt curve on the Hugoniot. This data will be compared with similar experiments performed on LCLS, making it possible to compare shots done with greater x-ray diffraction precision (because of the x-ray free-electron laser) with the greater-precision shock drive available on OMEGA EP. In addition, these melt curve measurements will be used in the design of future NIF shots using shock-ramp combination drives to measure melt curves in off-Hugoniot states.

Development of a New Platform for Measuring Recrystallization

Principal Investigator: F. Coppari
Designer: R. Kraus
Co-investigators: C. E. Wehrenberg and J. H. Eggert

This campaign seeks to develop a platform for measuring recrystallization of Pb through shock-ramp compression. By first launching an initial shock to compress the sample along the Hugoniot close to the melting pressure, letting the sample release into the liquid phase, and then recompressing it with ramp compression across the solid–liquid phase boundary, one can measure high-pressure melting lines of materials. The structure of the Pb upon shock, release, and ramp compression is monitored by x-ray diffraction. The onset of melting is identified by the appearance of a diffuse scattering pattern and the disappearance of the Bragg diffraction lines characteristic of the solid. The pressure is monitored by VISAR looking at the interface between the Pb and a LiF window.

Building upon the successful use of Be ablators initiated in FY16, the FY17 series used a slightly modified target design that included a Ge preheat shield (Fig. 152.94). Hydrocode simulations allowed us to design a suitable laser pulse shape to compress the Pb sample along this complicated shock–release–ramp path.

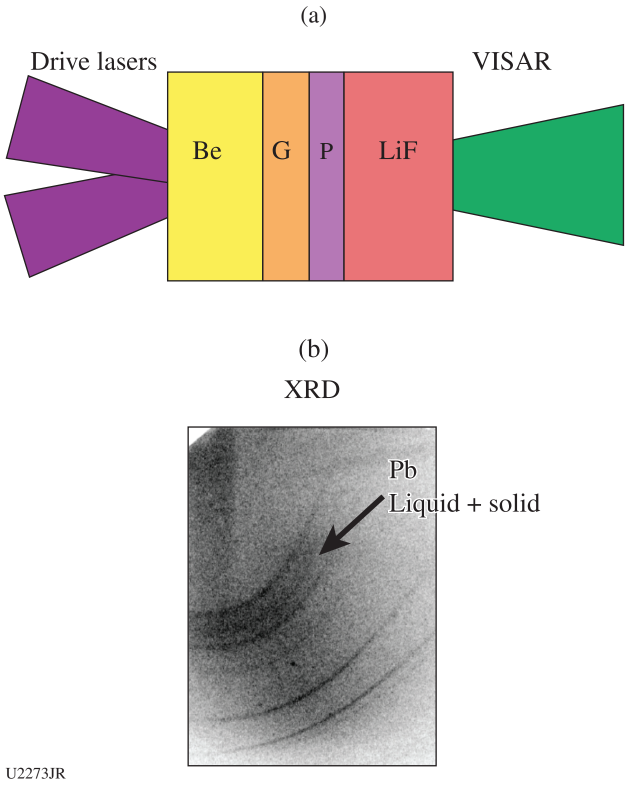

Figure 152.94
(a) Target schematic and (b) example of a diffraction image showing diffuse (liquid) and sharp (solid) features from the Pb sample. VISAR: velocity interferometer for any reflector; XRD: x-ray diffraction.

Diffraction data indicate that Pb completely melts above 50 GPa along the Hugoniot. Resolidification into a structure consistent with the bcc lattice has been observed upon subsequent ramp compression to higher pressures. Data analysis is ongoing and will provide valuable information for future OMEGA and NIF campaigns.

High-Pressure Crystal Structure of Ramp-Compressed Pb and Ta to Resolve Known or Potential High-Pressure Phase Transformations

Principal Investigator: A. E. Lazicki
Co-investigators: F. Coppari, R. Kraus, C. E. Wehrenberg, J. M. McNaney, D. Swift, D. Braun, and J. H. Eggert (LLNL); and J. R. Rygg, D. N. Polsin, and G. W. Collins (LLE)

Several previous experiments on OMEGA, OMEGA EP, and the NIF in the past five years have examined the crystal structure of Pb and Ta at high pressure. Pb is of specific interest because its high-pressure/high-temperature phase diagram, including two phase transformations, is well constrained between 0 to 100 GPa from diamond-anvil cell experiments. Therefore, it provides an opportunity to test for the effects of rapid compression and heating, inherent from ramped laser drives, on phase boundaries. Although very high quality data have already been collected in the 100- to 500-GPa pressure regime, previous measurements have failed to reach sufficiently low pressures to cross the two known phase boundaries. Meanwhile, measurements of Ta structure have suggested a possible new high-pressure phase, but contamination of the diffraction pattern by diamond, a material that has always been present in the target packages, has made the determination ambiguous. The goals of this OMEGA EP campaign were to capture the low-pressure phase transformations in Pb and, in the case of Ta, to eliminate all diamond from the target and examine the pressure regime where previously a new phase was suggested. Both target packages used beryllium ablators and LiF windows, with thin (3- to 5-μm) layers of Pb. The shots used a combination of Cu and Ge backlighter sources.

Very high quality diffraction data were collected on all shots and the low-pressure phases of Pb were clearly observed and followed with pressure, constraining the phase boundaries (Fig. 152.95). The diagnostic damage incurred from the explosive ablation of beryllium made it impossible to reach the desired pressure regime for the Ta measurements, but the measurements provided at least a clear lower bound to the transition. These results were presented at an invited talk at the 55th meeting of the European High-Pressure Research Group and are being prepared for publication.

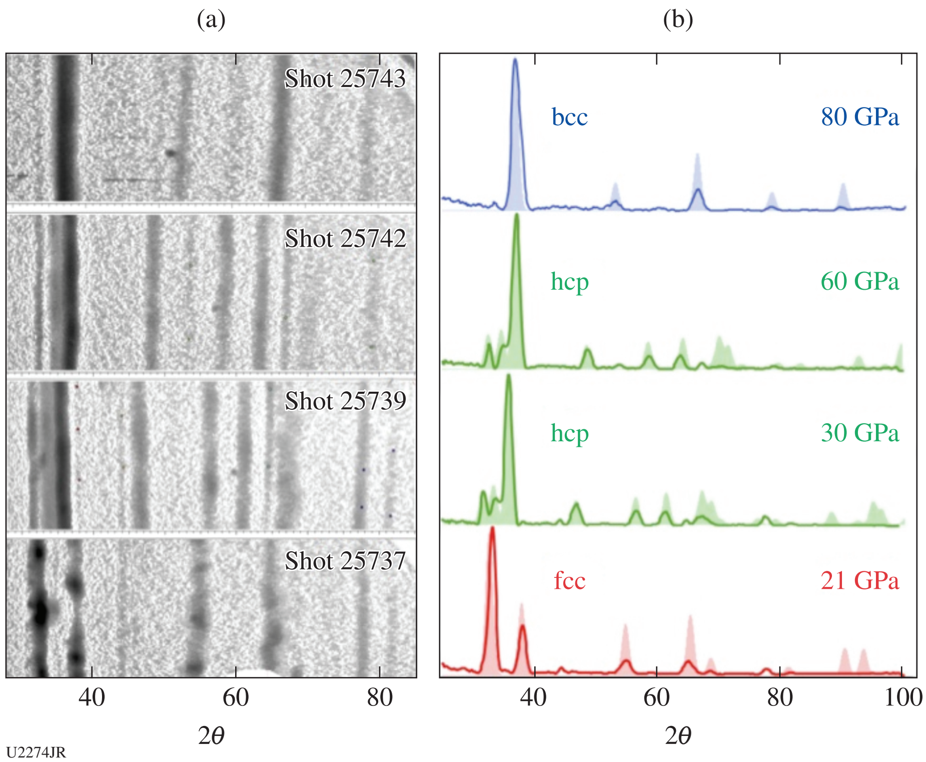

U2274JR

Figure 152.95
(a) Raw data and (b) integrated diffraction patterns from three phases of Pb. A Cu He$_\alpha$ x-ray source was used.

Development of an In-Situ *Pressure Standard for Diffraction Experiments*

Principal Investigator: F. Coppari
Co-investigators: J. H. Eggert and R. Kraus

The goal of this campaign is to develop a new way of determining pressure in diffraction experiments, based on the use of an *in-situ* pressure gauge. By measuring the diffraction signal of a standard material (whose equation of state is known) compressed together with the sample, one can determine the pressure reached during ramp compression.

Currently, pressure is determined from VISAR measurements of diamond free-surface velocity or particle velocity through a transparent window (such as LiF or MgO). This method is, in some cases, ambiguous (lack of reflectivity or shock formation) or relies on assumptions and equation-of-state models. Cross-checking the VISAR measurement with *in-situ* pressure determination using the diffraction signal of a standard material will improve the diffraction platform by providing a complementary way of determining the pressure state within the sample, with great impact to the programmatic effort of determining structures and phase transitions at high pressure and temperature. In addition, combining pressure determination from VISAR and from the *in-situ* gauge can provide information about the temperature of the sample by measuring the calibrant thermal expansion.

Building upon the results obtained in FY16, this FY17 campaign focused on the study of Au, Ta, Pt, and W pressure standards ramp compressed to 2 Mbar on OMEGA. Data were collected on eight successful shots in a half-day, including diffraction patterns of the Au/Ta and Pt/W pairs. All shots provided useful data (Fig. 152.96). Comparison of the pressures obtained from VISAR analysis and from the diffraction patterns will yield information on the accuracy of the VISAR method as well as on the existence of preheating.

Future directions of this work will look at characterizing the pressure standards at higher pressure and implementing this technique into other diffraction experiments. This platform still requires additional development before it can be used routinely in diffraction experiments, but the data collected so far are extremely encouraging and suggest that the use of an *in-situ* pressure gauge can be a viable path forward in future x-ray diffraction (XRD) measurements on both OMEGA and the NIF.

Development of Simultaneous Diffraction and EXAFS Measurements

Principal Investigator: F. Coppari
Co-investigators: Y. Ping and J. H. Eggert

Being able to measure simultaneous diffraction and an extended x-ray absorption fine-structure (EXAFS) signal in the same shot will be an enormous advance for laser-based materials experiments, providing a simultaneous probe of both the long-range [x-ray diffraction (XRD)] and short-range (EXAFS) order of the material, as well as two complementary probes of the Debye–Waller factor to gain information about the temperature state of the material under investigation. The approach successfully developed in FY16 was to use the PXRDIP diagnostic to measure diffraction and the x-ray source spectrometer to measure EXAFS. The challenge was to find a single suitable backlighter that would generate both a monochromatic (for diffraction) and broadband (for EXAFS) x-ray source. Success was achieved in measuring simultaneous

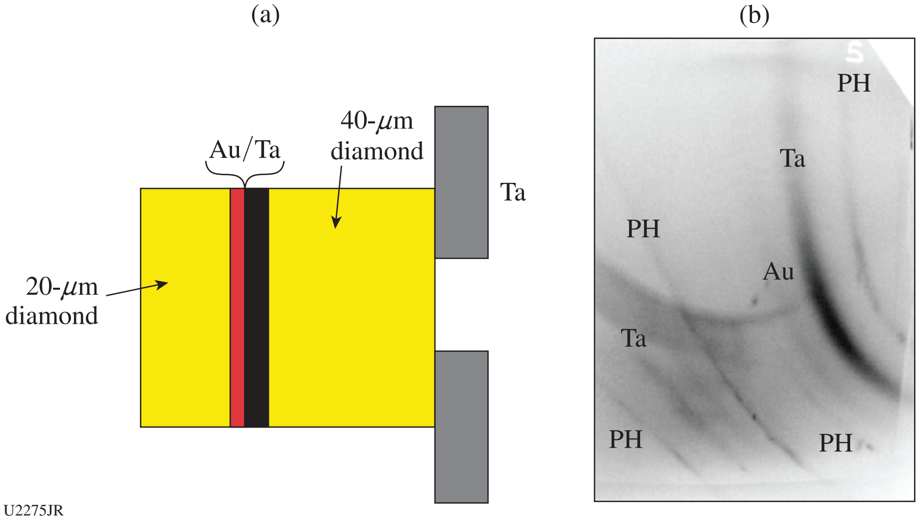

Figure 152.96
(a) Target schematic and (b) example of a diffraction image showing features from Au and Ta.

XRD and EXAFS of Fe by using a dual-foil bremsstrahlung backlighter, where one foil is optimized to generate He$_\alpha$ radiation for diffraction and the other to generate a continuous and broadband x-ray source for EXAFS (see Fig. 152.97).

The goal for the FY17 campaign was to improve the quality of the EXAFS measurement by using a higher-Z foil to increase the bremsstrahlung radiation, thereby generating a brighter x-ray source to allow EXAFS measurements at a higher energy (Zr K edge at 18 keV). Both Au and Ta were tested as x-ray sources for EXAFS and Fe or Cu as an x-ray source for diffraction. The spectrum generated by Au is indeed brighter, but it was not yet possible to see the EXAFS modulation above the Zr K edge. Poor spectral resolution certainly played a role in the deterioration of the EXAFS data: in this experimental setup, the spectral resolution is limited by the x-ray source size, which is enlarged by the expanding plasma generated by direct laser ablation of the foil. Further improvement could be obtained by using a spectrometer with focusing geometry that would be less sensitive to the effects of the source size.

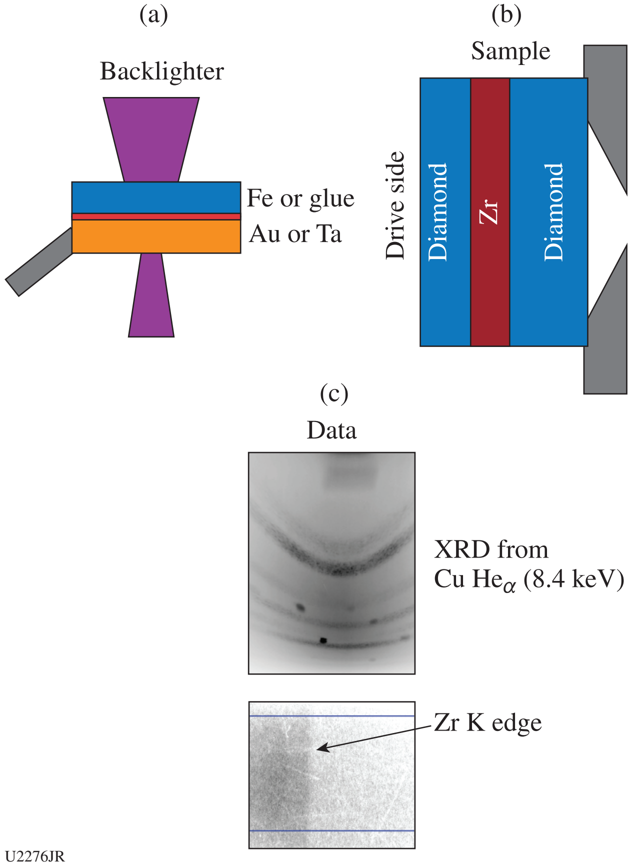

Figure 152.97
Target schematics for the (a) backlighter and (b) physics package, respectively; (c) example of diffraction and EXAFS images.

Texture Diffraction and Recovery of Shock-Compressed Samples for Ex-Situ *Study*

Principal Investigator: A. Krygier
Co-investigators: C. E. Wehrenberg, H.-S. Park, and D. C. Swift

This shot day continued the previous work of Wehrenberg on highly textured Ta that studied the deformation response of Ta to shock waves. The goal of these shots is to study if effects seen on the initial shock are present during a second shock. In particular, twinning, which is not included in the Livermore strength model for Ta, was observed to play a significant role in deformation over a wide range of shock pressures (30 to 150 GPa). X-ray scattering was measured using the PXRDIP platform in combination with VISAR on OMEGA EP.

These shots included a time series of x-ray diffraction measurements of various pressure histories. In the first configuration, the sample was shocked to the twinning regime, released, and then shocked above twinning. Twinning was observed, as shown by the red circle in Fig. 152.98, in the initial shock but not on release or on the second shock. In the second configuration, the sample was shocked to the twin-

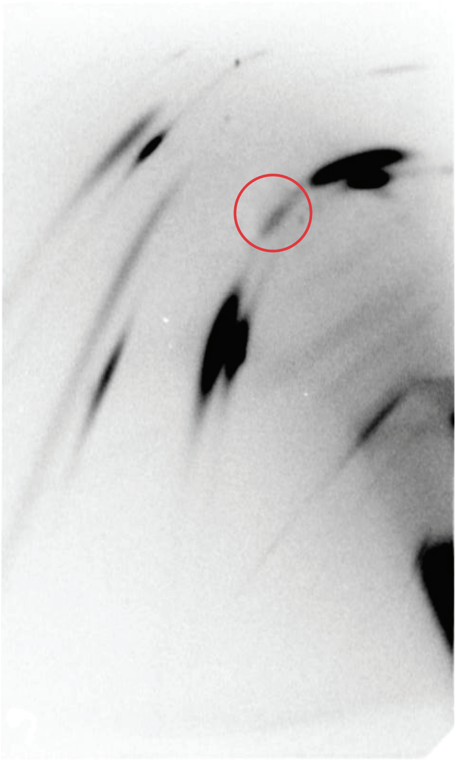

Figure 152.98
Diffraction image for shocked tantalum, showing twinning feature (circled).

ning threshold, released, and then shocked into the twinning regime. Twinning was not observed on either the release or the second shock, suggesting that dislocations generated by a shock wave moderate the deformation response. In addition, a shock-ramp history was performed, using the initial shock in the twinning regime that is approximately analogous to strength experiments in Ta performed on the NIF. In this regime, a new texture was observed that cannot be explained by twinning. Analysis is ongoing.

2. Material Equation of State Using Other Techniques

Development of a Platform for Equation-of-State Measurements Using Flyer Plate Impact

Principal Investigator: F. Coppari

Co-investigators: R. London, P. M. Celliers, M. A. Millot, D. E. Fratanduono, A. Lazicki, and J. H. Eggert

This ongoing campaign is developing a platform to use OMEGA to accelerate flyer plates to a high velocity for absolute equation-of-state (EOS) measurements by symmetric impacts. The concept is to ramp compress a metallic foil through indirect laser ablation across a vacuum gap and observe the flyer impact on a same-material sample, mounted side by side with a transparent LiF window (Fig. 152.99). By measuring the flyer-plate velocity through the transparent window prior to impact, and the resulting shock velocity in the metallic sample using transit time measurements, the principal Hugoniot of the metallic foil can be determined *absolutely* (e.g., without needing a known pressure reference), enabling one to develop an EOS standard.

Specifically, this campaign tested three flyer-plate materials to check performance and hydrodynamic prediction capabilities. Plates of Mo, Cu, and W were chosen because they can be "easily" ramp compressed to a high pressure and do not exhibit structural solid-phase transitions. Building upon the previous FY16 campaign, a successful half-day of eight shots was fielded in FY17, accelerating flyer samples to different velocities. While Cu and W showed anomalous behavior, such as flyer breakup resulting in the loss of VISAR reflectivity before impact, Mo was successfully accelerated to 14 km/s, corresponding to a shock pressure into the Mo sample of ~1 TPa. As Fig. 152.99 shows for the lower-pressure shot, the velocity ramps up smoothly and VISAR data are obtained up to impact. The impact actually shocked the LiF window into a pressure range where it was no longer transparent, impairing the VISAR signal. Future experiments will look at accelerating Mo flyer plates to different pressures to characterize its Hugoniot EOS in a wide pressure range, using quartz as a transparent window.

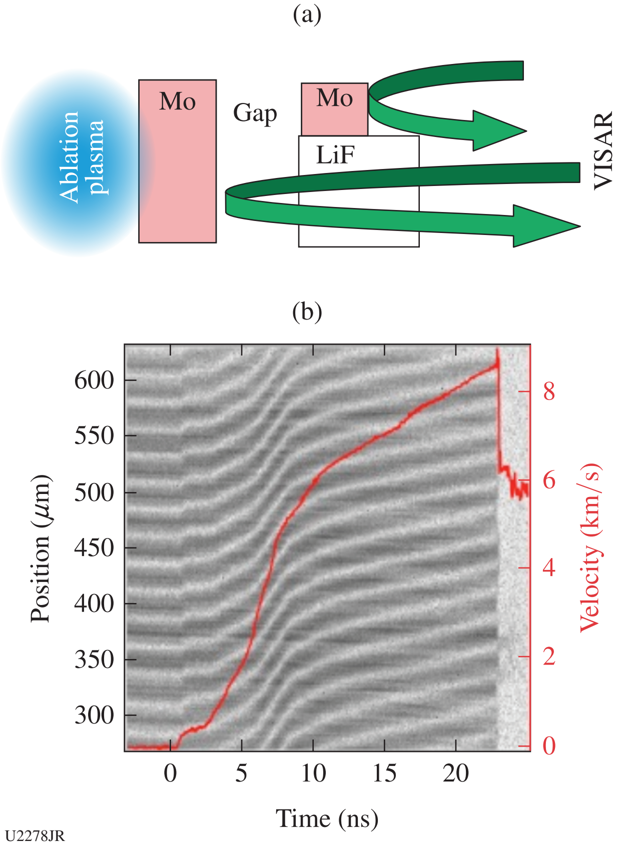

Figure 152.99
(a) Experimental concept and (b) sample VISAR data.

Development of Simultaneous EXAFS and VISAR Measurements

Principal Investigator: Y. Ping

Co-investigators: F. Coppari and J. H. Eggert

This campaign aims to test mirror shielding for simultaneous VISAR measurements in the presence of the implosion backlighter needed for EXAFS measurements. Both the VISAR and EXAFS measurements must pass through the sample, so an x-ray transparent optical mirror is used to redirect the VISAR probe beam onto the sample. This mirror is, however, vulnerable to blanking. For these FY17 shots a tilted mirror design was implemented to move the mirror out of the line of sight of the x-ray transmission path, so that more shielding of the mirror could be applied. This design extended the mirror life time by about 1 ns, but after that, the mirror was still blanked and the VISAR signal lost. On the other hand, good EXAFS data were collected for the Co K edge for the first time, as shown in Fig. 152.100. Separate shots for VISAR without the implosion also produced good VISAR data to characterize the pressure. The similar experimental design on the NIF has

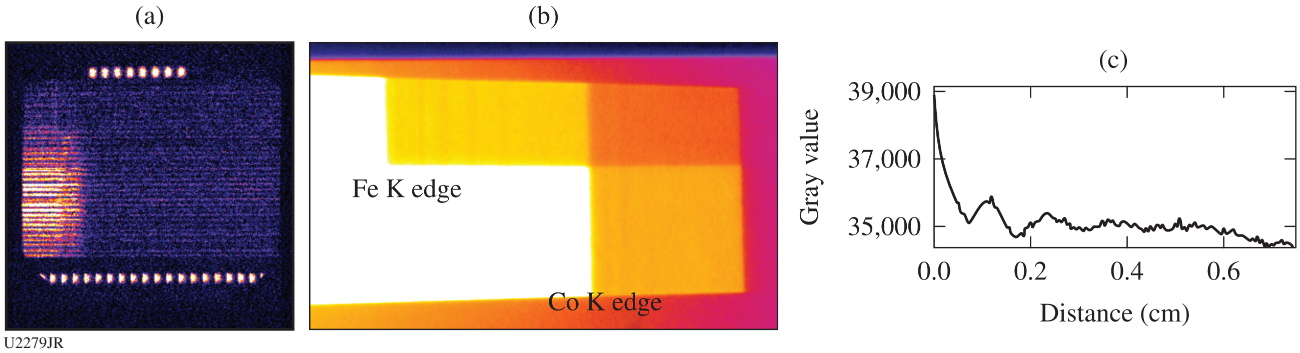

Figure 152.100
(a) Raw image of VISAR, showing blanking of the mirror delayed by ~1 ns. (b) EXAFS spectra at the Fe and Co K edges. (c) The lineout shows the EXAFS modulations at the Co K edge.

the mirror positioned behind the target, which survived and produced a VISAR signal in the presence of the implosion in a recent NIF shot.

Development of a Platform for EXAFS Measurements at the L Absorption Edge of High-Z Materials

Principal Investigator: F. Coppari
Co-investigators: Y. Ping and J. H. Eggert

EXAFS measurements in the 7-keV x-ray region are routinely performed on the OMEGA laser during shock and ramp compression. However, because the brightness of the capsule implosion used as an x-ray source decreases at high energy, measuring the EXAFS of materials with an absorption edge higher than 7 keV is very difficult in a single shot. In addition, as one seeks to study higher-*Z* materials and observe the L absorption edge, the amplitude of the EXAFS signal decreases as well because the cross section for the absorption at the L edge is lower than at the K edge. These issues make these measurements extremely challenging.

In prior years the TaXAFS Campaigns looked at the Ta L3 edge (~10 keV) and were able to obtain a good signal-to-noise ratio by averaging 15 shots or by using a multicrystal spectrometer.[36] The goal of the FY17 campaign is to look at materials whose L edge is closer to 7 keV, where the number of photons generated by the capsule implosion is higher, to see if a good signal can be obtained in a single shot. The shots studied the Ce L3 edge (5.7 keV), but although a nice contrast at the Ce L edge has been measured, no clear EXAFS modulations could be observed in a single shot (Fig. 152.101), probably also a result of limited spectral resolution. This suggests that in order to successfully measure L-edge EXAFS, a spectrometer with focusing geometry is needed to increase the signal because of the higher collection efficiency and reduce the sensitivity to x-ray source size broadening, therefore improving the quality of the data.

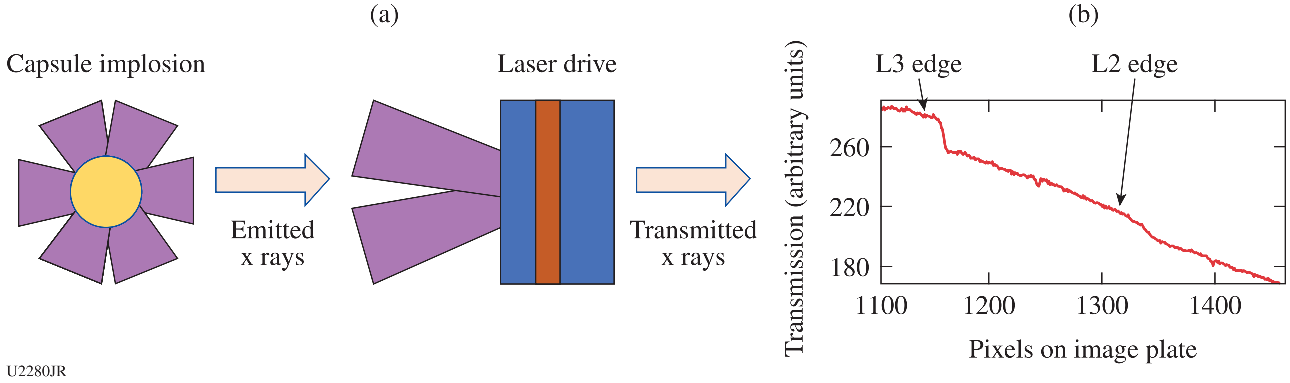

Figure 152.101
(a) Experimental concept and (b) sample EXAFS data.

Development of Spherically Convergent Equation-of-State Measurements

Principal Investigator: A. E. Lazicki
Co-investigators: D. Swift, A. M. Saunders, T. Doeppner, R. Nora, F. Coppari, R. London, P. M. Celliers, J. H. Eggert, G. W. Collins, H. Whitley, J. Castor, and J. Nilsen

This campaign is developing a platform for measuring Hugoniot EOS at pressures much higher than can be achieved using a standard planar drive. This platform is intended to collect data in the pressure regime of 100+ Mbar, where currently very little data exist for any material, for the purpose of constraining EOS models.

The FY17 campaigns first used a hohlraum (indirect drive) to launch converging shock waves into solid spheres of CD (deuterated) and CH (normal) plastic. Along the axis of the hohlraum, vanadium He$_\alpha$ backlit 2-D x-ray images of the imploding sphere were collected with a framing camera. On some shots, x-ray Thomson-scattering measurements were also made using a Zn backlighter and a spectrometer at the hohlraum equator [Figs. 152.102(a) and 152.102(b)]. The radiographs yield density and shock velocity that make it possible to calculate the shock state using the Rankine–Hugoniot equations, and the scattering data yield information about temperature and ionization state.

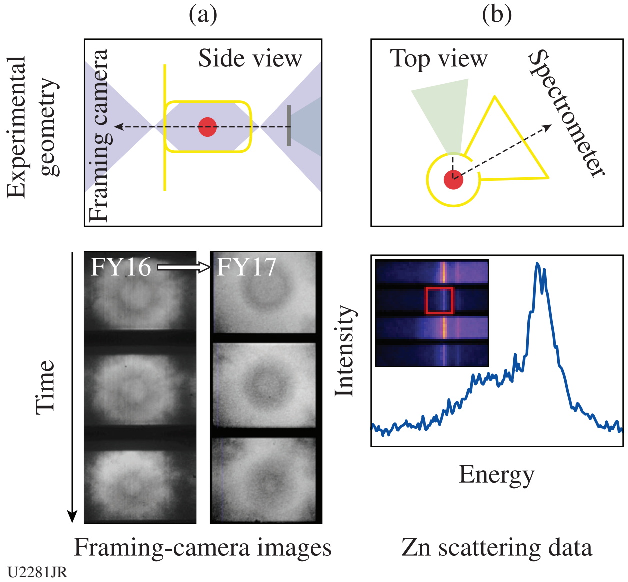

Figure 152.102
(a) Experimental geometry and representative 2-D framing-camera images of the imploding sphere, comparing results from FY16 and FY17 (shot 83557). (b) Geometry and representative Zn x-ray Thomson-scattering data (shot 85304).

The FY17 shots improved on prior measurements by increasing hohlraum gas fill to eliminate suspected hohlraum blowoff features and using faster-gating cameras to improve spatial resolution. Neutron diagnostics were also fielded to detect neutrons from the hot spot. The new design for the x-ray scattering measurement yielded a high-quality Compton feature and an elastic feature potentially artificially elevated because of Zn plasma leakage. These results, together with the FY16 measurements on CH_2, are being summarized for a publication that will describe the principal Hugoniot of plastic from the initial densities of CH, CH_2, and CD.

In addition, a separate half-day of shots continued development of a platform to achieve hundreds-of-Mbar pressures in a spherically converging shock wave, launched by using direct laser ablation of the sphere. This measurement probed deuterated plastic (CD) using radiography, x-ray Thomson scattering, and neutron yield. Data improved in quality compared to FY16 but indicated some drive asymmetry and preheating effects, requiring further design optimization.

Development of a Conically Convergent Platform for Hugoniot Equation-of-State Measurements in the 100-Mbar to 1-Gbar Pressure Regime

Principal Investigator: A. E. Lazicki
Co-investigators: D. Swift, F. Coppari, R. London, D. Erskine, D. E. Fratanduono, P. M. Celliers, J. H. Eggert, G. W. Collins, H. Whitley, J. Castor, and J. Nilsen

This campaign was designed to develop a platform for measuring Hugoniot EOS of arbitrary (including high-*Z*) materials at pressures much higher than can be achieved using a standard planar drive. This platform is intended to collect data in the pressure regime of 100+ Mbar, where currently very little data exist for any material, for the purpose of constraining EOS models.

To achieve the desired pressure amplification, converging shock waves are launched into a cone inset in a halfraum. For appropriate cone angles, nonlinear reflections of the shock wave result in the formation of a Mach stem: a planar high-pressure shock that propagates along the axis of the cone. This approach was tested in FY16 and produced promising results but suggested the need for preheat shielding. The FY17 half-day campaign attempted to overcome this need with Au preheat shield layers by experimenting with a porous cone material, from which simulations suggested that increased pressure amplification would be possible. Additionally, these shots tested multiple cone angles and fielded targets with quartz windows and Al steps to attempt to quantify the Mach wave's strength and steadiness. Two results are shown in Fig. 152.103. Transit time calculations indicate that 100+ Mbar shock waves were generated in the CH cones. At peak laser intensities the quartz windows blanked, indicating that the Au preheat shield thicknesses were not sufficient, and the profile of the shock breakout suggested the Mach wave was decaying (unsupported) through the full target thickness. A subset of the shots also attempted to use area-backlit radiography to image the Mach wave formation in the cones themselves, through slits in the halfraums. Geometric issues made it very difficult to interpret the framing-camera images. However, the lessons learned on this shot day were very important in designing a successful test shot on the NIF, completed on 31 August 2017.

(a) Al steps with Au preheat shield

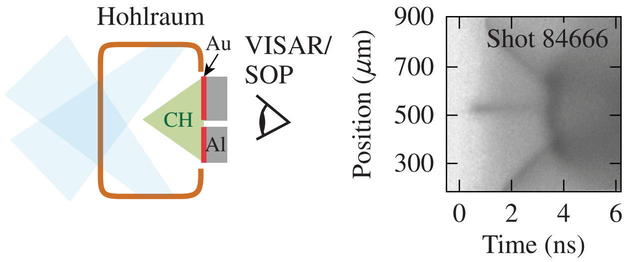

(b) Quartz flat with Au preheat shield

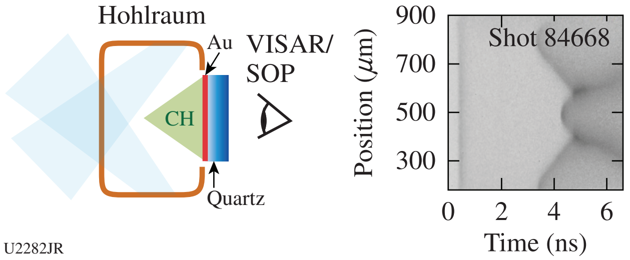

Figure 152.103
Experimental configuration and raw SOP data showing the breakout time from (a) a stepped Al sample with Au preheat shield layers and (b) a thick quartz sample with a Au preheat shield layer.

3. Material Dynamics and Strength

Copper Rayleigh–Taylor (CuRT) Growth Measurements

Principal Investigator: J. M. McNaney
Co-investigators: S. Prisbrey, H.-S. Park, C. M. Huntington, and C. E. Wehrenberg

The CuRT Campaign is part of the material strength effort, which is aimed at assessing the strength of various metals at high pressure and high strain rate. The goal of the CuRT platform is to measure Rayleigh–Taylor (RT) growth of samples that behave "classically," i.e., can be fully modeled using a fluid description. In this series of experiments the intent is to measure RT growth in liquid copper at high pressures. A second goal is to demonstrate the dynamic range of the technique by measuring RT growth in solid copper.

Without the stabilization of strength, classical RT growth is characterized by a growth rate $\gamma = \sqrt{kg\mathrm{A}_n}$, where k is the wavelength of the unstable mode, g is the acceleration, and the Atwood number A_n quantifies the magnitude of the density jump at the interface. Acceleration of the sample in the experiment is provided by the stagnation of a releasing shocked plastic "reservoir," which is directly driven by ~2 to 8 kJ of laser energy, depending on the desired material condition. The growth of preimposed ripples is recorded using transmission x-ray radiography of a copper He_α slit source, where the opacity of the sample is calibrated to the ripple amplitude. The preshot metrology and measured ρr of the driven sample together yield the growth factor, which is compared to models of RT growth. Diagnostic features such as a gold knife edge on the sample allow one to measure the modulation transfer function and create an opacity look-up table on each shot, resulting in error bars of approximately ±10%.

The March 2017 campaign produced the first results for liquid copper RT. Analysis of the velocimetry (Fig. 152.104) indicated that the copper RT samples were subjected to a shock of ≈5 Mbar, leading to a complete melt of the sample and subsequent RT growth in the liquid phase. The liquid Cu RT growth curve is presented in Fig. 152.105. A second day of liquid copper shots took place on 13 September 2017. The results of those experiments (also in Fig. 152.105) were consistent with the values obtained in the March data. Simulations of the liquid Cu growth are in progress.

Evaluation of Additively Manufactured Foams for Ramp-Compression Experiments

Principal Investigator: R. F. Smith

The FY17 "AMFoam" Campaigns continued to evaluate the use of 3-D–printed or additively manufactured foams as surrogates to carbonized resorcinol foams (CRF's) in ramp-compression target designs. The 3-D–printed foams may be characterized as follows: The $100 \times 100 \times 16\text{-}\mu\mathrm{m}^3$ log pile blocks, composed of individually printed lines, are stitched together to form 1.7-mm-diam layers. Seven $16\text{-}\mu\mathrm{m}^3$ layers are then stacked on top of one another to arrive at cylindrical AM foams that are 112 μm tall (Ref. 37). These foams are glued onto a 25 μm Br + 120 μm 12% Br/CH assembly

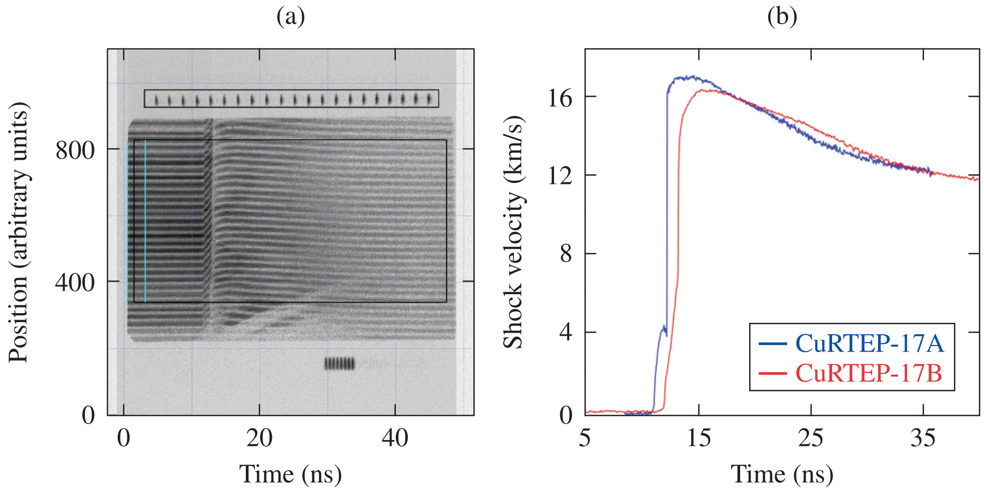

U2283JR

Figure 152.104
(a) The active shock breakout (ASBO) data from shot 26423 (September 2017); (b) analyzed results and comparison to March 2017 results.

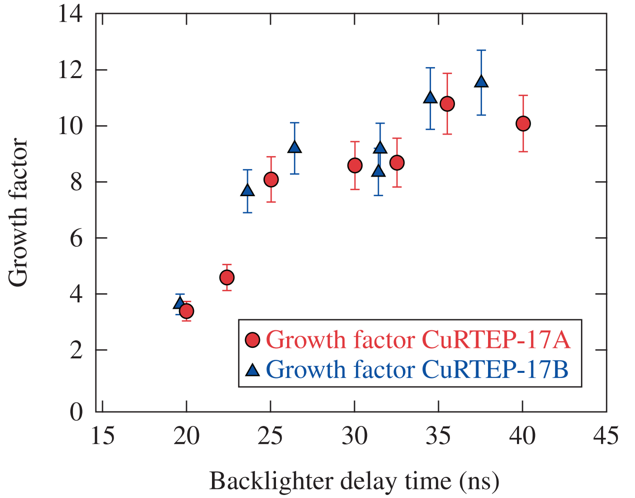

U2284JR

Figure 152.105
Growth factor data for liquid copper from the March and September shot days.

[Fig. 152.106(a)]. Following the ramp-compression design described in Ref. 30, 15 OMEGA beams with 300 J in 2 ns result in a ramp-compression wave being launched into a stepped-Al/LiF sample [Fig. 152.106(a)]. At a controlled time after this compression begins, the OHRV (2-D VISAR probe) takes a 2-D snapshot of the reflectivity and velocity field with a spatial resolution of ~3 μm (Ref. 38). An example of the intensity field recorded on the 2-D VISAR is shown in Fig. 152.106(c).

These campaigns have varied the structure of the 3-D–printed foam with the goal of optimizing the temporal ramp profile. These experiments have been conducted in support of material strength experiments on the NIF.

4. National Security Applications

SolarCellESD: Solar Cell Electrostatic Discharge Experiments

Principal Investigator: K. Widmann
Co-investigators: P. Jenkins (NRL); S. Seiler (DTRA); and P. Poole and B. Blue (LLNL)

The overall goal of the SolarCellESD Campaign is to determine experimentally whether prompt x rays can induce failure modes in solar arrays that are not accounted for by simply testing the individual solar cells alone. The solar-cell array is fielded as part of the x-ray Langmuir probe detector (XLPD) cassettes and exposed to x rays from a laser-driven source. The FY17 campaigns added a partial electromagnetic-interference enclosure of the XLPD front end—"partial" because the enclosure has a large rectangular opening providing an unobstructed view of the x-ray source for the solar-cell array. The bias and diagnostic electronics for the solar cells were also improved such that the bias circuit is fully isolated from any of the target chamber components and the bias voltage can be changed manually between shots. This bias voltage allows one to mimic the voltage difference between two adjacent solar cells from different strings in large arrays, which can range from tens to a few hundred volts. Figure 152.107 shows a schematic and a photo of the new and improved XLPD front end.

The FY17 campaign continued using the x-ray source developed in FY15: a small gold halfraum (600-μm diameter, 600-μm long) with a small pinhole (60-μm or 100-μm diameter) at the "closed" side of the halfraum. The targets were driven with three sets of 1-ns laser pulses to generate x-ray pulses of 3-ns duration. These targets provide two significantly different

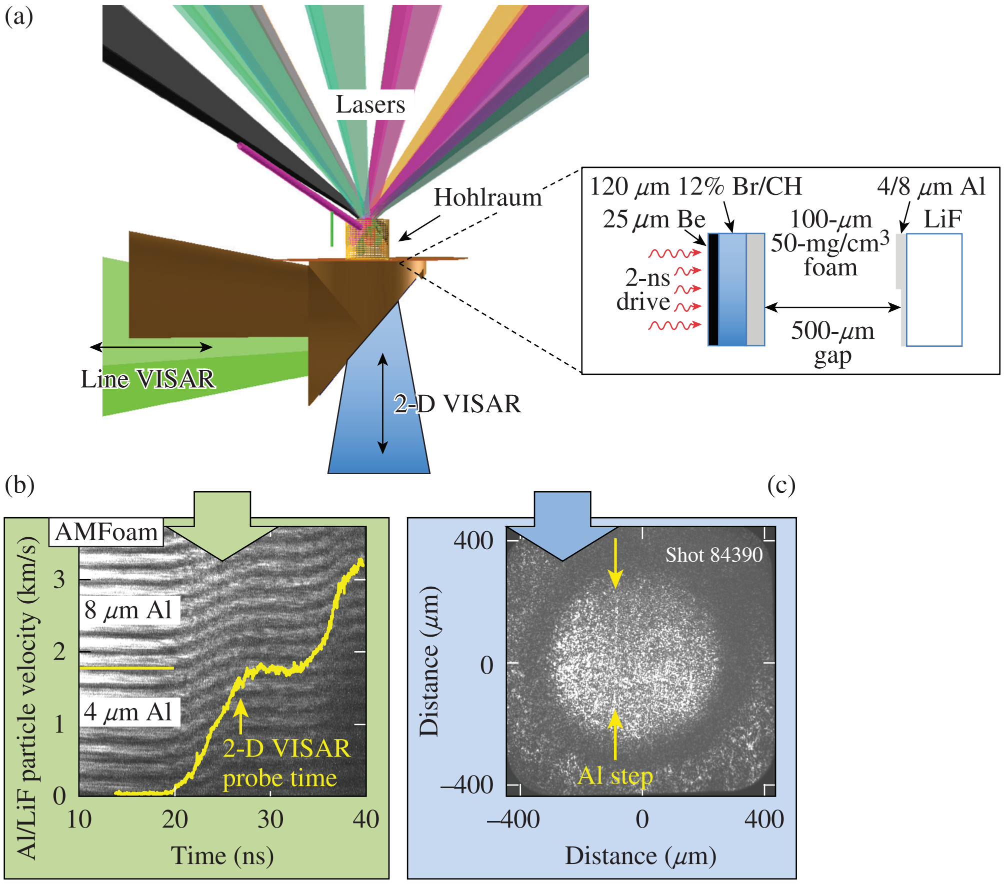

Figure 152.106
(a) Schematic diagram describing the experimental setup for the AMFoam-17A Campaign, which combined the ASBO and OHRV (2-D VISAR) diagnostics on a single shot. The goal of these shots was to characterize the temporal and spatial drive associated with additively manufactured (3-D–printed) foam targets. The line VISAR shows the 1-D velocity measure as a function of time. Two-dimensional VISAR provides the 2-D velocity measurement of 3-D–printed foams at a snapshot in time. (b) The ASBO record shows a characteristic ramp/pressure-hold/ramp compression profile. (c) Sample reflectivity at OHRV probe time. For the AMFoam-17B Campaigns, only the ASBO (VISAR) diagnostic was used. Preliminary 2-D VISAR non-fringes image and velocity analysis shows AMFoam exhibits a spatial structure comparable or perhaps smoother than CRF foam.

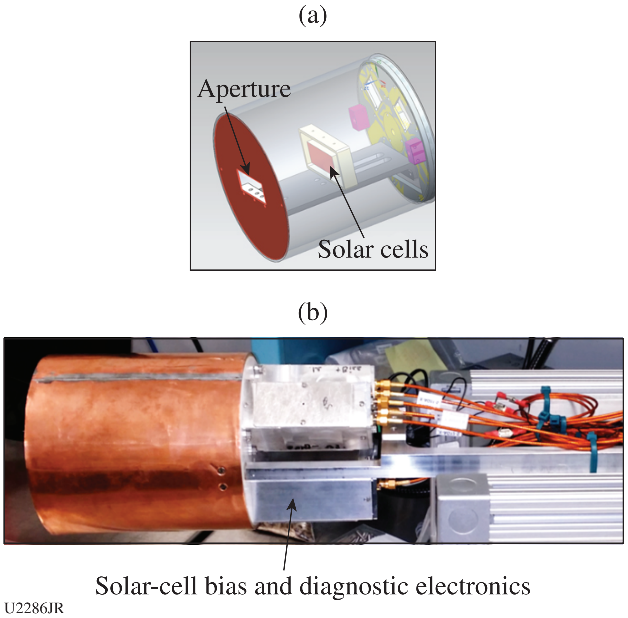

Figure 152.107
(a) Front end of the x-ray Langmuir probe detector (XLPD) with the solar cell (mini) array, i.e., 2 × 1 cells and (b) photo of the XLPD (side-on view) with the new electromagnetic-interference enclosure and the various bias and diagnostic electronics.

x-ray flux (and fluence) levels depending on the target orientation with respect to the solar cell array ("open side" versus "pinhole side"). Despite the large difference in the measured radiant x-ray power, from 300-GW/sr peak flux for the open side down to a few tens of GW/sr for the pinhole side, the spectral intensity distribution should be very similar. Unfortunately, the low signal level on the Dante x-ray diodes for the low-flux case did not allow us to make a good quantitative comparison of the unfolded spectral intensities. Figure 152.108 shows the x-ray flux measured with Dante for two open-side shots.

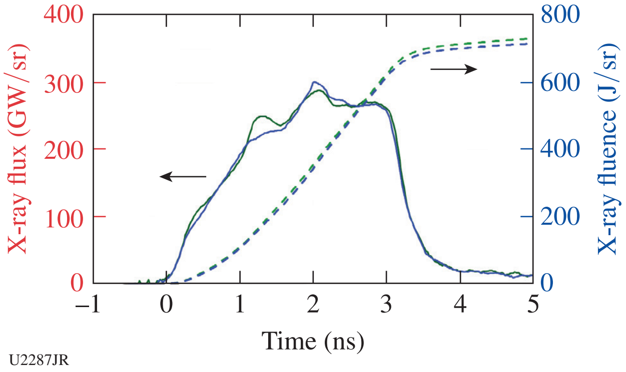

Figure 152.108
Dante measurements of the output (radiant power and x-ray fluence) of the laser-driven x-ray sources for two shots in the "open side" configurations (see text for details) showing a shot-to-shot variation of only 2% in the total x-ray fluence, within the uncertainty of the Dante x-ray flux measurement.

With the improved hardware, it was possible to generate and observe, for the first time, x-ray–induced arcing just between the solar cells without creating discharge between the solar cells and any of the other components in the target chamber. These shots also demonstrated the feasibility of mitigating the x-ray–induced arcing by altering the bias voltage for the solar-cell array. The next goal for the this campaign is a detailed parameter scan to determine the threshold values for the x-ray fluence and associated bias voltage levels, respectively, for x-ray–induced arcing in solar-cell arrays.

Plasma Instability Control to Generate a High-Energy Bremsstrahlung X-Ray Source

Principal Investigator: P. L. Poole
Co-investigators: R. Kirkwood, S. C. Wilks, M. May,
K. Widmann, and B. E. Blue

In FY17 a campaign began to develop a high-fluence x-ray source in the 30- to 100-keV range by deliberately stimulating and optimizing plasma instabilities. High-fluence sources at lower energies are currently used for materials effects studies in extreme environments, but stronger sources are needed for >30-keV x rays. This project aims to enhance laser conversion to plasma instabilities such as stimulated Raman scattering (SRS), which accelerate electrons in plasma waves that will convert to high-energy x rays via bremsstrahlung in the high-Z hohlraum wall.

The SRS-Xray-17A half-day centered on optimizing plasma conditions within a hohlraum for high SRS gain by reversing ideas on how to mitigate these effects for fusion conditions (SSD bandwidth off, phase plate changes, etc.). Two types of targets were fielded to test SRS generation: one with 6-mg/cm^3 (0.2 n_c) SiO$_2$ foam fill, the other with 10 μm of parylene-N (CH) inner lining. The CH-lined hohlraums were illuminated with an 80-ps picket prepulse arriving a variable time before the main 1-ns, 450-J/beam laser drive.

Primary results were promising: the best targets exhibited *10× more x-ray yield in the >50-keV regime than typically seen on direct-drive shots*. The SRS streak data are being compared to the various x-ray diagnostics fielded to obtain a detailed picture of instability gain and directionality and its impact on x-ray fluence. While the CH prepulsed targets exhibited factors-of-6 more direct SRS backscatter than the no-prepulse CH and foam targets, these latter configurations had the best x-ray yield (Fig. 152.109). The increased indirect backscatter on the no-prepulse CH target provides an avenue of further simulation and future experimental study to investigate the directionality of SRS backscatter within the hohlraum and its impact on the ultimate x-ray yield. Target design simulations are underway, using these valuable experimental results to plan the FY18 OMEGA and NIF campaigns. These promising initial results are a valuable stepping stone toward a new x-ray source that will represent a large capability increase for national security applications and related materials under extreme conditions studies, with the additional benefit of broadening the understanding of plasma instability control for fusion and other applications.

5. Plasma Properties

Investigation of Orthogonal Plasma Flows in the Presence of Background Magnetic Fields

Principal Investigator: B. B. Pollock
Co-investigators: T. Johnson, G. F. Swadling, J.S. Ross,
and H.-S. Park

The DebrisPlasma-17A shots continued the Magnetized Collisionless Shock–Weapons Effect Campaign from previous

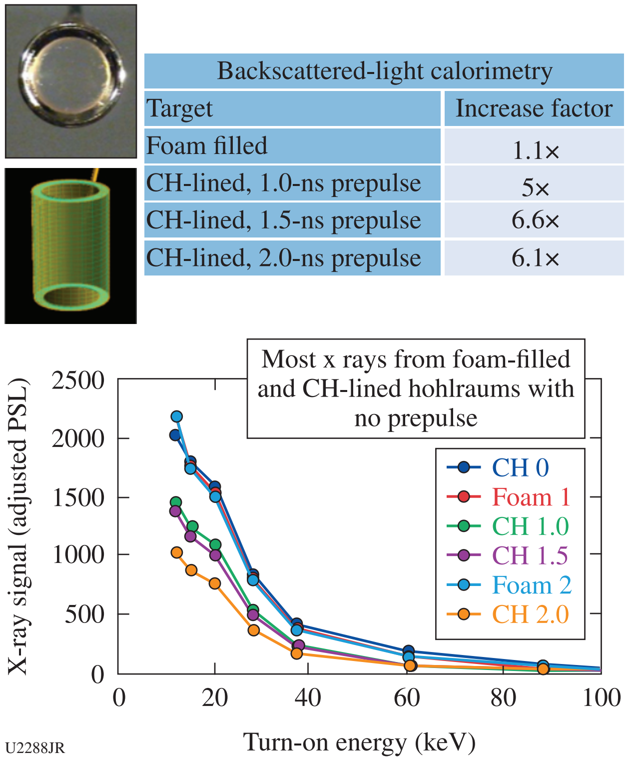

Backscattered-light calorimetry	
Target	Increase factor
Foam filled	1.1×
CH-lined, 1.0-ns prepulse	5×
CH-lined, 1.5-ns prepulse	6.6×
CH-lined, 2.0-ns prepulse	6.1×

Figure 152.109
Data summary for SRS-Xray-17: highest SRS backscatter from CH-lined hohlraums irradiated with prepulse; highest x-ray yield from no-prepulse CH and foam-filled targets. PSL: photostimulated luminescence.

years. The goal for this series of experiments is to quantify the interaction of orthogonal plasma flows, with and without a background magnetic field. The field is supplied by LLE's magneto-inertial fusion electrical discharge system (MIFEDS), which delivers 4 to 8 T at the interaction region of the experiments, depending upon the specific geometry of the MIFEDS coils (Fig. 152.110). The orthogonal plasma flows originate from two separate foil targets, one of which is mounted to the MIFEDS structure. The foil material composition, laser drive, spacing, and time of flight to the interaction region can be varied on each shot.

The interaction region of the two flows is simultaneously probed with 2ω Thomson scattering and protons from the implosion of a D^3He-filled capsule. Initial measurements of the electron density and temperature from the Thomson scattering do not indicate a strong dependence on the strength or direction of the background magnetic field. The proton deflectometry data do show structural differences in the measured proton distribution with and without the field, but further modeling and simulations are needed to quantify these differences.

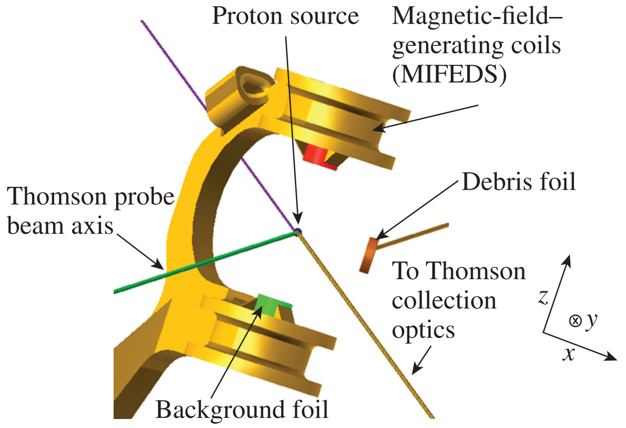

Figure 152.110
Experimental configuration viewed from the proton detector in TIM-1. One or two foils can be mounted to the MIFEDS structure, which is centered at target chamber center (TCC). The Thomson-scattering geometry is k matched to the z axis of the experiment. The capsule is 1 cm into the plane of the page from TCC and the debris foil is 2 mm from TCC.

Measurement of Gold Thermal Transport and M-Shell Emission Using a Buried Layer Platform

Principal Investigator: E. V. Marley
Co-investigators: L. C. Jarrott, M. B. Schneider, G. E. Kemp, M. E. Foord, R. F. Heeter, D. A. Liedahl, K. Widmann, C. W. Mauche, G. V. Brown, and J. A. Emig

This campaign was designed to measure the thermal transport through gold layers as well the emitted M-shell gold spectra from a well-characterized and uniform plasma for comparison to atomic kinetic models. The buried layer target geometry used for this experiment is capable of generating plasmas with an electron temperature of ~2 keV at electron densities of 10^{21} electrons per cubic centimeter. These are within the range of conditions found inside gold hohlraums used on experiments on the NIF, providing a stable laboratory setting for radiation transport and atomic kinetic studies of hohlraum plasmas.

Planar, buried layer targets composed of Ti, Mn, and Au were illuminated evenly on both sides (Fig. 152.111) to heat the sample. The sample was buried between two 5-μm-thick layers of Be serving as an inertial tamp to slow the expansion of the sample. Time-resolved 2-D images of the target's x-ray emission, viewed both face-on and side-on, were recorded using time-gated pinhole cameras. The K-shell spectra from the Ti and Mn were used to determine the electron temperature of the plasma. The time-resolved spectra were recorded using a

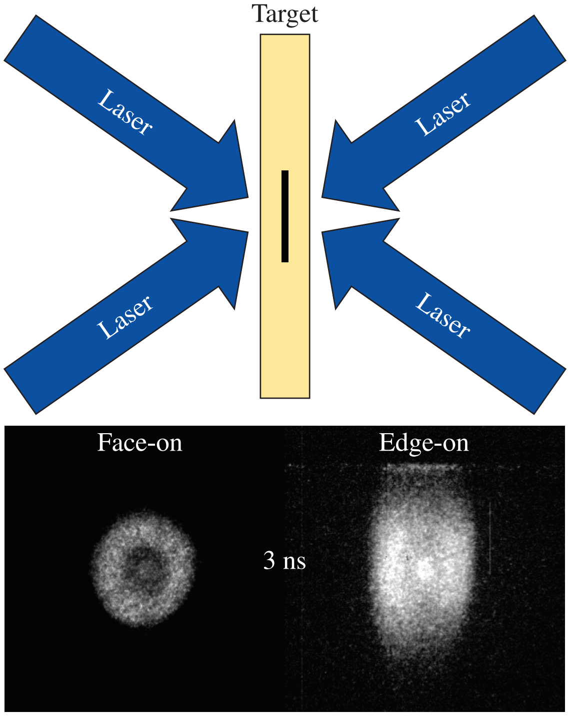

U2290JR

Figure 152.111
Experimental configuration and pinhole images of the emission area at 3 ns of shot 86860.

crystal spectrometer coupled to a framing camera, as well as a crystal spectrometer coupled to an x-ray streak camera. Two additional time-resolved crystal spectrometers were used to record the full range of the Au M-shell emission. All of the framing cameras used, for imaging as well as spectroscopy, were co-timed so the plasma conditions at the time of the measured Au M-shell emission could be established from synchronous K-shell and imaging data.

During the campaign two different sample thicknesses were used to measure the thermal transport through Au. Two different pulse shapes were also used to assess which was most efficient for coupling laser energy into the buried layer target. A complete set of data from all six precisely co-timed diagnostics was recorded for both target types, using both pulse shapes during this August campaign, at temperatures ~2 keV. Data analysis is underway.

6. Hydrodynamics

Experiments on the Rayleigh–Taylor Instability in the Highly Nonlinear Regime

Principal Investigators: C. C. Kuranz (University of Michigan) and C. M. Huntington (LLNL)

Co-investigators: L. Elgin, G. Malamud, S. R. Klein, R. P. Drake, and D. Shvarts (University of Michigan) and T. Handy and M. R. Trantham (LLNL)

These experiments observe the evolution of the single-mode Rayleigh–Taylor instability (RTI) in low- and high-Atwood-number regimes at late scaled times (Fig. 152.112). Models predict two growth phases of the RTI: exponential growth, followed by a nonlinear stage reaching a terminal velocity.[39] For low-Atwood number systems, numerical simulations show an additional growth phase in the late nonlinear stage, characterized by reacceleration.[40] There are, however, claims that this reacceleration may be an artifact of the simulations and may not reflect the evolution of classical RTI. Prior experimental studies of RTI growth have not created the conditions necessary to observe the late nonlinear stage, which requires large aspect ratios of the spike and bubble amplitudes to the perturbation wavelength $\left(1 \le h_{\mathrm{s,b}} / \lambda \le 3\right)$ (Ref. 40).

The first two experiments in this new campaign were conducted in FY17. A laser-driven blast wave accelerates an RT-unstable interface in a shock tube. X-ray radiographs along dual orthogonal axes capture the evolution of RTI. Late scaled times are achieved with small-wavelength ($\lambda = 40$-μm) seed perturbations at the interface. PAI (polyamide-imide) plastic (1.4 g/cm^3) is used as the heavy fluid. The lighter fluid consists of CRF, with pre-shock densities of 0.05 g/cm^3 (high Atwood) or 0.4 g/cm^3 (low Atwood). The first shot day demonstrated x-ray–backlit imaging capable of resolving

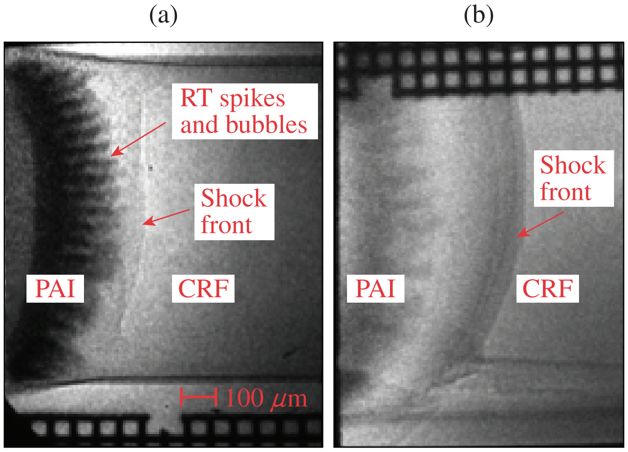

U2291JR

Figure 152.112
(a) RID 83095 (10/06/16) with high-Atwood, $\lambda = 40$-μm target at 15 ns and (b) RID 85111 (4/06/2017) with low-Atwood, "flat" interface target at 26 ns. PAI: polyamide-imide; CRF: carbon resorcinol formaldehyde.

the small-wavelength RT spikes and bubbles. But the plastic shock tube could not support the higher internal pressure of the dense, low-Atwood targets. A new target design was developed and fielded for the second shot day. Improvements included Be walls, which can be thicker because of the high x-ray transmission of Be, and a larger tube diameter, which delays the effects of transverse waves. The new design extended the time scale for observations of RTI growth in low-Atwood targets from 30 ns to >40 ns. However, the ablators did not meet specifications, compromising the physics of the experiment. The data are being analyzed to extract as much information as possible, and the team is working with the ablator manufacturer to ensure that the parts for the FY18 experiments meet all specifications.

This work is funded by LLNL under subcontract B614207.

Proton Heating of Copper Foam on OMEGA EP

Principal Investigator: J. Benstead

Co-investigators: E. Gumbrell, S. McAlpin, M. Crook-Rubery, R. Merritt, and W. Garbett (AWE)

This LLNL–AWE campaign studies the heating of a cylindrical puck of copper foam irradiated by a short-pulse–generated proton beam. This shot day was an extension of previous shot days in 2014 and 2016 and featured a refined target and diagnostic design. The two major aims of the experiment were to measure the temperature distribution through the target and to quantify the extent of expansion of the rear surface.

The experimental setup is shown in Fig. 152.113. A gold foil was irradiated with the OMEGA EP sidelighter (SL) beam delivering 200 J over 3 ps. The SL produced a beam of protons and ions that were used to heat a copper-foam puck positioned 0.5 mm away. An aluminum foil was placed between the gold foil and the copper puck to improve heating by filtering out heavier ions and low-energy protons, which nonuniformly heat the target. The subsequent sample expansion was imaged with an x-ray radiography system. This used a nickel area backlighter, irradiated with three long-pulse beams, coupled to an x-ray framing camera (XRFC) that imaged the backlit target. The backlighter (BL) beams were delayed with respect to the SL beam in order to observe the heated and expanded target at different times. The streaked optical pyrometry (SOP) diagnostic was fielded orthogonally to the heating axis with its imaging slit oriented such that the temperature through the central section of the disk could be measured front to rear over the first 5 ns of heating (see Fig. 152.114); an RCF stack measured the proton/ion beam spectrum on each shot (see Fig. 152.115).

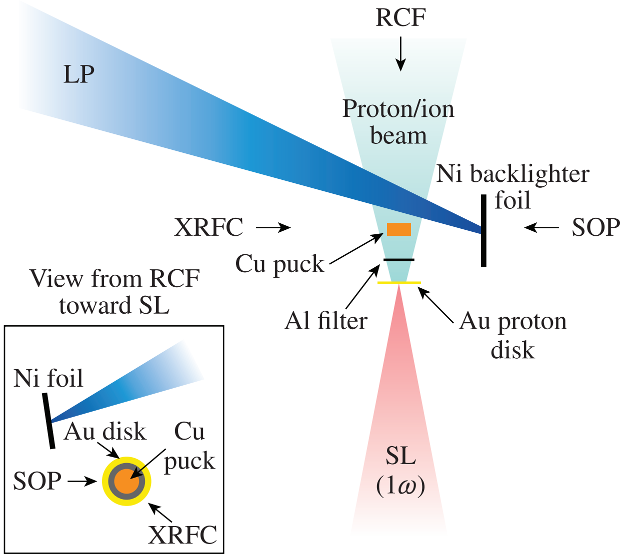

U2292JR

Figure 152.113
Experimental layout for proton-heating shots with combined x-ray radiography, SOP, and RCF. Only one long-pulse beam (of the three used) is shown for simplicity.

In total, seven shots were fired with data acquired on the XRFC, RCF, and SOP diagnostics. Full data analysis is still in progress, but preliminary results indicate that the degree of heating achieved was as desired. Slightly unusual features present on the SOP data have been attributed to the reduced target size relative to previous shot days, causing unexpected interactions with the SL pulse.

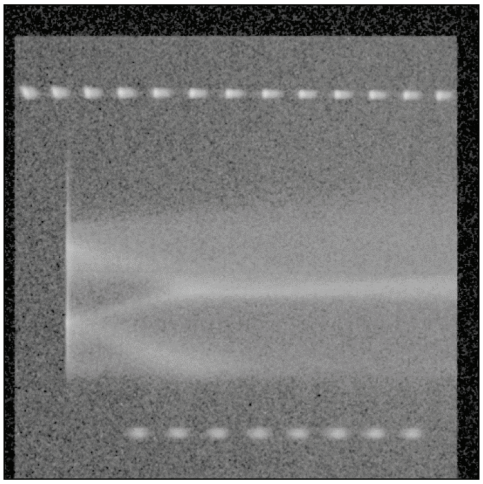

U2293JR

Figure 152.114
SOP data from a proton-heating shot. The proton field is directed from the top downward, and the 1-D spatial image is taken through the center of the puck. The anomalous features observed appear to be caused by the reduced target dimensions causing more-complicated interactions with the beam and proton field relative to previous shot days in this campaign.

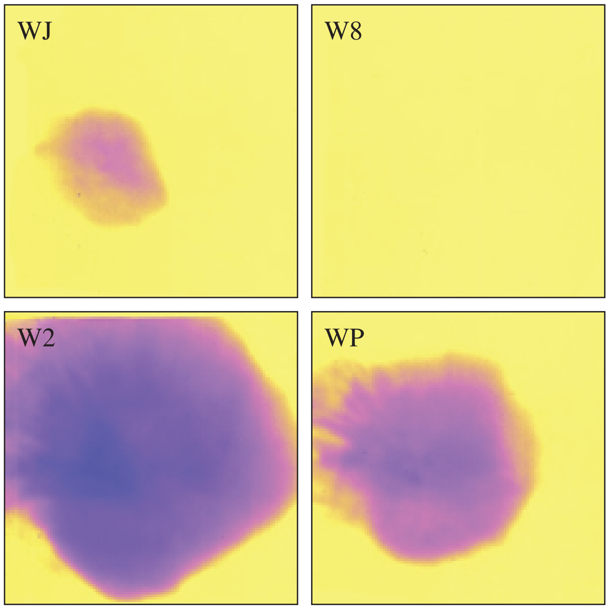

Figure 152.115
RCF data showing the attenuation of the proton and ion fields on one shot in the final four pieces of the film stack. The film pieces move progressively farther away from the target beginning at the bottom left image, then bottom right, then top left, and finally top right.

Development of Radiography-and-VISAR Platform for Hydrodynamics Measurements

Principal Investigators: M. Rubery (AWE) and D. A. Martinez (LLNL)
Co-investigators: G. Glendinning (LLNL); and S. McAlpin, J. Benstead, and W. Garbett (AWE)

As part of the LLNL/AWE Carisbrook Campaign, one and a half shot days of experiments were performed on the OMEGA Laser System during FY17. The platform consists of a halfraum and shock tube package driven by 15 × 500-J beams from the OMEGA H7 axis [Fig. 152.116(a)]. The objectives for these shot days were to diagnose the evolution of a hohlraum-driven interface using simultaneous point-projection x-ray radiography and VISAR, a configuration that was successfully demonstrated during FY16. A secondary objective for FY17 was to demonstrate the use of a reduced-mass backlighter [3-mm Ta disk versus 4-mm Ta square, Fig. 152.116(b)]. If successful, the new configuration should sufficiently reduce the amount of vaporized metal generated during the experiment to allow future campaigns to use the OMEGA EP short-pulse beam with debris shields removed (higher energy).

To generate the 7.8-keV He$_\alpha$ point-projection x-ray source, a 600-μm-sq nickel microdot was driven to 2×10^{15} W/cm^2 using 4 × 400-J, 1-ns backlighter beams [Fig. 152.116(b)]. The x-ray emission is projected through a 20-μm Ta pinhole plate aligned along the shock tube and toward the TIM-6 cranked snout axis of $\theta = 123.1$ and $\phi = 172.76$. Images were recorded on film using a gated XRFC.

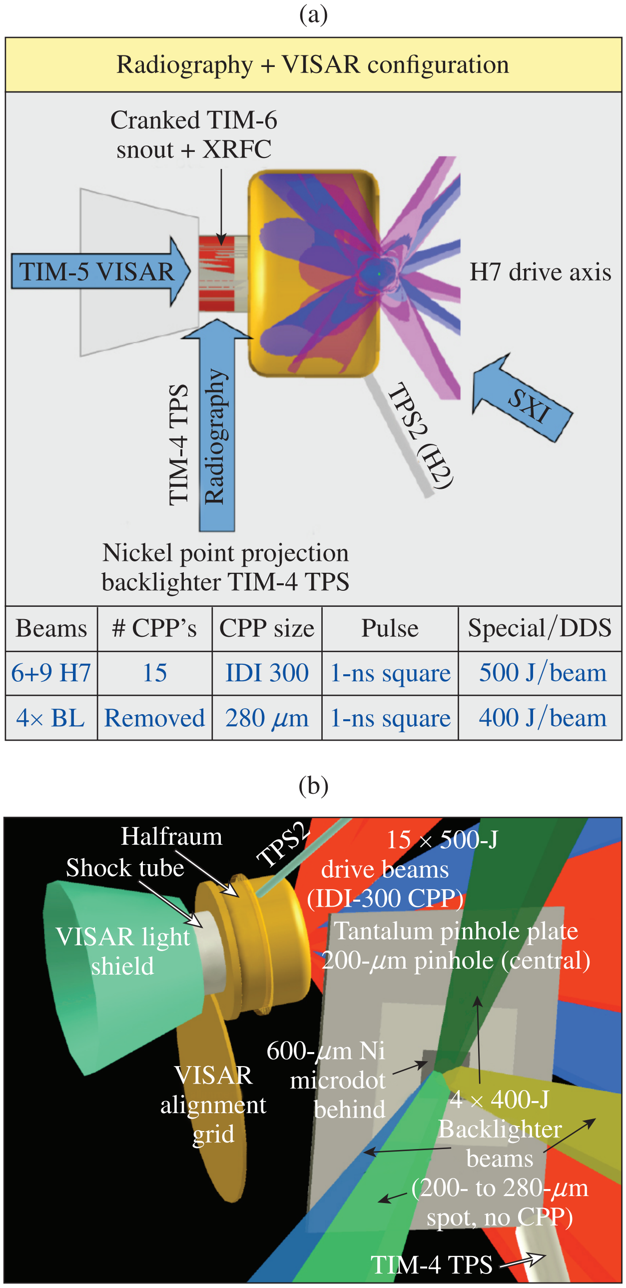

Beams	# CPP's	CPP size	Pulse	Special/DDS
6+9 H7	15	IDI 300	1-ns square	500 J/beam
4× BL	Removed	280 μm	1-ns square	400 J/beam

Figure 152.116
(a) Radiography + VISAR configuration overview and (b) VISRAD isometric view of the experiment. TPS: target positioner system.

A quartz window, aluminum flash coating, and light shield cone were added to the rear of the target, allowing us to make VISAR measurements along the TIM-5 H14 axis.

The VISAR diagnostic performed well during all shots from Ca-17A and 17B. Figure 152.117 shows good-quality streak-camera images from both legs of the VISAR diagnostic on shot 86473. The SOP diagnostic, which uses the same optical relay as the VISAR, also produced good quality data on both shot days.

Unfortunately, during the first shot day, no radiography images were recorded. The source of this failure was found to be in the assembly of the backlighter. The mounting location of the nickel microdot was measured >100 μm away from the design position; this deviation is sufficiently large to move the nickel x-ray emission out of the XRFC field of view. In response to this, the backlighter design was modified to reduce sensitivity to assembly and target misalignment. The microdot was increased from 400 μm square to 600 μm square, and the backlighter beam spots increased from 200-μm to 280-μm diameter. The backlighter energy was also increased from 200 J/beam to 400 J/beam to maintain intensity. On the second half-day of shots these modifications were found to be 100% successful.

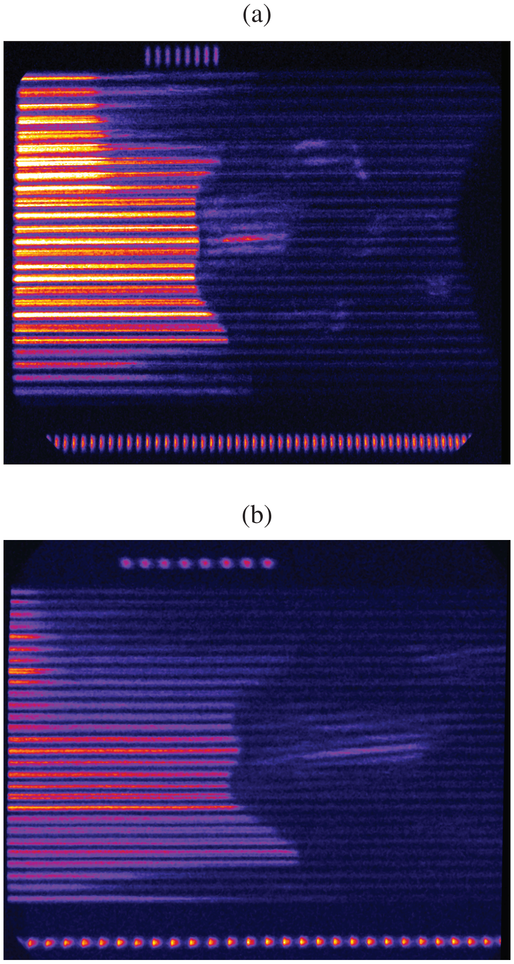

Figure 152.117
VISAR streaked images from OMEGA shot 86473, Ca-17B.

In addition, the new reduced-mass backlighter was successfully fielded on the second day and produced a radiograph with no observable drop in image quality, opening up the possibility of a future joint shot day, without the limitations on pulse energy introduced by parabola debris shields.

Development of Gamma-Ray Sources for MeV Radiography

Principal Investigator: F. Albert
Co-investigators: N. Lemos and J. Shaw (LLE); and D. A. Martinez and V. A. Smalyuk (LLNL)

This series of shots was designed to develop gamma-ray sources intended for a future MeV radiography capability on NIF's Advanced Radiography Capability (ARC) short-pulse laser. Megavolt radiography on the NIF will serve a number of applications, such as double-shell implosions and imaging of dense objects.

The first FY17 campaign alternatively focused the backlighter and sidelighter short pulses (10 ps, 900 J) onto tantalum targets coated with 10 μm of plastic to produce hot electrons and subsequent gamma-ray emission from bremsstrahlung radiation (Fig. 152.118). The electron spectrum was measured with an electron positron proton spectrometer (EPPS) (along the short-pulse laser axis and also at 90°), and the gamma-ray spectrum with HERIE (a high-energy radiography imager) using a tantalum step-wedge filter pack. This diagnostic was used to retrieve an emitted photon spectrum of the form $f(E) = A\exp(E/E_T)$, where E_T is the spectrum temperature, comprised between 0.5 and 1 MeV for this experiment. About 10^{12} to 10^{13} photons/eV/steradian were detected with this process. Targets included both 1-mm-thick, 1-mm-diam, as well as 500-μm-thick, 25-μm-diam, tantalum pucks. The source size was measured by imaging an 800-μm-diam tungsten sphere onto HERIE and was found to be around a few 100 μm for the thick targets. Further shots are required to determine the effect of the target geometry on the source size.

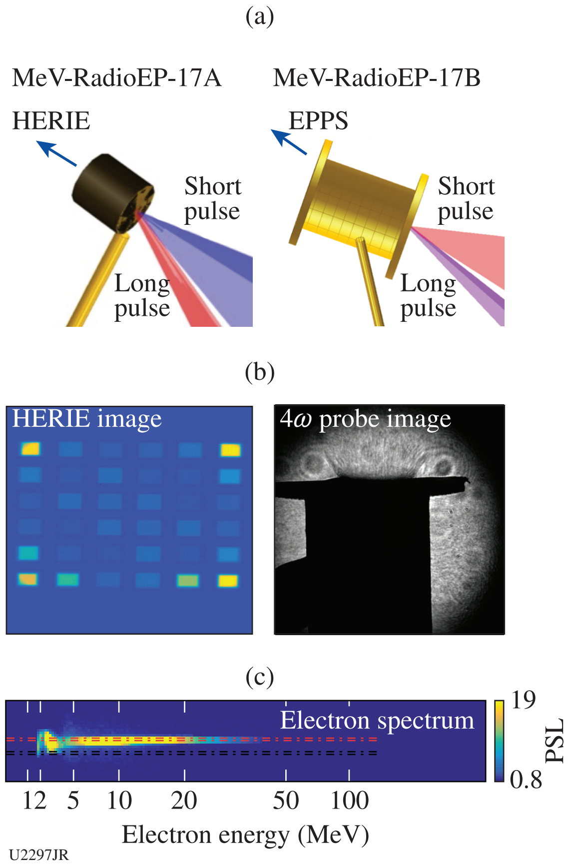

Figure 152.118
(a) Experimental configurations for the two shot days, (b) HERIE diagnostic image for MeV-RadioEP-17A and 4ω probe image, and (c) measured electron spectrum for MeV-RadioEP-17B.

The second campaign (MeV-Radio-EP-17B) aimed to look at an alternative electron production scheme (laser-wakefield acceleration in underdense plasmas) for future development of MeV photon sources on ARC. During this shot day, the 3- to 10-ps OMEGA EP short-pulse beams (alternately sidelighter and backlighter) were focused at intensities ~10^{18} W/cm^2 onto a 3-mm plastic gas tube filled with helium at atmospheric pressure. The gas tube was closed with 1-μm-thick mylar windows, which were blown down using an OMEGA EP long-pulse beam timed 5 to 10 ns before the short pulse. Plasma density at the entrance of the gas tube was monitored with the 4ω probe diagnostic. The main diagnostic, EPPS, measured accelerated electron energies up to 50 MeV.

Analysis of these campaigns is ongoing, and the results of the two shot days will be used to design efficient gamma-ray sources for LLNL programs.

Measurements of Instability Growth and Shell Trajectory Relevant to NIF Double-Shell Designs

Principal Investigator: Y. Ping
Co-investigators: V. A. Smalyuk, P. A. Amendt, R. Tipton, J. Pino, O. L. Landen, F. Graziani

The goal of this campaign is to measure instability growth rate and shell trajectory in planar geometry under conditions relevant to the double-shell design on the NIF. The target is a halfraum with an attached physics package consisting of an ablator, CRF foam, and a Cu inner shell. For the instability growth measurements, ripples with 30-μm and 60-μm periods and 0.5-μm amplitude were imprinted on the Cu inner surface, and face-on gated x-ray radiography was employed to measure the ripple growth over time. For the shell-trajectory measurements, side-on x-ray radiography with a streak camera was employed. The shot day was very successful with excellent data in both configurations, as shown in Fig. 152.119. Data analysis shows reasonable agreement with simulations on the ripple growth, yet the observed preheat of the Cu shell was underpredicted in the modeling. These results are being organized for publications and will also be used for target designs in FY18.

ACKNOWLEDGMENT

This work was performed under the auspices of the U.S. Department of Energy by Lawrence Livermore National Laboratory under contract DE-AC52-07NA27344.

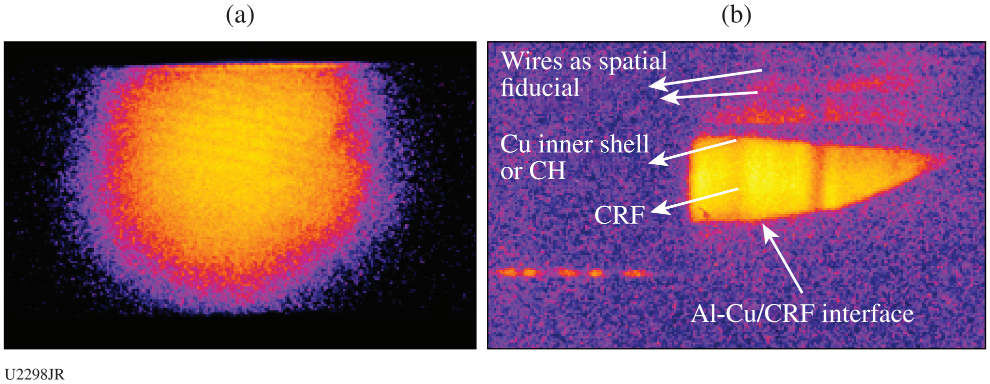

Figure 152.119
(a) A typical x-ray radiograph of ripple growth and (b) streaked x-ray radiograph of the shell trajectory.

FY17 LANL Report on Omega Facility Experiments

In FY17, Los Alamos National Laboratory carried out 17 shot days on the OMEGA and OMEGA EP Laser Systems in the areas of high-energy-density (HED) science and inertial confinement fusion (ICF). In HED our focus areas were on radiation flow, hydrodynamic turbulent mix and burn, warm-dense-matter equations of state, and coupled Kelvin–Helmholtz (KH)/Richtmyer–Meshkov (RM) instability growth. For ICF our campaigns focused on the Priority Research Directions (PRD's) of implosion phase mix and stagnation and burn, specifically as they pertain to laser direct drive (LDD). We also had several shot days focused on transport properties in the kinetic regime. We continue to develop advanced diagnostics such as neutron imaging, gamma reaction history, and gas Cherenkov detectors. The following reports summarize our campaigns, their motivation, and our main results from this year.

BeBoron

Shots were taken to measure the ablation rate of polyethylene to be evaluated for use as an ablator material for imploding capsules. Polyethylene was used at the last minute to replace Be:B flats that did not survive transportation, nor polishing. Polyethylene thin flats positioned at the end of the half-hohlraum and driven by the hohlraum radiation were used. This technique is similar to that used previously.[41,42] The shock breakout data gave us good measurements at 175 and 204 eV, with an ablation rate between 3 to 4 mg/cm^2/ns (Fig. 152.120).

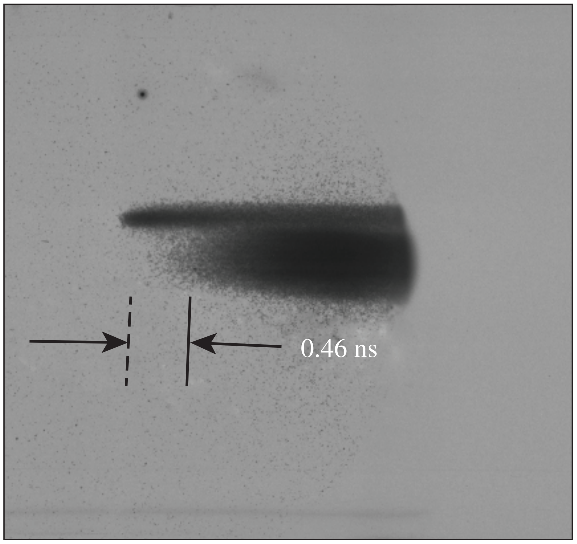

U2197JR

Figure 152.120
Shock breakout data from shot 84428.

Because of the poor reflectivity of the targets, only three shots gave data. Shot 84428 at 100-eV drive gave good VISAR data with a velocity reaching 30 km/s, with the data being consistent with a reflecting shock in the quartz (Figs. 152.121 and 152.122).

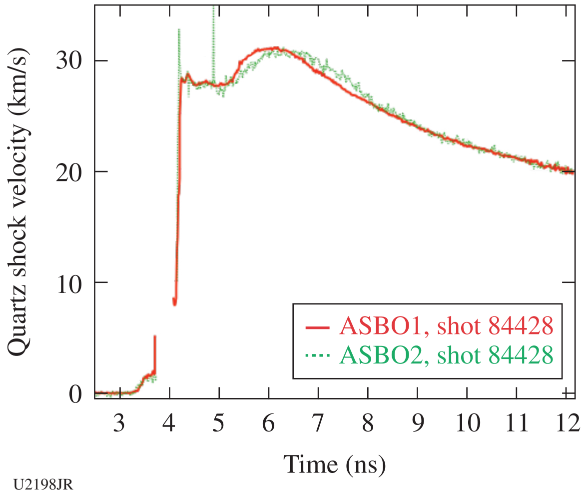

U2198JR

Figure 152.121
Analyzed VISAR data from shot 84428.

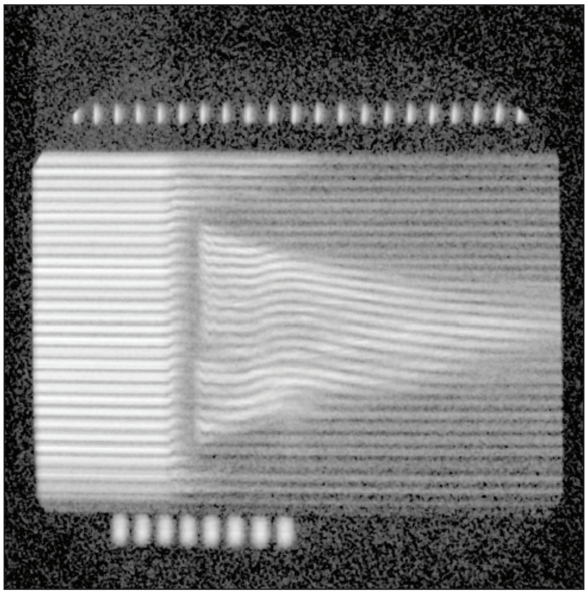

U2199JR

Figure 152.122
VISAR data from shot 84428.

COAX

The goal for COAX in FY17 was to complete platform development to prepare the way for addressing radiation-transport physics questions in supersonic → subsonic fronts on OMEGA and the NIF. To accomplish this, COAX had three shot days in FY17. This platform uses a halfraum to launch a radiation front down a cylindrical target featuring a doped aerogel foam coaxially contained in an undoped aerogel and a Be sleeve. This target is point-projection backlit by a V foil and pinhole target to radiograph the density spike that occurs when the radiation front cools and hydrodynamic expansion exceeds the rate of radiation flow. A 600-μm CH capsule with 1.5-atm Kr fill is used to backlight the target earlier in time to collect the temperature of the supersonic front from the ionization balance of dopant revealed through K-shell absorption spectroscopy of 1*s*–2*p* and 1*s*–3*p* Ti or Sc. Dante is used to measure the halfraum temperature through the laser entrance hole (LEH). As the impedance offered by the foam to the radiation front is increased, the slope of the front increases. This provides a window into radiation-transport physics in the supersonic to subsonic regime, which is important for astrophysical objects such as supernovae.

In November 2016, COAX collected useful radiography data of the subsonic front. The spectroscopic backlighter still needed development work to achieve high-resolution Ti and Sc K-shell spectra. We tested a method for evaluating the temperature sensitivity of the platform: putting an 8-μm-thick Cu ring or "top hat" around the lower half of the doped foam. In Fig. 152.123 we observed the difference between two shots in which the doped foam's density was equivalent, but one target contained a top hat and the other did not. A simple examination of the data was shown at the 2016 APS DPP Meeting (Fig. 152.124).

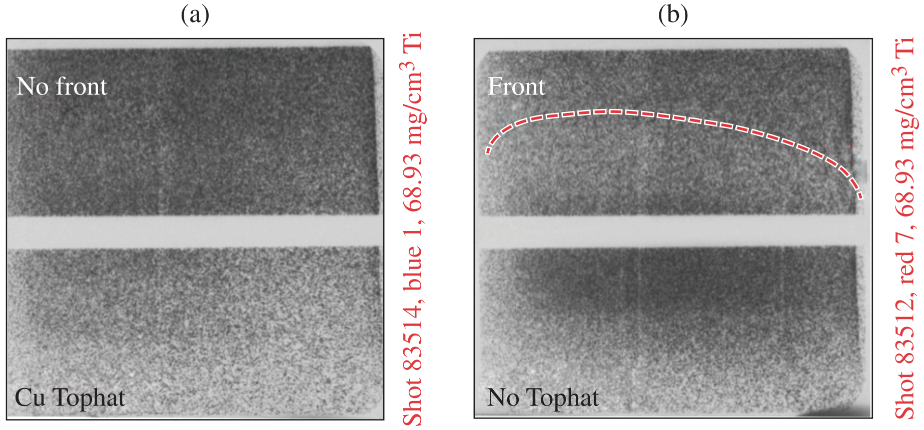

Figure 152.123
Comparison of COAX radiography from targets (a) with and (b) without the copper "top hat."

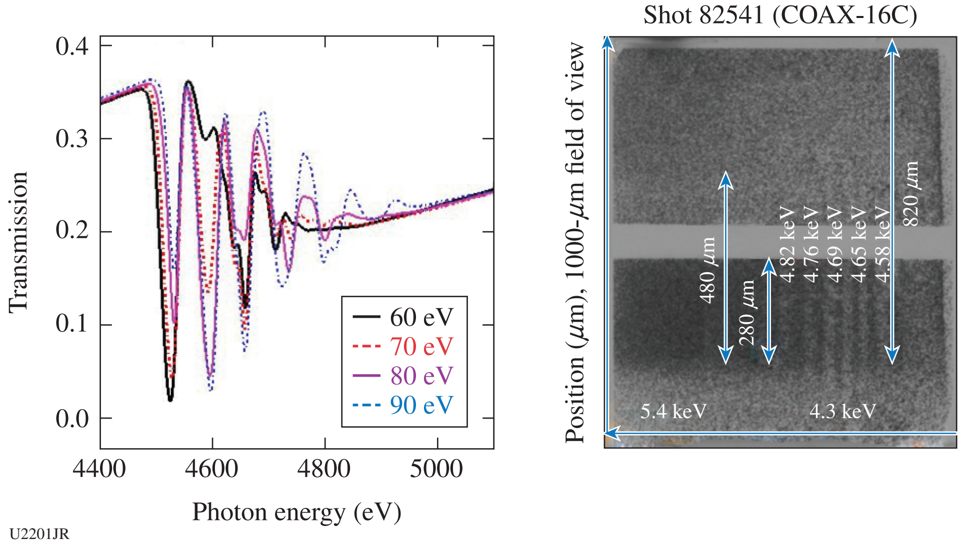

Figure 152.124
Data presented at APS DPP 2016 showing emission from the subsonic density spike superimposed on the spectral data.[43]

We observed emission from the subsonic density spike superimposed on the spectral data for the first time.

In May 2017 we collected high-resolution (~1000 resolving power) Ti and Sc spectroscopic data (Fig. 152.125). We tested a new design for the radiography backlighter, which unfortunately did not meet specification. The quality of the radiography was reduced as a result. We drove some targets with 600-ps and some with 1-ns square laser pulses to evaluate whether increased coasting time would improve the backlighter brightness. While that did occur, the physics target was much cooler than is typical because of the reduced drive energy. We repeated the observation of the subsonic front in the spectroscopic data with this higher-resolution, brighter spectra (produced as a result of improvements to the beam pointing for the capsule backlighter). A comparison between data from May and synthetic spectra produced with OPLIB in *PrismSPECT* was included in a presentation at the 2017 Anomalous Absorption Conference (Fig. 152.125).

In August 2017, we made a platform design change to move the physics target closer to target chamber center (TCC). This was partly to move the hohlraum back into the field of view for Dante and partly to improve backlighter flux through the physics target. We improved our design for the radiography V-foil backlighter and moved that target closer to TCC as well, to take advantage of the maximum drive range for the beams that this design allowed. We collected high-quality radiography and spectroscopy data with the new design (Fig. 152.126). We collected data at a sequence of times to study the transition between the supersonic and the subsonic flow over time. The times shown in Fig. 152.126 are the difference in time between the start of hohlraum drive and the time at which data were actually collected. At this year's APS DPP Meeting we will discuss early analysis results for this data, such as shown in Fig. 152.127. To address radiation-transport physics questions precisely enough to constrain radiation–hydrodynamics models, we need T_e uncertainty <5 eV and spatial uncertainty (from radiography) ~20 μm, which early analysis of our results

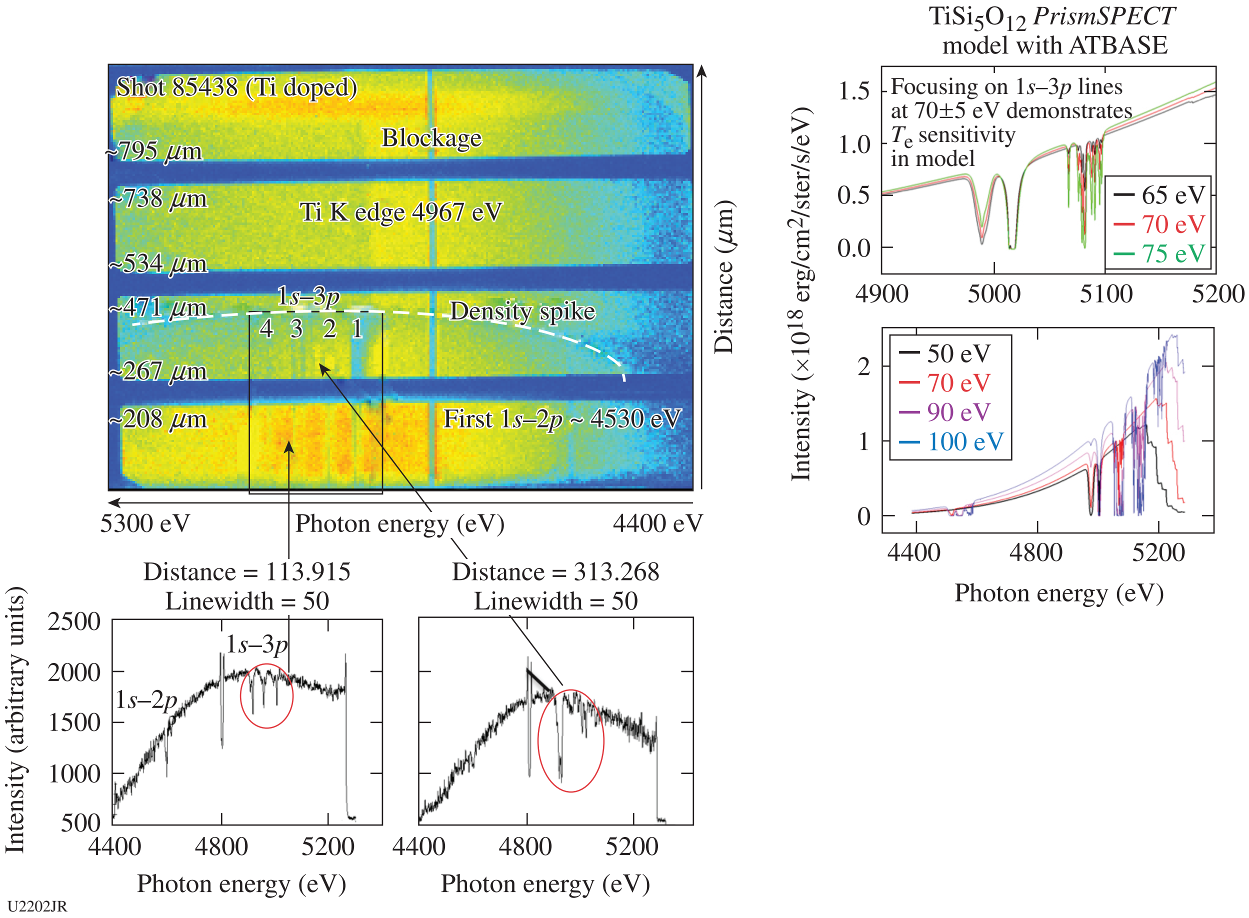

Figure 152.125
High-resolution Ti and Sc data with a comparison to synthetic data created using OPLIB in *PrismSPECT*.

(Fig. 152.127) implies we have achieved. Provided the rest of the analysis of the data from COAX-17B and COAX-17C is as promising, we will be starting the process for applying for NIF shots in 2018.

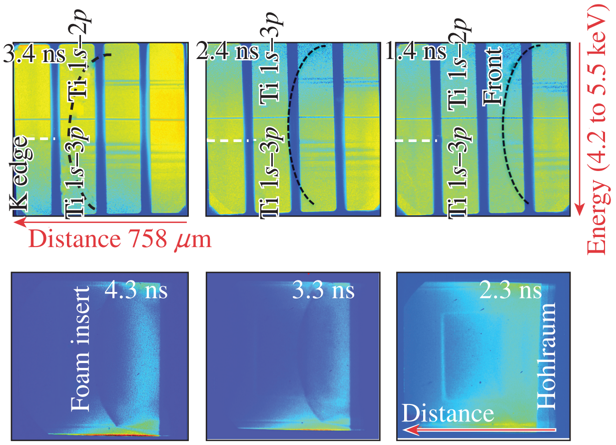

Figure 152.126
Improved data quality obtained using the modified platform developed in COAX-17C.

CylDRT

The first CylDRT/CylStalk shot day was scheduled on 29 August 2017. The main objective for this shot day was to measure the deceleration-phase Rayleigh–Taylor (RT) growth of the sine wave perturbations on the inner side of an aluminum marker layer in cylindrical geometry using face-on radiography. We are reviving the cylindrical problem after more than ten years on OMEGA. The cylinder is 250 μm longer than what was previously used because of the requirement to use SG5 phase plates. The Target Fabrication Group had to re-establish their capabilities including an outside vendor (AlumiPlate) for the marker layer coating. The goal is to measure the deceleration RT growth of the $m = 10$-mode sine wave inner perturbation on the aluminum marker layer.

Figure 152.128 shows the axial and transverse views of the cylindrical target. The cylinder was 2.5-mm long and had a 986-μm outer diameter. The inner diameter of the cylinder was 860 μm. In the middle and inner side of the cylinder was a 500-μm-long aluminum marker band, and the inner aluminum layer had sine wave perturbations mode 10 with 3-μm amplitude. Figure 152.129 shows the experimental geometry.

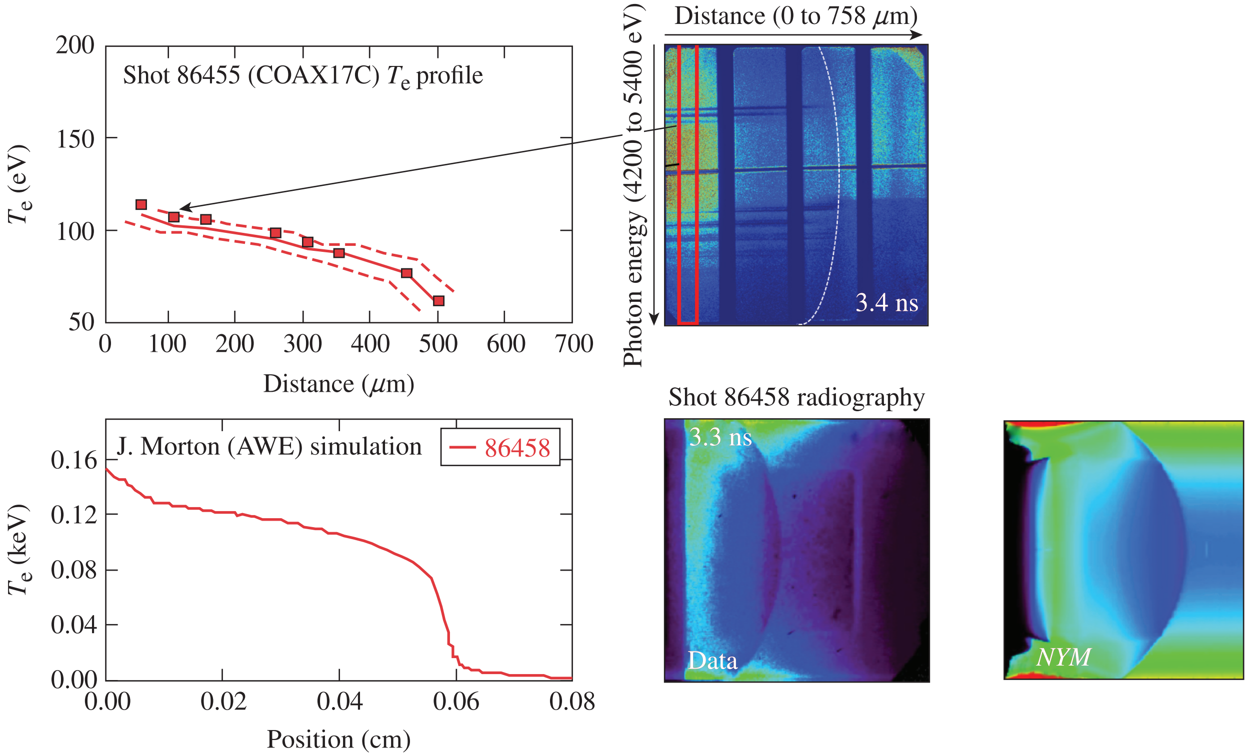

Figure 152.127
Electron temperature profiles obtained from the COAX data compared to simulations.

The cylinder was driven by 40 beams with a 1-ns square pulse. An iron or nickel backlighter was attached to the TIM-4 end of the cylinder. The x-ray framing camera was on TIM-6. We used 12× magnification with a 15-μm pinhole onto a four-strip framing camera. We also used a TIM-2/TIM-3 side imaging of the target to see the uniformity of the implosion.

Figure 152.130 shows the experimental image from a smooth target that had no sine wave perturbation for reference. Figure 152.131 shows the experimental image for a target with mode-10 sine wave. The preliminary analysis of the experimental results shows deceleration phase RT growth agreeing with hydro calculations.

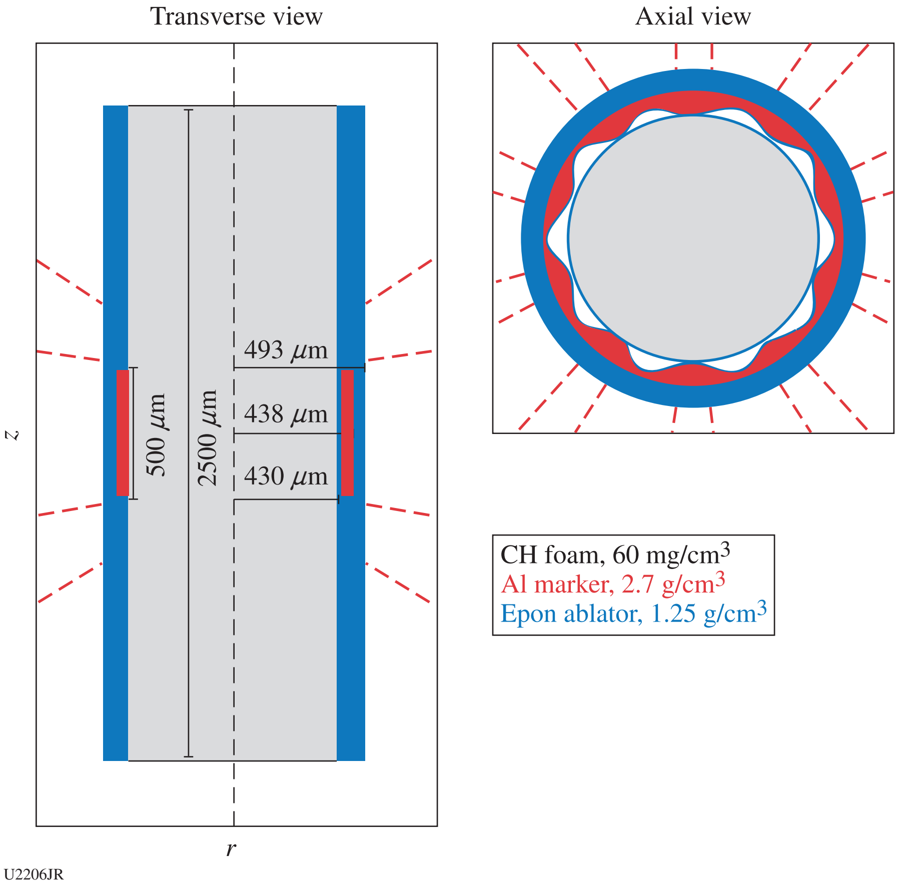

Figure 152.128
(a) Transverse and (b) axial views of the target.

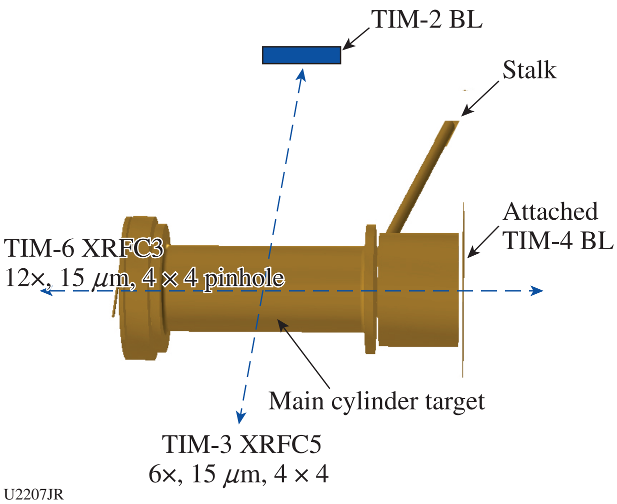

Figure 152.129
Experimental geometry for the CylDRT Campaign.

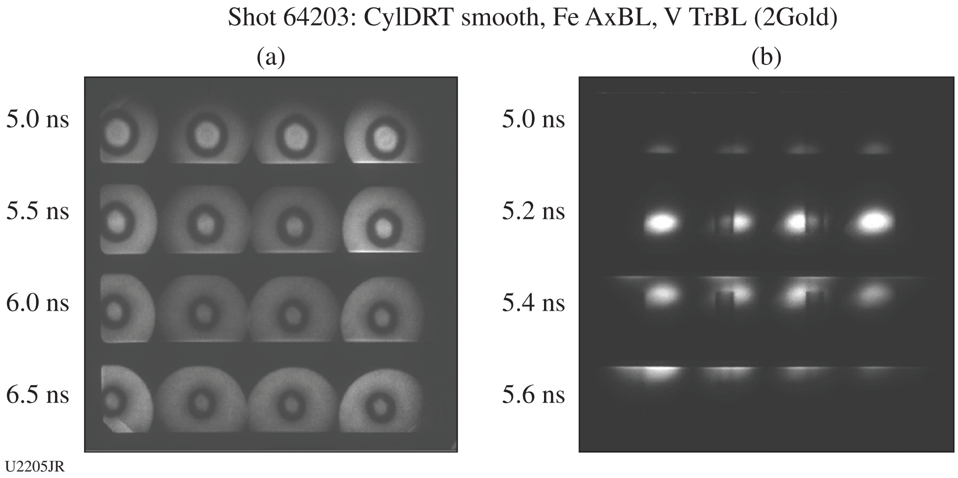

Figure 152.130
(a) Axial and (b) transverse x-ray radiographs of a smooth target.

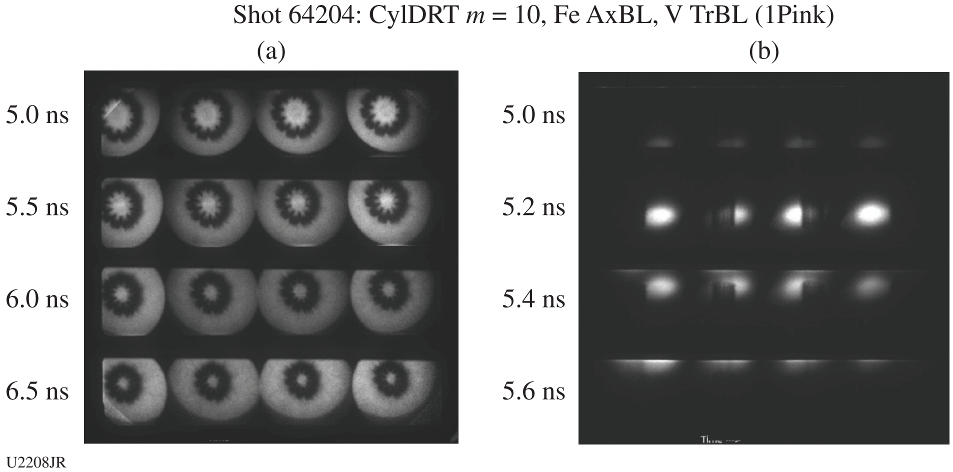

Figure 152.131
(a) Axial and (b) transverse x-ray radiographs of a mode-10 sine wave perturbation target.

DSPlanar

The Los Alamos Double-Shell team completed two planar double-shell (DSPlanar) experiments at the Omega Laser Facility in FY17. This campaign of experiments is part of the larger overall double-shell effort at Los Alamos, which is intended to test double-shell–relevant physics and materials in a planar geometry for ease of simulation and diagnosis. Specifically, these experiments are intended to validate our ability to predict hydro coupling, instability growth, with and without tamper mitigation, and the impact of target-fabrication artifacts such as fill tubes or joints in a double-shell target in the simplified planar geometry.

The first FY17 experiments examined momentum transfer during the ablator "inner shell" collision to benchmark *RAGE* simulations for similar systems. In these experiments, an indirectly driven ablator propagated down a shock tube [Fig. 152.132(a)] to impact a SiO_2 layer serving as an inner-shell surrogate. VISAR measurements [Fig. 152.132(b)] of the shock propagation, for pre- through post-ablator/layer impact, showed good breakout timing and average velocity agreement with pre-shot simulations.

The second FY17 shot day focused on studies of joint perturbation growth in support of NIF target-fabrication efforts.

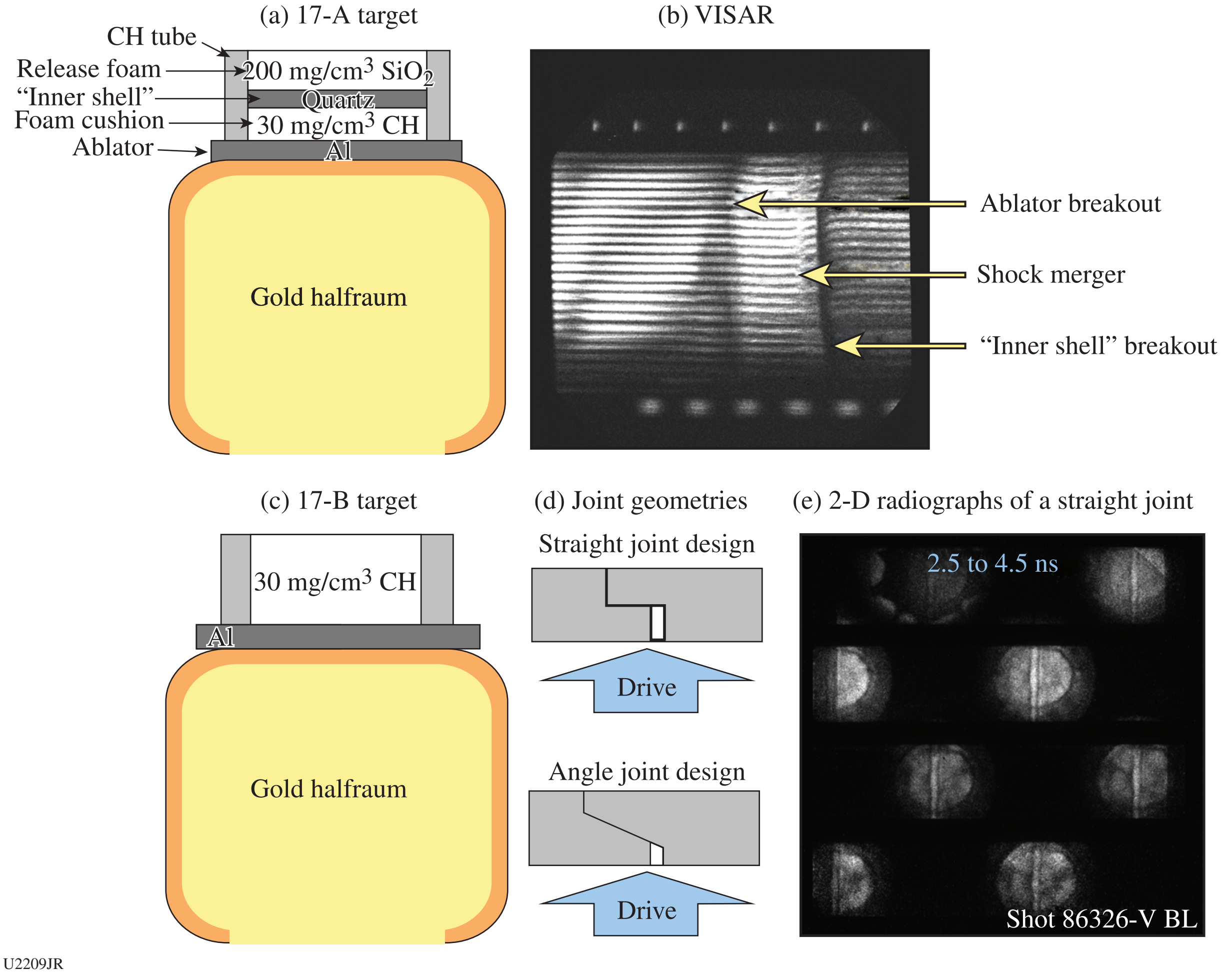

Figure 152.132
(a) Planar double-shell momentum transfer and (b) joint perturbation targets. (c) VISAR measurement of shock propagation, (d) schematic of joint propagation targets, and (e) radiographs of growth in a target with a straight joint.

These experiments again used indirectly driven ablators, but this time the ablator had a joint down the center. We varied the width of the joint gap as well as the geometry of the joint seam [Fig. 152.132(d)] for comparison to *RAGE* simulations. Early analysis suggests that *RAGE* simulations bound the observed joint growth rate and can serve to calculate an upper limit on the joint perturbation growth in a double-shell target.

HKMix

HKMix is a continuing LANL campaign to study mix physics in implosions between the fuel and shell, with the overarching goal of benchmarking models used in simulations of ICF and HED systems. These shots used 9- or 15-μm-thick, 860-μm-diam plastic shells with a thin deuterated (CD) layer in the shell and a HT gas fill. Using the LANL Cherenkov-based gamma ray detectors, both the HT (core) and DT (mix) burn histories can be measured.[44] The timing difference between mix and core burn is a novel constraint on modeling these implosions; good data were acquired, with analysis and interpretation ongoing.

These campaigns also used much thinner deuterated layers (0.15 μm) than past work, which enables higher resolution of the effect mix depth. Past work with 15-μm-thick shells could be explained using turbulence-based mix models, and these were used to predict the mix (DT) yield versus CD layer recession depth for these shots, shown by the green curves in Fig. 152.133. The data, however, show a dramatic 100× decrease in mix yield as the CD layer is recessed by only 0.3 μm. This trend cannot be explained by a turbulence-based model, but good agreement is found with a diffusion-based model (black curve).[45] At a 1-μm recession depth, the mix yield is observed to increase, indicating another "inversion" mix mechanism, potentially caused by a jet from the target support stalk.

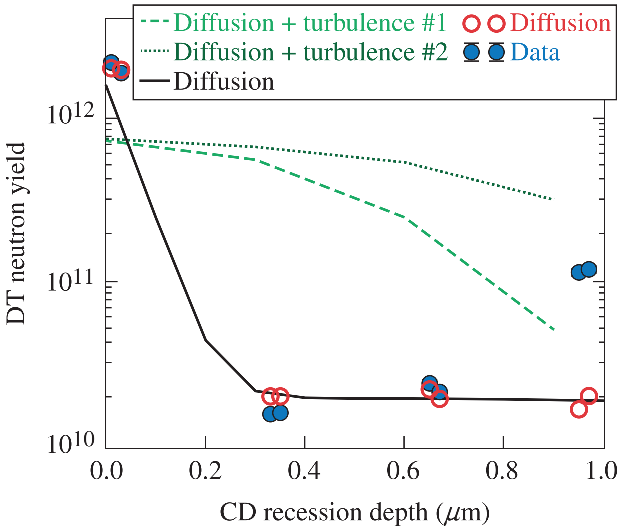

U2210JR

Figure 152.133
Mix (DT) yield versus CD layer recession depth compared to models.

IonSepMMI

In ICF experiments, interspecies ion separation is considered to be a candidate mechanism for yield degradation compared to radiation–hydrodynamic code predictions. This species separation could be driven by multispecies diffusive processes (e.g., thermodiffusion), as suggested by simulations employing recently implemented first-principles–based multi-ion–species transport models. The same physics also appears to drive ablator/gas mix in ongoing experiments focused on studying that problem.

Detailed analyses of x-ray–imaging spectroscopy data obtained from the earlier IonSepMMI-15A Campaign (in 2015) provided the first direct experimental evidence of interspecies ion separation in ICF experiments.[46,47]

To obtain the earlier results, we assumed 1-D spherical symmetry in the analysis procedure. In the recent IonSepMMI-17A Campaign (August 2017), we recorded x-ray–imaging spectroscopy data along three different lines of sight, which will allow us to analyze the data without needing to assume spherical symmetry and to perform 2-D/3-D reconstructions of spatial profiles of ion densities to infer ion species separation in the implosion core. We conducted 12 target shots with a high return of x-ray–imaging spectroscopy data on four target types of varying fill pressure and dopant (Ar) concentration. We also collected time-evolution data of both x-ray and DD-neutron reaction histories in collaboration with MIT, which fielded their PXTD diagnostic for this purpose. We anticipate improved observations of stronger and weaker interspecies ion separation as a function of target type. We are now processing and analyzing the x-ray spectroscopy data (Figs. 152.134 and 152.135). Further processing/analysis is being conducted to infer the spatial profile of argon concentration versus time, which is the smoking gun for whether species separation is occurring.

Results from these campaigns will add to our experimental database for validating first-principles models of multi-ion–species transport and diffusion that have been implemented in LANL ASC (advanced simulation and computing) codes. The latter will allow us to better quantitatively assess the impact of species separation that are initially mixed, as well as the mix of species that are initially separated (e.g., ablator/fuel) in ICF implosion performance.

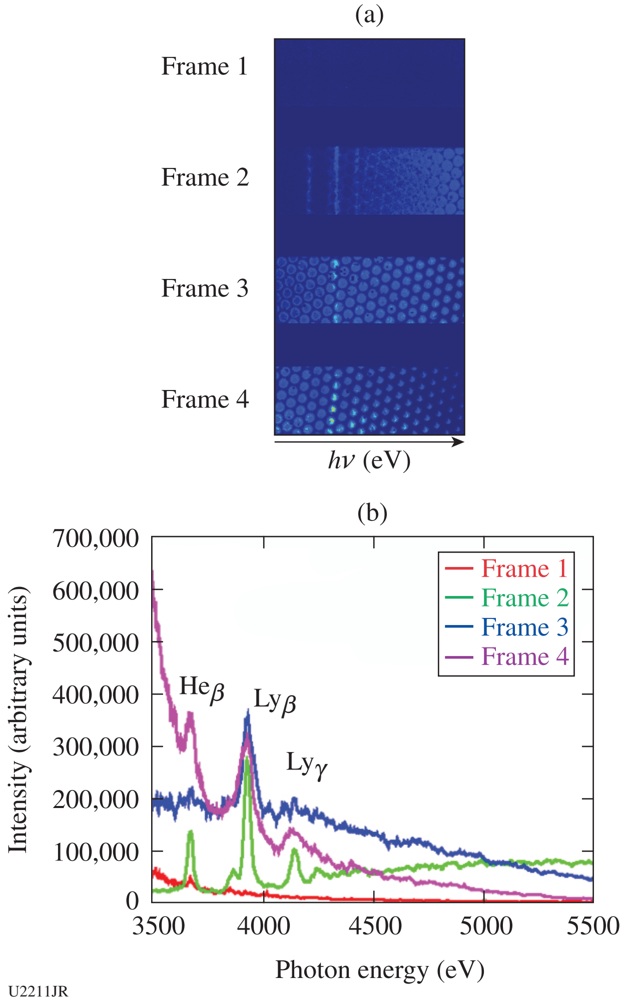

U2211JR

Figure 152.134
(a) Multi-monochromatic x-ray imager (MMI) data from shot 86678 (XRFC1, TIM-2) after processing and (b) space-integrated spectra from four frames of MMI (progressing in time, ~100-ps time interval between subsequent frames).

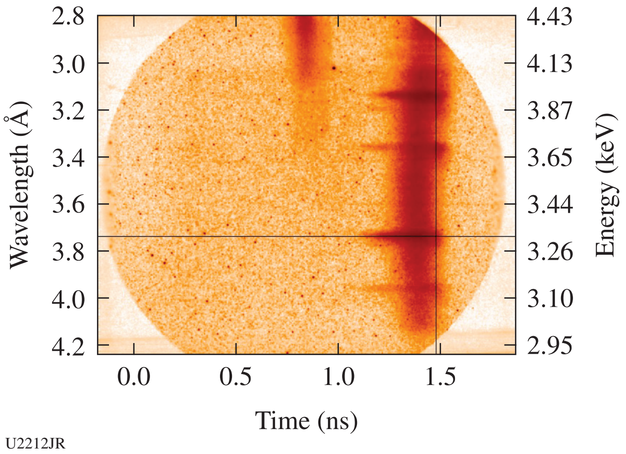

Figure 152.135
Streaked-crystal spectrometer (SSCA) data from shot 86678 (photon energy on vertical and time on horizontal axes, respectively).

Marble VC

The Marble Void Collapse Campaign was developed to address (1) fundamental issues relevant to understanding of Marble implosions on the NIF and (2) simulation capability of macro-pore engineered foams. This year, the Marble team refined a laser-driven shock-tube platform and tested two topics. First, shock propagation through macro-pore engineered foams were investigated to examine if the pore size affects shock speed. Three types of macro-pore engineered foams (<1, 50, and 90 μm in diameter) were used in shock-tube experiments driven by the OMEGA laser. X-ray radiographic data indicate that shock speed through macro-pore engineered foams depends strongly on foam density, less on pore size [Fig. 152.136(a)]. Data were successfully used to validate LANL simulation capability. Second, we designed a single foam-filled void (250 μm in diameter) [Fig. 152.136(b)] and shocked it from two opposing directions, aiming to increase turbulence at the spherical boundary and as a result induce magnetic fields. X-ray radiographic data show that while the first shock compressed a spherical foam-void without much turbulence, the time-delayed second shock seems to increase a turbulent motion. D^{3}He proton radiographic data (supported by the MIT group) were successfully obtained and are being analyzed.

MShock

The LANL MShock Campaign is studying the feedthrough of the RM instability in a thin layer, analogous to previous gas-curtain experiments. RM is relevant to mix in an ICF capsule where the ablative drive on capsule imperfections gives rise to RM and secondary shocks re-shock the linearly growing RM instability. It is known from fluids that such a re-shock can drive RM to turbulence. The MShock platform utilizes a beryllium shock tube analogous to the previous Shear Campaign. A thin high-density layer ~10× denser than surrounding foam is located a short distance from the first drive ablator. Two opposing laser drives with a 3-ns time delay directly drive ablators on the opposite side of the shock tube. This allows for a growth period between the initial excitation of the RM instability and the re-shock. X-ray radiography is used to capture the evolving layer; mix-width measurements are compared with the LANL Besnard–Harlow–Rauenzahn (BHR) turbulence model.

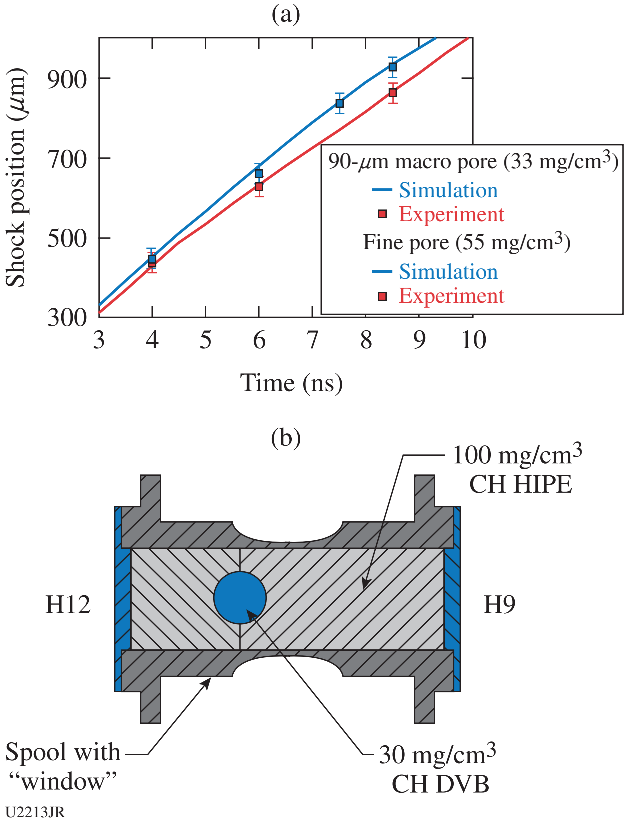

Figure 152.136
(a) Comparison of the simulated and measured shock position in fine-pore and 90-μm macropore foam and (b) the single-void target with the walls reduced in thickness to allow proton radiography of the shocked void. DVB: polystyrene/divinylbenzene.

FY17 was the first year of the MShock Campaign. The first shot day was focused on platform development and proof of concept for the target design. Data were collected to calibrate shock timings with simulations, and a new central doping technique applied to the high-density layer was verified (Fig. 152.137). In addition, the experiment showed no distortions of the mix layer, which had been previously observed in the OMEGA Re-shock Campaign. The second shot day focused on capturing time sequences for three surface perturbations and collecting photometric data for dopants in the high-density layer. Preheat characterizations on this day showed that preheat effects are strong enough to affect surface profiles. Sufficient data were collected for one of the surface modes and nearly all data were collected for another. The results from both of these days will aid in preparing future experiments for both OMEGA and the NIF.

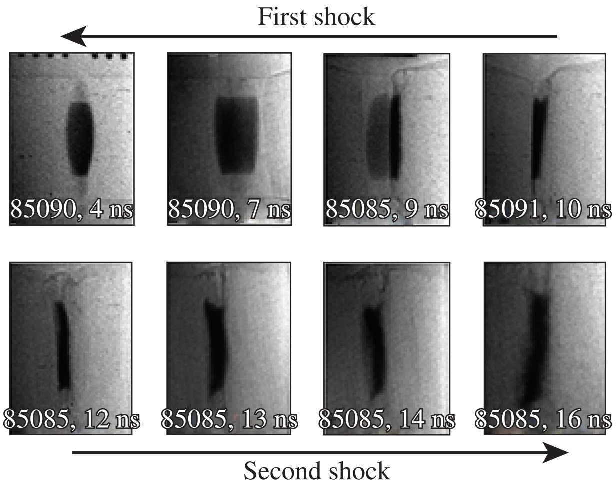

U2214JR

Figure 152.137
Data from a series of shots in the MShock Campaign.

Oblique Shock

The LANL Oblique Shock Campaign on OMEGA EP had two shot days in FY17 with a total of 14 shots. This campaign is designed to study the interplay between RM and KH hydrodynamic instabilities. It was conceived as a collaborative effort between LANL and the University of Michigan. The platform will also allow us to provide experimental input for testing and validation studies for turbulent transitional models like the LANL's modal model,[48] which will provide input for initial conditions for full turbulence models[49] like BHR.[50]

The first day was dedicated to testing (1) a 30-ns extended drive as an alternative to the typical 10-ns drive, and (2) the platform in a regime that more closely mirrors the University of Michigan'a hydro experiments on tilted interfaces (light to heavy). The Oblique Shock Campaign has been looking at shocks driven across an inclined (heavy-to-light) surface into a low-density foam (Fig. 152.138). Instead of three beams driving the target at one time, the three beams were stacked in time with 10 ns each, making a 30-ns train. In this configuration, the intensity driving the shock is reduced by a factor of 3, but the shock is supported for almost the entire experiment.

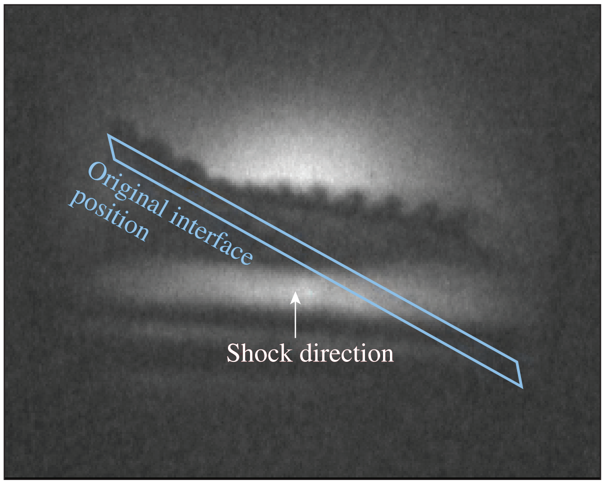

U2215JR

Figure 152.138
A two-mode interface undergoing shock with the original interface becoming flat with RM ripples on the front surface—an inversion of the original surface structure.

The current shots are intended to collect a time series of data that show how a two-mode perturbation on a heavy-to-light interface evolves with a sustained drive. This results in a later arrival time at the interface for the laser turn-off rarefaction, extending the time over which mixing-width growth can be considered to be predominantly caused by RM and KH growth. A two-mode interface was tested (Fig. 152.139) with the longer pulse, yielding a new data set for modeling.

The second shot day was dedicated to testing a new multimode surface to study the effects of mode coupling on the growth of the interface. The 10-ns drive focused three beams

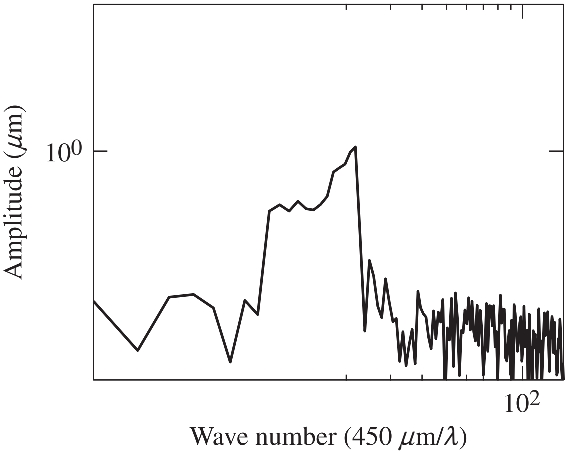

U2216JR

Figure 152.139
The machined interface of the single-band multimode spectrum in wave-number space that was used as a seed for the RM instability.

on the ablator to drive a strong shock into the tube as in previous experiments; the setup was the same as Fig. 152.138. Figure 152.140 shows the imposed interface for studying mode coupling. The idea is for the mid modes to couple to the low modes, which would allow us to track the mode growth. The shot day showed very promising results; however, it also showed the limitations of our diagnostics and alignment procedures (Fig. 152.141). These are being enhanced for the next shot day to improve our resolution and contrast using a new Mn-He$_\alpha$ quartz asphere for the spherical crystal imager (SCI), which will allow us to use long-pulse (0.5- to 1-ns) beams to illuminate the backlighter targets; this in turn will allow us to produce far more x rays to view the layer and increase our resolution by using film instead of image plates. In the future, we will take advantage of the new SCI magnification (15×) to further increase resolution.

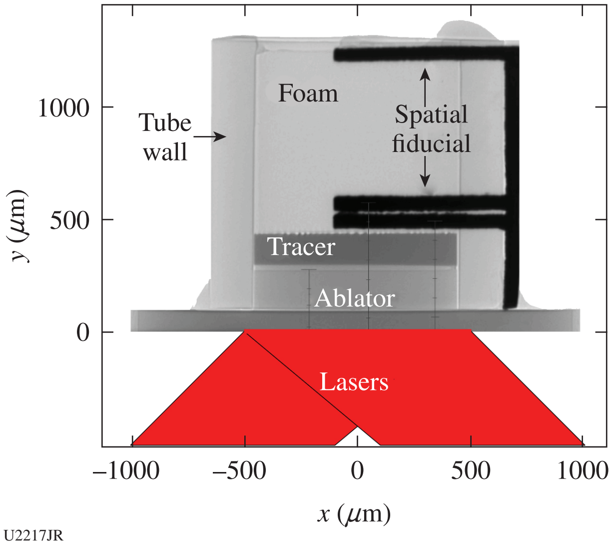

Figure 152.140
The Oblique Shock shock tube for OMEGA EP consists of a CH or Be tube with a CH ablator top hat, where laser energy is absorbed and launches a shock into the tube across the high-density tracer layer into the low-density foam.

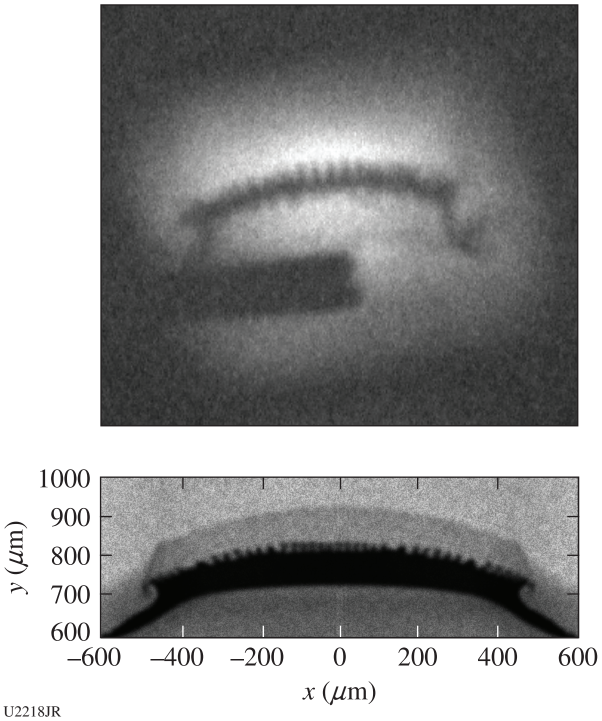

Figure 152.141
Experimental image of the single-band multimode interface on top and underneath the simulated image using *RAGE*.

WFEOS

The goal of the WFEOS-17A shot day was to study the equation of state (EOS) of wetted-foam material. The LANL ICF Program is conducting liquid layer implosions on the NIF, where the liquid is wicked into a supporting foam shell on the inner surface of the capsule. The implosion dynamics and performance are sensitive to the EOS of the mixed foam/DT material because it sets the implosion adiabat, but the EOS of such mixtures has not been measured. The WFEOS-17A Campaign used the planar cryogenic capability on OMEGA with the active shock breakout (ASBO)/streaked optical pyrometer (SOP) diagnostic to measure the shock propagation through a liquid-D_2 wetted foam. Good data were acquired on several shots. An example interferometry streak from VISAR on shot 85712 is shown in Fig. 152.142. In addition to the shock release

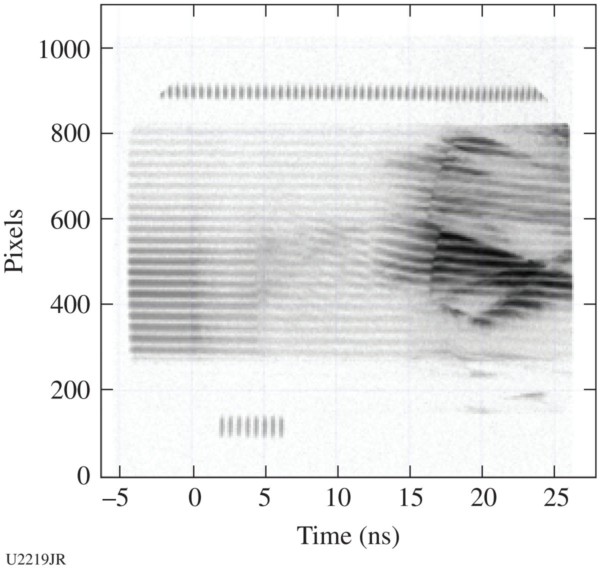

Figure 152.142
ASBO data from WFEOS-17A shot 85712.

from a high-density carbon pusher into the wetted-foam material, we observe a change in shock velocity at the wetted-foam interface with pure D_2, indicating a noticeable difference in the EOS of the two materials.

FY17 SNL Report on Omega Facility Experiments

MagLIFEP and MagLIFSNL

Principal Investigators: A. J. Harvey-Thompson, M. Glinsky, M. Weis, T. Nagayama, and K. Peterson (SNL); M. S. Wei, J. Fooks, E. Giraldez, and C. M. Krauland (General Atomics); E. M. Campbell, J. R. Davies, J. Peebles, R. E. Bahr, D. H. Edgell, C. Stoeckl, D. Turnbull, and V. Yu. Glebov (LLE); and J. A. Emig, R. F. Heeter, and D. Strozzi (LLNL)

The MagLIFEP and MagLIFSNL Campaigns at LLE operated by Sandia National Laboratories conducted a total of four shot days in FY17 (one on OMEGA and three on OMEGA EP) aimed at characterizing the laser heating of underdense plasmas (D_2, Ar) at parameters that are relevant to the magnetized liner inertial fusion (MagLIF) ICF scheme.[51,52] MagLIF combines fuel preheat, magnetization, and pulsed-power implosion to significantly relax the implosion velocity and ρR required for self-heating. Effective fuel preheat requires coupling several kilojoules of laser energy into the 10-mm-long, underdense (typically $n_e / n_c < 0.1$) fusion fuel without introducing significant mix. Barriers to achieving this include the presence of laser–plasma instabilities (LPI's) as laser energy is coupled to the initially cold fuel, and the presence of a thin, polyimide laser entrance hole (LEH) foil that the laser must pass through and that can be a significant perturbation.

Experiments, having different goals, were performed on the OMEGA and OMEGA EP lasers. The objectives of the OMEGA EP experiments were to develop a spectrometer capable of viewing Ne K-shell emission ($h\nu = 920$ to 1100 eV), and to continue to investigate the effects of pulse shaping and LEH foil thickness on energy coupling. Capturing Ne spectra required developing a new spectrometer based on the spatially (in 1-D) and temporally resolved multipurpose spectrometer (MSPEC) design that used a KAP or RbAP with a maximized Bragg angle giving an observable energy range of 891 to 1773 eV (Ref. 53). In addition, modifications to the targets were required that allowed soft x rays to escape while still accommodating high-pressure (up to 10 atm) gas fills. This was achieved by machining up to five slots in the sides of the 115-μm-thick CH tube target and covering the slots with a 2-μm-thick polyimide foil, as shown in Fig. 152.143(a). Capturing Ne spectrum was challenging but was achieved as shown in Fig. 152.143(b). The instrument should allow one to observe cooling of the plasma after the laser has turned off, potentially facilitating the study an applied magnetic field's effect on the electron thermal conduction and cooling process.

The objective of the OMEGA laser experiments was to compare energy coupling into underdense D_2 plasmas with 2ω

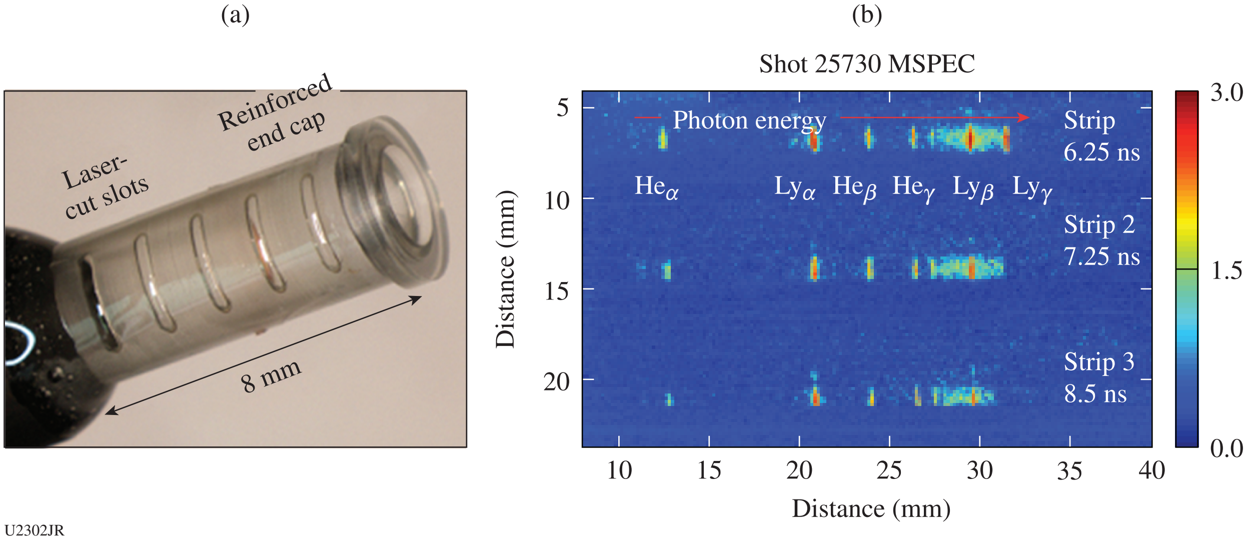

Figure 152.143
(a) Photograph of an OMEGA EP target with five side-on windows covered with a 2-μm polyimide foil capable of holding 10 atm and (b) a spectrum captured with the Ne multipurpose spectroscopy snout (MSPEC) on shot 25730 from MagLIFEP_17B showing the observed multiple Ne K-shell lines.

and 3ω beams, with and without smoothing by spectral dispersion (SSD), and for different beam intensities. This shot series was the first Sandia-led effort to investigate preheat on this laser, and, as such, scaled-down versions of the OMEGA EP targets were required because of the reduced energies per beam available (~450 J max compared to >3 kJ on OMEGA EP). Of particular interest in this series was the effect that changing the laser wavelength, intensity, and smoothing had on-beam propagation and on-stimulated Brillouin scattering (SBS) and stimulated Raman scattering (SRS) levels. The results suggest that for similar intensities and similar values of n_e/n_c, the laser wavelength has a significant effect on the beam propagation, as measured by x-ray framing camera (XRFC) imaging [Fig. 152.144(a)], and on LPI levels, as inferred by hard x-ray signal levels [Fig. 152.144(b)], while SSD has little impact. The results have implications for the future of MagLIF laser preheat, which currently uses a 2ω laser and is susceptible to significant LPI at relatively low intensities. The data suggest that a 3ω laser could make preheat possible at higher intensities for given plasma parameters while minimizing LPI, ensuring that greater energy coupling could be possible over a given propagation distance.

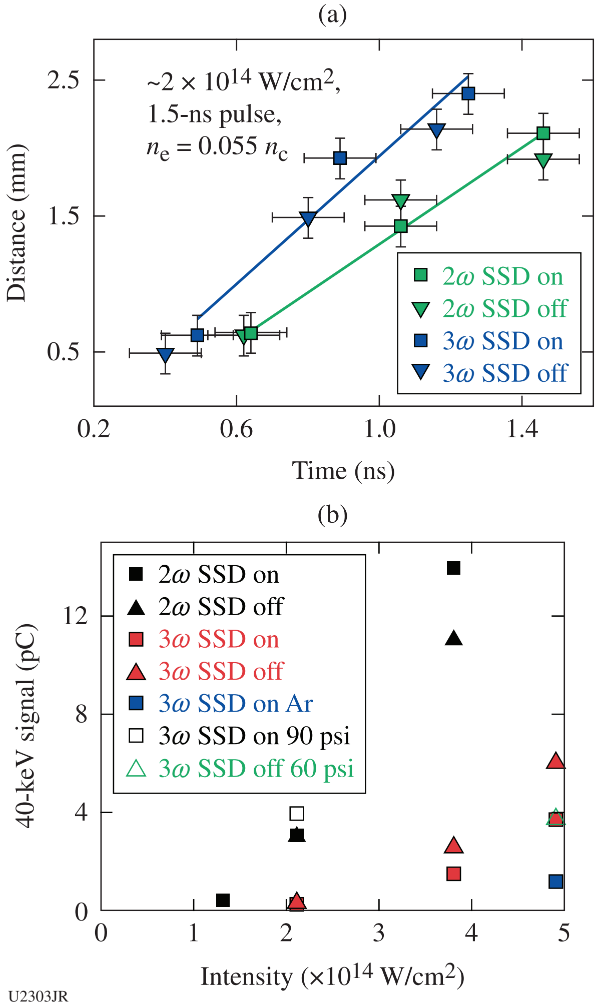

Figure 152.144
(a) Emission depth as a function of time measured from time-gated XRFC images for 2ω and 3ω light with SSD on and off and (b) hard x-ray signal levels as a function of intensity for the various parameters tested in the experiment.

ACKNOWLEDGMENT

Sandia National Laboratories is a multi-mission laboratory managed and operated by National Technology & Engineering Solutions of Sandia, LLC, a wholly owned subsidiary of Honeywell International, Inc., for the U.S. Department of Energy's National Nuclear Security Administration under contract DE-NA0003525.

FY17 NRL Report on Omega Facility Experiments

During FY17, an NRL/LLE collaboration on laser imprint led to three successful shot days on OMEGA EP. The experiments showed that the application of a prepulse that pre-expands and lifts off the coating prior to the arrival of the main laser pulse gives an order-of-magnitude reduction of laser imprint, as expected on the basis of the original experiments on the Nike laser and understanding the mechanism of the imprint suppression (Fig. 152.145). Further experiments demonstrated imprint reduction with prepulse times compatible with pulse durations available for implosions on the Omega 60-beam laser. Moreover, we were able to utilize thinner coatings, minimizing the risk of fuel preheat and increasing the chances that they will be compatible with low-adiabat, thin-ablator shell implosions on OMEGA.

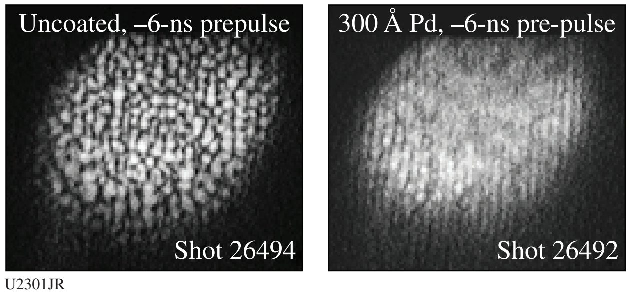

Figure 152.145
Measurements on OMEGA EP showing a reduction in laser imprint with a thin Pd coating. (a) An accelerated uncoated plastic foil broken up by Rayleigh–Taylor instability amplified laser imprint. (b) With a thin palladium coating, the target maintains integrity and the regular ripple structure preimposed on the foils becomes evident.

FY17 CEA Report on Omega Facility Experiments

Experimental Investigation of the Collective Stimulated Raman and Brillouin Scattering of Multiple Laser Beams in Inertial Confinement Fusion Experiments

Principal Investigators: C. Neuville, S. Depierreux, V. Tassin, M.-C. Monteil, P.-E. Masson-Laborde, P. Fremerye, F. Philippe, P. Seytor, D. Teychenné, M. Casanova, A. Debayle, P. Loiseau, and G. Tran (CEA-DAM-DIF); C. Baccou, C. Labaune, and C. Riconda (LULI); D. Pesme, S. Hüller, and A. Heron (Centre de Physique Theorique); V. Tikhonchuk, A. Colaitis, G. Duchateau, and P. Nicolaï (CELIA); N. Borisenko and A. Orekhov (Lebedev Physical Institute); and R. Bahr, J. Katz, C. Stoeckl, and W. Seka (LLE)

In the direct- and indirect-drive approaches to inertial confinement fusion, the megajoule laser energy is delivered through tens of beams grouped by cones—a regular arrangement that intrinsically includes principal directions for the amplification of laser–plasma instabilities (LPI's) by multiple beams. In this way, a collective instability can develop when all the incident laser waves located in a cone couple to a same daughter wave growing along the cone's symmetry axis. These collective effects were theoretically studied in the 1990s (Ref. 54) and evidenced for the two-plasmon decay in direct-drive experiments performed on OMEGA.[55–57] Similar collective multibeam coupling may be expected for the stimulated scattering instabilities, namely stimulated Brillouin scattering (SBS) and stimulated Raman scattering (SRS), in which the incident laser waves resonantly couple with ion acoustic waves (IAW's) or electron plasma waves (EPW's) to amplify scattered light waves. As in the single-beam configuration, the collective scattering instabilities can reduce the coupling efficiency of the beams with the target, accelerate copious amount of hot electrons, and modify the symmetry of the implosion. Additionally, the convective gain for the collective instabilities is increased compared to the single-beam instability, leading to expected higher levels of scattering. Another aspect of collective instabilities concerns its sidescattering geometry that results in the emission of the scattered light in novel directions compared to backscattering.

Multibeam effects in LPI at the megajoule scale were first considered through the cross-beam energy transfer between two beams that was used to adjust the symmetry of irradiation.[58,59] Recent experiments performed in near-vacuum hohlraums have revealed another multibeam effect, namely the electromagnetic seeding[60–62] of the sidescattering for some beams by the backscattering or transmission of additional beams.[63] The issue of collective scattering instabilities has recently become an emerging field with several reported experimental studies. In this context, two experiments have been performed on OMEGA to investigate collective SRS[64] and collective SBS.[65] The SRS of two beams has been evidenced in an inhomogeneous plasma produced in an open planar geometry where the significant amplification of the Raman light at large angles from the density gradient has been observed for the first time. The collective Brillouin amplification of shared IAW's has been observed in indirect-drive experiments using a rugby-ball–shaped hohlraum. In both types of experiments, the flexibility of the Omega Laser Facility and its large battery of diagnostics have played a critical role toward the physical understanding of the collective mechanisms.

The first experiment was performed to investigate the collective SRS produced by two beams sharing a common electromagnetic daughter wave in an inhomogeneous plasma. The targets were 7-mg/cm^3 $C_{12}H_{16}O_8$ foams with a diameter of 2.5 mm and a length of 950 μm aligned along the H3–H18 axis of the OMEGA target chamber. The laser beams were focused by $f = 6.7$ lenses through elliptical phase plates, producing spot sizes with a 200 × 300-μm diameter [full width at half maximum (FWHM)]. These beams were fired at an energy level of 400 J in a 1-ns square pulse. Twelve beams were used, incident at 60° from the foam axis, making a six-beam cone on each side of the target, as is illustrated for the H18 side in Fig. 152.146(a). After ~0.5 ns, the regions of foam ionized by the different beams of the same cone began to superimpose.

Figure 152.146(b) shows a typical measurement with the near-backscatter imager (NBI) of the time-integrated angular distribution of the light scattered in the Raman wavelength range (450 to 900 nm) around the midplane of Beamlines 45 and 50 with angles between 20° and 60° from the target normal. The SRS signal was maximum in the bisecting plane of beams 45 and 50 at angles between 42° and 54° from the target normal, close to the full-aperture backscatter station of Beamline 25 (FABS25). Figure 152.146(c) shows the time-resolved spectrum of the light scattered in this direction collected in an aperture of ±4° in FABS25 for the same shot. The SRS signal started at $t \sim 0.5$ ns, as soon as the beams started overlapping in the foam plasma. It lasted until the end of the laser pulses with an almost constant wavelength of $\lambda_{\text{SRS}} \sim 600$ nm, corresponding to the electron density (~0.17 n_{c}) in the region of beam overlap.

This observation in vacuum of the SRS scattered light at ~48° from the target normal corresponds to SRS light produced at ~80° from the density gradient in the plasma region of interaction. This optimum angle results from the increase of

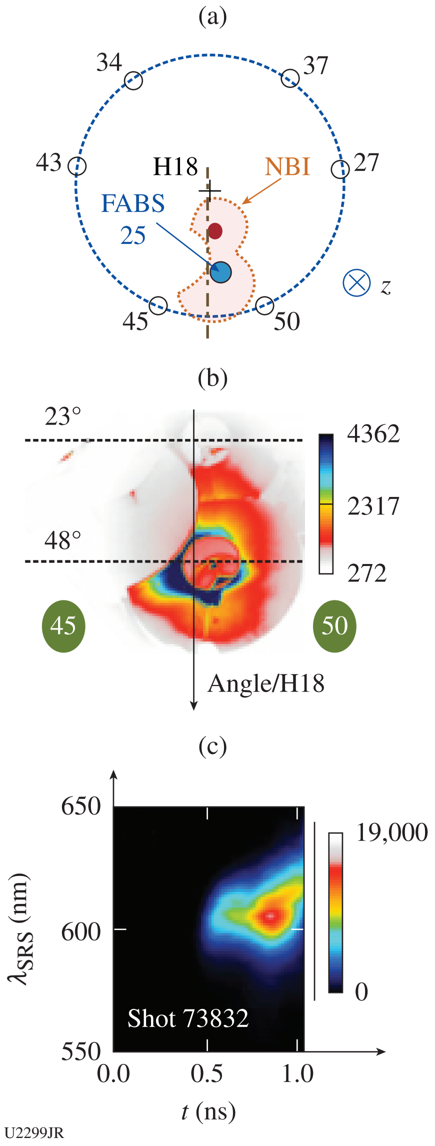

Figure 152.146
(a) Angular distribution of the six beams incident on the H18 side and scheme of the near-backscatter imaging (NBI) diffuser plate. (b) Typical image recorded with the NBI diagnostic for a 7-mg/cm^3 foam. (c) Time-resolved spectrum of the stimulated Raman scattering (SRS) light collected in the direction of FABS25 (full-aperture backscatter station) in the same shot as for (b).

the SRS collective gain partly compensated by the increased collisional absorption of the SRS signal as the light is scattered at larger angles from the density gradient. Absolute energy measurements performed in a calorimeter in this same direction indicated that the SRS losses associated with this signal maximized at ~5% of the power available in one beam. Last, the initial scattering angle ~80° is in good agreement with the hot-electron generation inferred from hard x-ray emission, giving a hot-electron temperature of 20 keV compared to an expected temperature of 25 keV.

The collective nature of the coupling and the amplification at large angles from the density gradient are found to increase the global SRS losses and to produce light scattered in novel directions outside the planes of incidence of the two beams. The mechanism evidenced in this experiment can occur in both direct- and indirect-drive experiments between any pair of beams. Such a collective amplification of a common scattered-light wave has been proposed to explain the large amount of SRS measured in the NIF indirect-drive experiments.[66] It results in an underestimation of the scattered-light losses because this red-shifted Raman light experiences significant refraction and absorption before exiting the plasma and in the acceleration of hot electrons, which can preheat the capsule.

The second experiment was performed to investigate collective Brillouin scattering in indirect-drive experiments. The interaction was studied at the laser entrance hole (LEH) of rugby-ball–shaped hohlraums filled with 1 atm of methane gas. The revolution axis of the hohlraum was aligned along the P5–P8 axis of the OMEGA target chamber. Twenty laser beams were incident on each side of the target distributed along three cones [see Fig. 152.147(a)]: five beams, at 21° from the axis, were pointed at 500 μm from the window outside the hohlraum; similarly, five beams at 42° and ten beams at 59° were pointed at the LEH. The beams were focused by $f = 6.7$ lenses through random-phase plates, producing focal spots with a diameter of 300-μm FWHM. The laser pulse, with a total duration of 2.5 ns, was made of a prepulse of intensity ~8×10^{13} W/cm^2 per beam followed by a main pulse for $t = 1.8$ to $t = 2.3$ ns at an intensity per beam of 5×10^{14} W/cm^2. The plasma conditions were characterized thanks to thermal Thomson-scattering (TS) measurements performed at the LEH and at 300 μm from the LEH outside the hohlraum as illustrated in Fig. 152.147(a).

The scattered light was collected in the backward direction of one beam of the 59° cone (Beamline 30) and one beam of the 42° cone (Beamline 25) and analyzed in time and wavelength by full-aperture backscatter stations (FABS30 and FABS25). Figure 152.147(b) shows a typical spectrum measured in FABS30. For the time interval (1.8 ns to 2.4 ns), when the laser intensity was close to its maximum, two contributions were detected in FABS30. The first signal, starting at $t = 1.8$ ns, was caused by Brillouin backscattering of Beamline 30 developing in the plasma inside the hohlraum. The backscattering was identified in the single-beam linear gain calculations performed by post-processing the hydrodynamics simulations. It simply

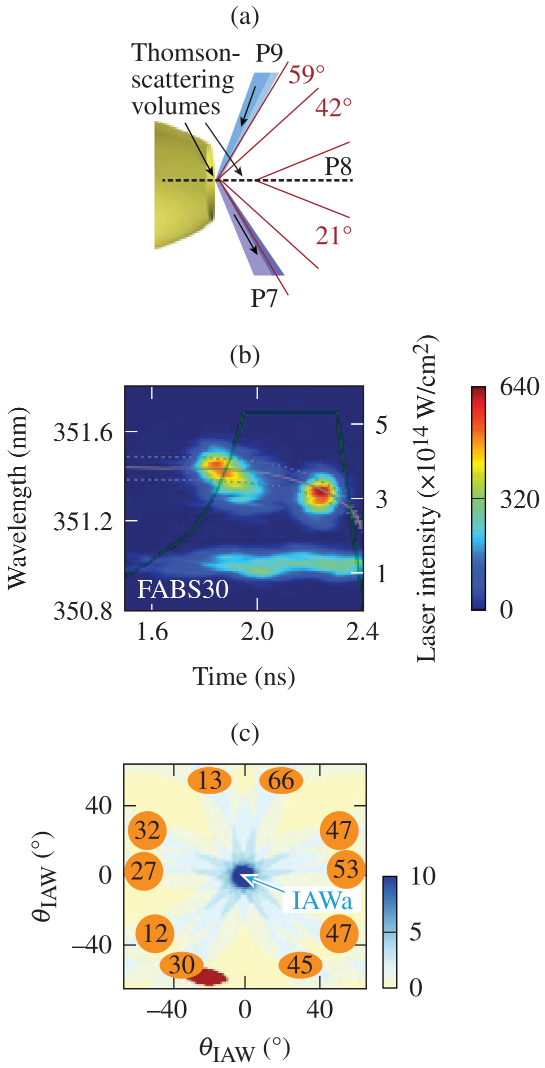

Figure 152.147
(a) Representation of the laser entrance hole (LEH) showing three cones of heater beams and the geometry of the Thomson-scattering (TS) diagnostic. (b) Time-resolved spectrum of the scattered light collected in the backward direction of Beamline 30. The gray lines represent the wavelength range calculated for the light scattered by Beamline 66 in the FABS30 direction off the collective IAW driven along the hohlraum axis by the ten-beam instability. (c) The direction of the IAW's having equal wave vectors are shown with respect to the ten laser beams of the 59° cone. A collective IAW is driven in each of the directions where multiple beams contribute. In the direction indicated as IAWa, the ten beams amplify the corresponding IAW. The region shown in red represents the scattering direction of Beamline 66 off IAWa.

depended on the energy of the beam itself. The origin of the second signal, observed after $t = 2.2$ ns, was different since we observed that the variations in time and amplitude were dependent on the energy of the other cone of crossing beams. This signal extended over a very narrow spectral range, corresponding exactly to the wavelength expected as a result of the Thomson-scattering measurements for the light scattered by Beamline 66 off the collective IAW's generated by the ten beams at 59° [IAWa in Fig. 152.147(c)]. The observation of a sidescattering signal peaked in wavelength was a strong indication of multibeam effects. In a different experiment, using a different pointing[67] of the ten beams of the 59° cone to improve the uniformity of irradiation on the hohlraum wall, significant spectral broadening of this second signal was observed as expected from the widening of the crossing volume of the ten beams of the 59° cone.

The absolute energy measurements performed in the FABS made it possible to evaluate the energy losses caused by the collective SBS instability of the 59° cone. To do so, we first considered the geometry of the scattering, taking into account the aperture of the beams and the diagnostic. The geometry of the SBS of Beamline 66 in the collective instability that drove the IAW along the hohlraum axis (IAWa) is shown in Fig. 152.147(c), assuming straight-line propagation of the light in front of the crossing-beam region at LEH. Its analysis showed that only a small fraction (<1/15) of the scattered light was collected in the FABS. The signal associated with the collective instability of the ten beams peaked at ~3% of the laser power per beam, but we estimate that the scattering losses may be 10× higher than those directly measured in the FABS. Therefore, collective Brillouin scattering can result in high scattering amplitude and significantly impair the laser–target coupling in indirect-drive experiments.

REFERENCES

1. D. B. Schaeffer, W. Fox, D. Haberberger, G. Fiksel, A. Bhattacharjee, D. H. Barnak, S. X. Hu, and K. Germaschewski, Phys. Rev. Lett. **119**, 025001 (2017).
2. D. B. Schaeffer, W. Fox, D. Haberberger, G. Fiksel, A. Bhattacharjee, D. H. Barnak, S. X. Hu, K. Germaschewski, and R. Follett, "High-Mach Number, Laser-Driven Magnetized Collisionless Shocks," submitted to Phys. Plasmas.
3. G. Fiksel, W. Fox, A. Bhattacharjee, D. H. Barnak, P.-Y. Chang, K. Germaschewski, S. X. Hu, and P. M. Nilson, Phys. Rev. Lett. **113**, 105003 (2014).
4. L. Willingale, P. M. Nilson, A. G. R. Thomas, J. Cobble, R. S. Craxton, A. Maksimchuk, P. A. Norreys, T. C. Sangster, R. H. H. Scott, C. Stoeckl, C. Zulick, and K. Krushelnick, Phys. Rev. Lett. **106**, 105002 (2011).
5. L. Willingale, A. G. R. Thomas, P. M. Nilson, H. Chen, J. Cobble, R. S. Craxton, A. Maksimchuk, P. A. Norreys, T. C. Sangster, R. H. H. Scott, C. Stoeckl, C. Zulick, and K. Krushelnick, New J. Phys. **15**, 025023 (2013).
6. S. Brygoo, M. Millot, P. Loubeyre, A. E. Lazicki, S. Hamel, T. Qi, P. M. Celliers, F. Coppari, J. H. Eggert, D. E. Fratanduono, D. G. Hicks, J. R.

Rygg, R. F. Smith, D. C. Swift, G. W. Collins, and R. Jeanloz, J. Appl. Phys. **118**, 195901 (2015).

7. H. Sio, R. Hua, Y. Ping, C. McGuffey, F. Beg, R. Heeter, C. K. Li, R. D. Petrasso, and G. W. Collins, Rev. Sci. Instrum. **88**, 013503 (2017).

8. M. Gatu Johnson, A. B. Zylstra, A. Bacher, C. R. Brune, D. T. Casey, C. Forrest, H. W. Herrmann, M. Hohenberger, D. B. Sayre, R. M. Bionta, J.-L. Bourgade, J. A. Caggiano, C. Cerjan, R. S. Craxton, D. Dearborn, M. Farrell, J. A Frenje, E. M. Garcia, V. Yu. Glebov, G. Hale, E. P. Hartouni, R. Hatarik, M. Hohensee, D. M. Holunga, M. Hoppe, R. J. Janezic, S. F. Khan, J. D. Kilkenny, Y. H. Kim, J. P. Knauer, T. R. Kohut, B. Lahmann, O. Landoas, C. K. Li, F. J. Marshall, L. Masse, A. McEvoy, P. McKenty, D. P. McNabb, A. Nikroo, T. G. Parham, M. Paris, R. D. Petrasso, J. Pino, P. B. Radha, B. Remington, H. G. Rinderknecht, H. Robey, M. J. Rosenberg, B. Rosse, M. Rubery, T. C. Sangster, J. Sanchez, M. Schmitt, M. Schoff, F. H. Séguin, W. Seka, H. Sio, C. Stoeckl, and R. E. Tipton, Phys. Plasmas **24**, 041407 (2017).

9. C. Stoeckl, R. Epstein, R. Betti, W. Bittle, J. A. Delettrez, C. J. Forrest, V. Yu. Glebov, V. N. Goncharov, D. R. Harding, I. V. Igumenshchev, D. W. Jacobs-Perkins, R. T. Janezic, J. H. Kelly, T. Z. Kosc, R. L. McCrory, D. T. Michel, C. Mileham, P. W. McKenty, F. J. Marshall, S. F. B. Morse, S. P. Regan, P. B. Radha, B. S. Rice, T. C. Sangster, M. J. Shoup III, W. T. Shmayda, C. Sorce, W. Theobald, J. Ulreich, M. D. Wittman, D. D. Meyerhofer, J. A. Frenje, M. Gatu Johnson, and R. D. Petrasso, Phys. Plasmas **24**, 056304 (2017).

10. V. N. Goncharov, S. P. Regan, E. M. Campbell, T. C. Sangster, P. B. Radha, J. F. Myatt, D. H. Froula, R. Betti, T. R. Boehly, J. A. Delettrez, D. H. Edgell, R. Epstein, C. J. Forrest, V. Yu. Glebov, D. R. Harding, S. X. Hu, I. V. Igumenshchev, F. J. Marshall, R. L. McCrory, D. T. Michel, W. Seka, A. Shvydky, C. Stoeckl, W. Theobald, and M. Gatu-Johnson, Plasma Phys. Control. Fusion **59**, 014008 (2017).

11. H. G. Rinderknecht, P. A. Amendt, M. J. Rosenberg, C. L. Li, J. A. Frenje, M. Gatu Johnson, H. Sio, F. H. Séguin, R. D. Petrasso, A. B. Zylstra, G. Kagan, N. M. Hoffman, D. Svyatsky, S. C. Wilks, V. Yu. Glebov, C. Stoeckl, and T. C. Sangster, Nucl. Fusion **57**, 066014 (2017).

12. R. Hua, H. Sio, S. C. Wilks, F. N. Beg, C. McGuffey, M. Bailly-Grandvaux, G. W. Collins, and Y. Ping, Appl. Phys. Lett. **111**, 034102 (2017).

13. C. K. Li, P. Tzeferacos, D. Lamb, G. Gregori, P. A. Norreys, M. J. Rosenberg, R. K. Follett, D. H. Froula, M. Koenig, F. H. Seguin, J. A. Frenje, H. G. Rinderknecht, H. Sio, A. B. Zylstra, R. D. Petrasso, P. A. Amendt, H. S. Park, B. A. Remington, D. D. Ryutov, S. C. Wilks, R. Betti, A. Frank, S. X. Hu, T. C. Sangster, P. Hartigan, R. P. Drake, C. C. Kuranz, S. V. Lebedev, and N. C. Woolsey, Nat. Commun. **7**, 13081 (2016).

14. H. Sio, J. A. Frenje, J. Katz, C. Stoeckl, D. Weiner, M. Bedzyk, V. Glebov, C. Sorce, M. Gatu Johnson, H. G. Rinderknecht, A. B. Zylstra, T. C. Sangster, S. P. Regan, T. Kwan, A. Le, A. N. Simakov, W. T. Taitano, L. Chacòn, B. Keenan, R. Shah, G. Sutcliffe, and R. D. Petrasso, Rev. Sci. Instrum. **87**, 11D701 (2016).

15. N. V. Kabadi, H. Sio, V. Glebov, M. Gatu Johnson, A. MacPhee, J. A. Frenje, C. K. Li, F. Seguin, R. Petrasso, C. Forrest, J. Knauer, and H. G. Rinderknecht, Rev. Sci. Instrum. **87**, 11D817 (2016).

16. G. D. Sutcliffe, L. M. Milanese, D. Orozco, B. Lahmann, M. Gatu Johnson, F. H. Séguin, H. Sio, J. A. Frenje, C. K. Li, R. D. Petrasso, H.-S. Park, J. R. Rygg, D. T. Casey, R. Bionta, D. P. Turnbull, C. M. Huntington, J. S. Ross, A. B. Zylstra, M. J. Rosenberg, and V. Yu. Glebov, Rev. Sci. Instrum. **87**, 11D812 (2016).

17. B. Lahmann *et al*., Rev. Sci. Instrum. **87**, 11D801 (2016).

18. H. Chen *et al*., Phys. Rev. Lett. **102**, 105001 (2009).

19. H. Chen, S. C. Wilks, D. D. Meyerhofer, J. Bonlie, C. D. Chen, S. N. Chen, C. Courtois, L. Elberson, G. Gregori, W. Kruer, O. Landoas, J. Mithen, J. Myatt, C. D. Murphy, P. Nilson, D. Price, M. Schneider, R. Shepherd, C. Stoeckl, M. Tabak, R. Tommasini, and P. Beiersdorfer, Phys. Rev. Lett. **105**, 015003 (2010).

20. H. Chen, G. Fiksel, D. Barnak, P.-Y. Chang, R. F. Heeter, A. Link, and D. D. Meyerhofer, Phys. Plasmas **21**, 040703 (2014).

21. O. V. Gotchev, J. P. Knauer, P. Y. Chang, N. W. Jang, M. J. Shoup III, D. D. Meyerhofer, and R. Betti, Rev. Sci. Instrum. **80**, 043504 (2009).

22. H. Chen *et al*., Phys. Rev. Lett. **114**, 215001 (2015).

23. H. Chen *et al*., Phys. Plasmas **22**, 056705 (2015).

24. H. Chen, D. D. Meyerhofer, S. C. Wilks, R. Cauble, F. Dollar, K. Falk, G. Gregori, A. Hazi, E. I. Moses, C. D. Murphy, J. Myatt, J. Park, J. Seely, R. Shepherd, A. Spitkovsky, C. Stoeckl, C. I. Szabo, R. Tommasini, C. Zulick, and P. Beirsdorfer, High Energy Density Phys. **7**, 225 (2011).

25. M. Millot, N. Dubrovinskaia, A. Černok, S. Blaha, L. Dubrovinsky, D. G. Braun, P. M. Celliers, G. W. Collins, J. H. Eggert, and R. Jeanloz, Science **347**, 418 (2015).

26. J. R. Rygg, J. H. Eggert, A. E. Lazicki, F. Coppari, J. A. Hawreliak, D. G. Hicks, R. F. Smith, C. M. Sorce, T. M. Uphaus, B. Yaakobi, and G. W. Collins, Rev. Sci. Instrum. **83**, 113904 (2012).

27. E. A. Mathez *et al*., Geochim. Cosmochim. Acta **59**, 781 (1995).

28. Z. Konôpková *et al*., Nature **534**, 99 (2016).

29. K. Ohta et al., Nature **534**, 95 (2016).

30. R. F. Smith, S. M. Pollaine, S. J. Moon, K. T. Lorenz, P. M. Celliers, J. H. Eggert, H.-S. Park, and G. W. Collins, Phys. Plasmas **14**, 057105 (2007).

31. S. Zhao *et al*., Proc. Nat. Acad. Sci. **114**, 9791 (2017).

32. S. Zhao *et al*., Acta Mater. **103**, 519 (2016).

33. J. A. Frenje, P. E. Grabowski, C. K. Li, F. H. Séguin, A. B. Zylstra, M. Gatu Johnson, R. D. Petrasso, V. Yu. Glebov, and T. C. Sangster, Phys. Rev. Lett. **115**, 205001 (2015).

34. D. E. Fratanduono, D. H. Munro, P. M. Celliers, and G. W. Collins, J. Appl. Phys. **116**, 033517 (2014).

35. H. G. Rinderknecht *et al*., Bull. Am. Phys. Soc. **61**, BAPS.2016.DPP.GO5.11 (2016).

36. Y. Ping, D. G. Hicks, B. Yaakobi, F. Coppari, J. Eggert, and G. W. Collins, Rev. Sci. Instrum. **84**, 123105 (2013).

37. J. S. Oakdale *et al*., Adv. Funct. Mater. **27**, 1702425 (2017).

38. R. F. Smith, C. A. Bolme, D. J. Erskine, P. M. Celliers, S. Ali, J. H. Eggert, S. L. Brygoo, B. D. Hammel, J. Wang, and G. W. Collins, J. Appl. Phys. **114**, 133504 (2013).

39. D. Layzer, Astrophys. J. **122**, 1 (1955).

40. P. Ramaprabhu *et al*., Phys. Fluids **24**, 074107 (2012).

41. R. E. Olson, D. K. Bradley, G. A. Rochau, G. W. Collins, R. J. Leeper, and L. J. Suter, Rev. Sci. Instrum. **77**, 10E523 (2006).

42. R. E. Olson *et al*., Phys. Plasma **18**, 032706 (2011).

43. H. M. Johns *et al*., Bull. Am. Phys. Soc. **61**, BAPS.2016.DPP.PO8.6 (2016).

44. A. B. Zylstra, H. W. Herrmann, Y. H. Kim, A. M. McEvoy, M. J. Schmitt, G. Hale, C. Forrest, Y. Yu. Glebov, and C. Stoeckl, Rev. Sci. Instrum. **88**, 053504 (2017).

45. A. B. Zylstra, J. A. Frenje, M. Gatu Johnson, G. M. Hale, C. R. Brune, A. Bacher, D. T. Casey, C. K. Li, D. McNabb, M. Paris, R. D. Petrasso, T. C. Sangster, D. B. Sayre, and F. H. Séguin, Phys. Rev. Lett. **119**, 222701 (2017).

46. S. C. Hsu *et al*., EPL **115**, 65001 (2016).

47. T. R. Joshi *et al*., Phys. Plasmas **24**, 056305 (2017).

48. B. Rollin and M. J. Andrews, J. Turbul. **14**, 77 (2013).

49. J. D. Schwarzkopf *et al*., Flow Turbulence Combust. **96**, 1 (2016).

50. D. Besnard *et al*., Los Alamos National Laboratory, Los Alamos, NM, Report LA-12303-MS (1992); K. Stalsberg-Zarling and R. Gore, Los Alamos National Laboratory, Los Alamos, NM, Report LA-UR-11-04773 (2011).

51. S. A. Slutz, M. C. Herrmann, R. A. Vesey, A. B. Sefkow, D. B. Sinars, D. C. Rovang, K. J. Peterson, and M. E. Cuneo, Phys. Plasmas **17**, 056303 (2010).

52. M. R. Gomez, S. A. Slutz, A. B. Sefkow, D. B. Sinars, K. D. Hahn, S. B. Hansen, E. C. Harding, P. F. Knapp, P. F. Schmit, C. A. Jennings, T. J. Awe, M. Geissel, D. C. Rovang, G. A. Chandler, G. W. Cooper, M. E. Cuneo, A. J. Harvey-Thompson, M. C. Herrmann, M. H. Hess, O. Johns, D. C. Lamppa, M. R. Martin, R. D. McBride, K. J. Peterson, J. L. Porter, G. K. Robertson, G. A. Rochau, C. L. Ruiz, M. E. Savage, I. C. Smith, W. A. Stygar, and R. A. Vesey, Phys. Rev. Lett. **113**, 155003 (2014).

53. R. F. Heeter *et al*., Rev. Sci. Instrum. **75**, 3762 (2004).

54. D. F. DuBois, B. Bezzerides, and H. A. Rose, Phys. Fluids B **4**, 241 (1992).

55. C. Stoeckl, R. E. Bahr, B. Yaakobi, W. Seka, S. P. Regan, R. S. Craxton, J. A. Delettrez, R. W. Short, J. Myatt, A. V. Maximov, and H. Baldis, Phys. Rev. Lett. **90**, 235002 (2003).

56. D. T. Michel, A. V. Maximov, R. W. Short, S. X. Hu, J. F. Myatt, W. Seka, A. A. Solodov, B. Yaakobi, and D. H. Froula, Phys. Rev. Lett. **109**, 155007 (2012).

57. R. K. Follett, D. H. Edgell, R. J. Henchen, S. X. Hu, J. Katz, D. T. Michel, J. F. Myatt, J. Shaw, and D. H. Froula, Phys. Rev. E **91**, 031104(R) (2015).

58. R. K. Kirkwood, B. B. Afeyan, W. L. Kruer, B. J. MacGowan, J. D. Moody, D. S. Montgomery, D. M. Pennington, T. L. Weiland, and S. C. Wilks, Phys. Rev. Lett. **76**, 2065 (1996).

59. P. Michel *et al*., Phys. Rev. Lett. **102**, 025004 (2009).

60. J. C. Fernández *et al*., Phys. Rev. Lett. **81**, 2252 (1998).

61. H. A. Baldis *et al*., Phys. Rev. Lett. **77**, 2957 (1996).

62. W. Seka, H. A. Baldis, J. Fuchs, S. P. Regan, D. D. Meyerhofer, C. Stoeckl, B. Yaakobi, R. S. Craxton, and R. W. Short, Phys. Rev. Lett. **89**, 175002 (2002).

63. D. Turnbull, P. Michel, J. E. Ralph, L. Divol, J. S. Ross, L. F. Berzak Hopkins, A. L. Kritcher, D. E. Hinkel, and J. D. Moody, Phys. Rev. Lett. **114**, 125001 (2015).

64. S. Depierreux, C. Neuville, C. Baccou, V. Tassin, M. Casanova, P.-E. Masson-Laborde, N. Borisenko, A. Orekhov, A. Colaitis, A. Debayle, G. Duchateau, A. Heron, S. Huller, P. Loiseau, P. Nicolaï, D. Pesme, C. Riconda, G. Tran, R. Bahr, J. Katz, C. Stoeckl, W. Seka, V. Tikhonchuk, and C. Labaune, Phys. Rev. Lett. **117**, 235002 (2016).

65. C. Neuville, V. Tassin, D. Pesme, M. C. Monteil, P. E. Masson-Laborde, C. Baccou, P. Fremerye, F. Philippe, P. Seytor, D. Teychenné, W. Seka, J. Katz, R. Bahr, and S. Depierreux, Phys. Rev. Lett. **116**, 235002 (2016).

66. D. E. Hinkel *et al*., Phys. Plasmas **18**, 056312 (2011).

67. P. E. Masson-Laborde, M. C. Monteil, V. Tassin, F. Philippe, P. Gauthier, A. Casner, S. Depierreux, C. Neuville, B. Villette, S. Laffite, P. Seytor, P. Fremerye, W. Seka, D. Teychenné, A. Debayle, D. Marion, P. Loiseau, and M. Casanova, Phys. Plasmas **23**, 022703 (2016).